EIC Detector R&D Progress Report

Project ID: eRD14
Project Name: PID Consortium for an integrated program for Particle Identification (PID) at a future Electron-Ion Collider
Period Reported: from 10/1/2015 to 12/31/2015

Project Members:
M.Alfred[8], L.Allison[13], M.Awadi[8], B.Azmoun[3], F.Barbosa[11], W.Brooks[17], T.Cao[16], M.Chiu[3], I.Choi[14], M.Contalbrigo[9], C.Han[14], A.Datta[15], M.Demarteau[2], J.M.Durham[12], A.Del Dotto[10,11], R.Dzhygadlo[7], D.Fields[15], M.Grosse-Perdekamp[14], J.Harris[18], X.He[6], H. van Hecke[12], T.Horn[4], J.Huang[3], C.Hyde[13], Y.Ilieva[16], G.Kalicy[13], E.Kistenev[3], Y.Kulinich[14], J.Lindesay[8], M.Liu[12], R.Majka[18], J.McKisson[11], R.Mendez[17], P.Nadel-Turonski[11], K.Park[13], K.Peters[7], R.Pisani[3], Yi Qiang[11], M.Sarsour[6], S.Rescia[3], P.Rossi[11], C.Schwarz[7], J.Schwiening[7] , C.L. da Silva[12], N.Smirnov[18], J.Stevens[11], A.Sukhanov[3], S.Syed[6], J.Toh[14], R.Towell[1], T.Tsang[3], R.Wagner[2], Ji.Wang[2], C.P.Wong[6], C.Woody[3], W.Xi[11], J.Xie[2], Z.W.Zhao[5], B.Zihlmann[11], and C.Zorn[11].

1) Abilene Christian University
2) Argonne National Lab
3) Brookhaven National Lab
4) Catholic University of America
5) Duke University
6) Georgia State University
7) GSI Helmholtzzentrum für Schwerionenforschung, Darmstadt, Germany
8) Howard University
9) INFN, Ferrara, Italy
10) INFN, Rome - Gruppo Collegato Sanità, Italy
11) Jefferson Lab
12) Los Alamos National Lab
13) Old Dominion University
14) University of Illinois at Urbana-Champaign
15) The University of New Mexico
16) University of South Carolina
17) Universidad Tecnica Federico Santa Maria, Valparaiso, Chile
18) Yale University

Abstract

The PID consortium (eRD14) was formed to develop integrated particle identification solutions for detectors at a future Electron-Ion Collider (EIC), combining different technologies to optimize cost and performance. The work approved for FY16 focuses on hadron identification, and includes R&D for high-resolution, mRPC-based time-of-flight detectors, and three types of imaging Cherenkov detectors: a DIRC for the central barrel, a dual-radiator RICH for the hadron endcap (complementary in concept to the single-radiator RICH developed as part of eRD6), and a modular aerogel RICH which could be used in several applications, but seems particularly suitable for the electron endcap. A significant effort is also put into photosensors for these detectors (primarily MCP-PMT-based ones, including LAPPDs), and in particular their performance in high magnetic fields, but for LAPPDs also on characterizing early production samples - and improving their capabilities (*e.g.*, UV photocathodes). The FY16 work builds on R&D performed earlier within three separate projects: eRD4 (DIRC and high-B), eRD10 (TOF), and eRD11 (RICH), which formed a starting point for the consortium. However, with regular bi-weekly meetings where progress is reported and discussed, and a well-attended consortium meeting in conjunction with the recent DNP meeting in Santa Fe, the collaboration between the various groups has been rapidly increasing - and a foundation has been laid for integrating the ongoing R&D efforts into a coherent PID system (or perhaps two complementary systems, since the EIC could end up having more than one detector). Discussions have also started on what future R&D would be needed to achieve these goals, and which issues will require collaboration with other consortia (for instance calorimetry for electron identification). The progress on TOF, RICH, DIRC, and sensor-related R&D is presented in the respective sections below.

Contents

1. *Time-of-Flight* *page 3*
2. *RICH* *page 17*
3. *DIRC* *page 37*
4. *Sensors in high magnetic fields* *page 54*

1. Time-of-Flight

Contact: M. Chiu <chiu@bnl.gov>

Abstract

For the TOF R&D these past 6 months, we have been working to understand better the performance characteristics of the 30-gap glass mRPC, including first attempts to measure its rate capability as well as studying its behavior under different gas mixtures. To help support this we have begun Garfield++ simulation studies. We have also explored further the possibility of using 3D printed plastic to form the gas gaps. Also, initial wideband preamp boards have been designed and built which will allow us to increase the number of channels we can read out. Our goal is to work towards construction of a meter square prototype that can achieve resolutions close to 10 ps in a reproducible manner within the next few years. This large scale prototype can hopefully be included in the sPHENIX and/or SOLID experiments to gain real world experience before the EIC.

Past

1.1 What was planned for this period?

1.1.1 Further studies of two prototype mRPCs, glass mRPCs and 3D printed gas gap mRPCs, including a rate capability test in the beam for the COMPASS experiment at CERN

1.1.2 Gas simulation for the mRPCs using GARFIELD++

1.1.3 Design of a preamplifier board for the mRPC readout

1.2 What was achieved?

1.2.1 Beam Test in the COMPASS at CERN

With our glass mRPCs, ~18ps time resolution had been achieved using a cosmic ray test stand at the nuclear physics laboratory at UIUC. To test mRPCs under higher particle flux rates than is possible from cosmic rays, we sent two types of the mRPC prototypes to the COMPASS experimental area for a rate capability test. Figure 1.2.1.1 shows the COMPASS spectrometers and the location of the test setup. In COMPASS, a 190 GeV negative pion beam is incident at a rate of $4*10^8$/s on a NH3 polarized target. Most of the non-interacting pions are stopped by a beam plug that is two meters long and is downstream of the target. Particles passing through this absorber are almost all muons. The mRPCs were placed at the end of the COMPASS spectrometers, about 55m downstream from the targets. By varying the location of the test setup away from the beam flux, the particle rate could be controlled. Three different locations were selected for the rate capability test. The flux rates were

estimated by using a 5cm x 20cm paddle scintillator in the front of the mRPCs. The red colored circles on the top right picture in the figure 1.2.1.1 show the selected three different locations. The flux rates at the top left, top right, and bottom are >80Hz/cm^2, 80Hz/cm^2, and 5Hz/cm^2, respectively. The bottom left picture in the figure shows the scintillators and the chambers for the mRPCs. The trigger for the data was generated by a double coincidence from the two paddle scintillators.

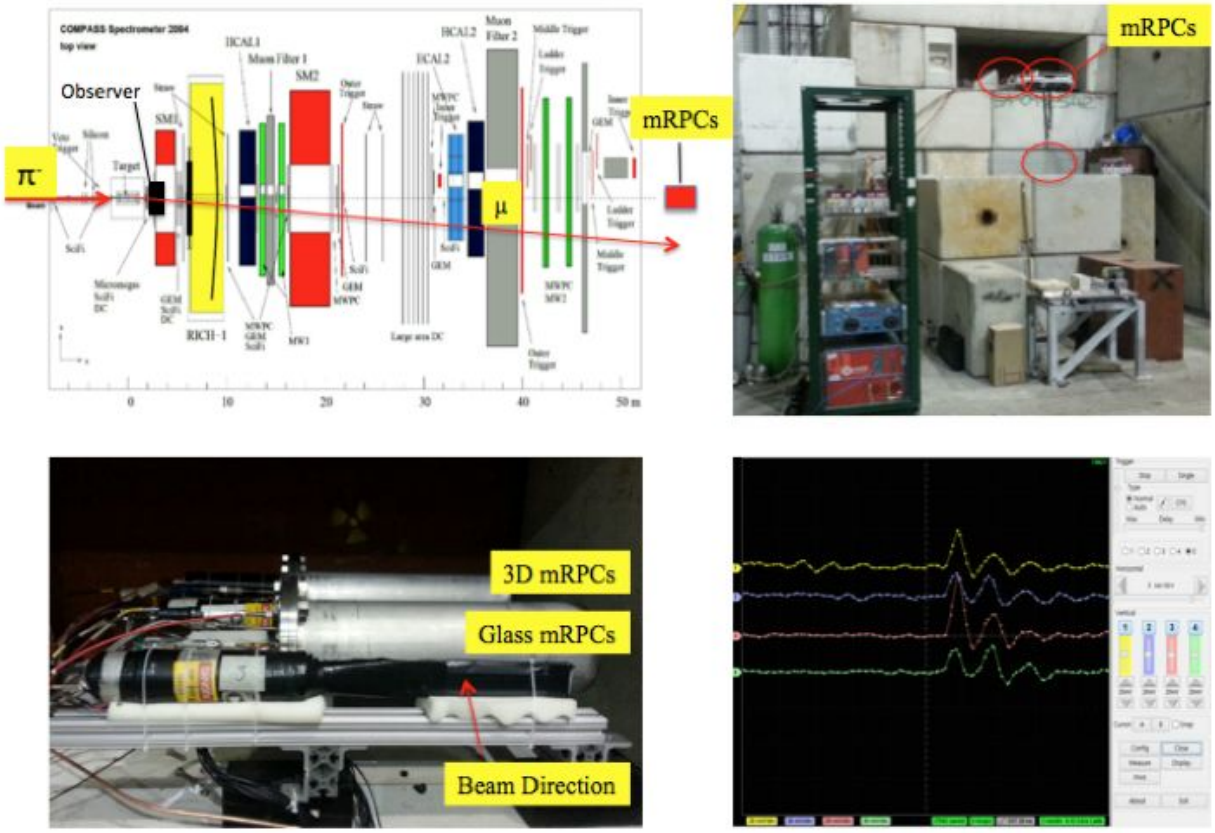

Figure 1.2.1.1: Top left diagram shows the COMPASS spectrometers and the location of the mRPCs is indicated with a red colored rectangle. The top right picture shows the test setup at the end of the COMPASS spectrometers. Bottom left shows two chambers for the glass mRPCs, 3D printed gas gap mRPCs, and scintillators for the trigger. Bottom right screen shot shows the signals from the glass mRPCs captured by the DRS4 waveform analyzer with a coincidence trigger.

Positive and negative polarity of the CAEN high voltage modules were used for applying an electric field in the mRPCs and their maximum combined high voltage could go up to 30kV (+15kV, -15kV). For this test, a range between 12kV to 24kV was selected.

Freon R134a and SF_6 are mixed in the gas mixing system and flowed into the two chambers at a rate of 150cc/min. The fraction of the SF_6 gas was varied from 1% to 3% relative to the Freon gas mixture. The pressure of the mixed gas in the chambers was measured at the gas gauge in the return gas line.

To vary the flux rate, the mRPC test setup is moved along the vertical direction to the beam line. Three different locations were chosen for the test shown in the top right side picture in the figure 1.2.1.1. The rates at the top two locations, where their positions are close to the beam line, were around 80Hz/cm^2 and the flux rate on the bottom where the position is far from the beam line was 5Hz/cm^2. However a significantly bigger amplitude of the mRPCs signal was observed at the flux rate of 80Hz/cm^2 than 5Hz/cm^2. In figure 1.2.1.2, the top left and top right pictures show the test setup in the two locations, while the bottom left and right plots show their accumulated signals.

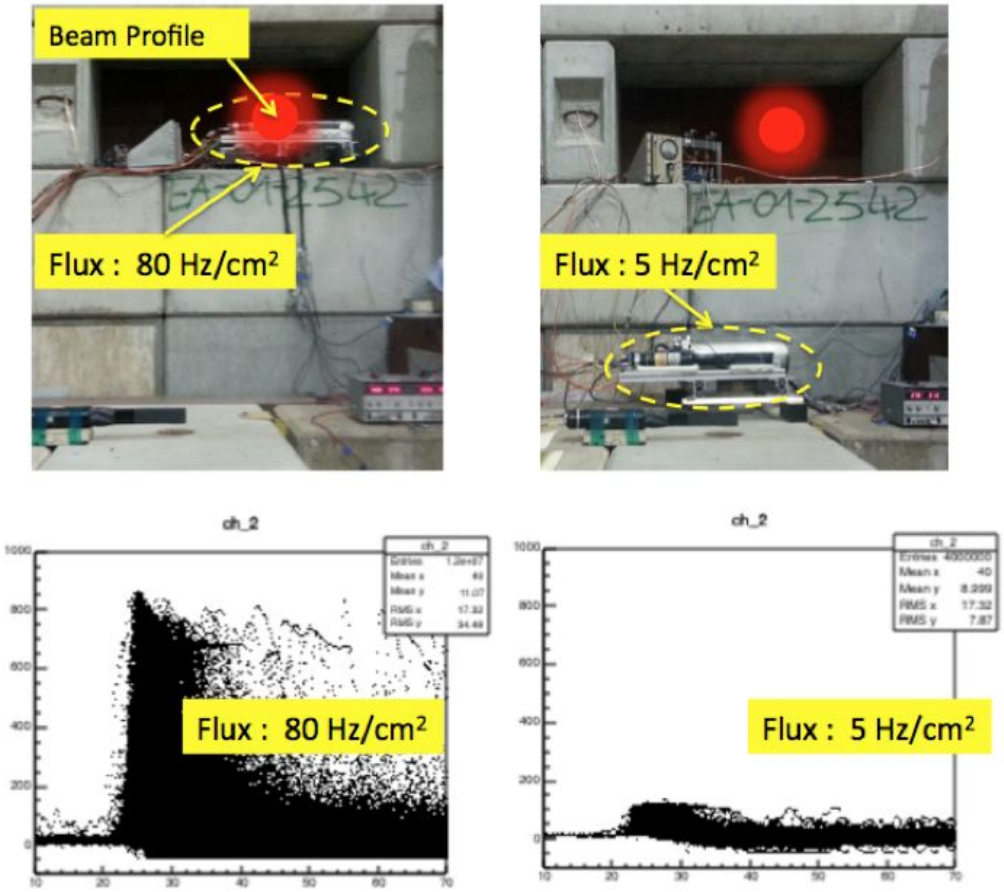

Figure 1.2.1.2. Top two pictures show the two locations for the test setup to vary the flux rate. The solid circles of red color in the pictures are estimated position of beam. The bottom two plots show the accumulated signals from mRPCs under the same gas mixture, 2% SF_6, and high voltage, 22kV, except the location. The range of Y-axis on the plots is from -10mV to 1000mV, and the X-axis is time from 10 ns to 70 ns.

We suspect that the significantly low amplitude of the signals observed when in the bottom location could be explained by a richer mixture of SF_6. The heavy SF_6 gas in the chamber couldn't flow easily out of the exhaust pipe, which is located 3 meters above the chamber. Also, the location of the exhaust outlet could have caused higher pressure towards the bottom than the top. A gas simulation might be able to confirm our hypotheses by varying the fraction of SF_6 and its pressure, and we also plan to redo these studies with cosmics in the lab, while varying the exhaust location.

We calculated the efficiency by comparing two hit counts from the two glass mRPCs that were placed together in the same gas cylinder.

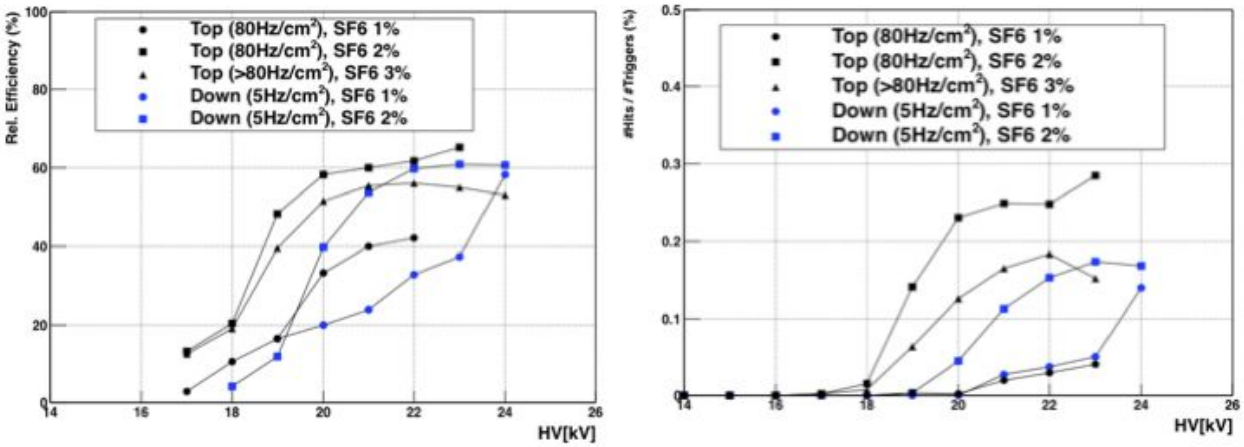

Figure 1.2.1.3. The left plot shows efficiency vs. high voltage results for different locations and gas mixtures. The right plot shows the hit ratios over the number of triggers.

Overall, the observed efficiency values reached up to 60% at a high voltage of 24kV using this hit-coincidence method. The results show that the efficiency at the low flux rate is even lower than at the high fluxes. This is consistent with the low signal amplitudes seen in the 5 Hz/cm^2 data. The COMPASS tracking could not be incorporated with the test system DAQ, so it isn't possible to have tracking for analysis. Without tracking, the absolute efficiency may not be correct, since one cannot guarantee having a track through both prototypes.

The time resolution results can be calculated from the distribution of the time difference between two mRPCs. The top left cartoon in figure 1.2.1.4 shows the channel mapping of the two mRPCs in the same gas chamber. Channel 1 and 3 are connected to both ends of the front mRPC and channels 2 and 4 are connected to the ends of the second mRPC. The time resolution can be calculated by subtracting the time value of channel 1 from the time value of channel 2 (same for channel 3 and 4). The top right plot in the figure shows the time correlation between channel 1 and 2. The bottom left plot shows the correlation between the time difference distribution and the signal rising speed of channel 1. The bottom right plot shows the correlation between the time difference distribution and the position difference estimated from the signal propagations. The red line in the bottom two plots is a fit to the correlations. Using the functions from the fits, the time difference distribution can be corrected. Figure 1.2.1.5 shows the two time difference distributions

before (left plot) and after (right plot) the two corrections, for 80Hz/cm^2, 2% SF_6, and a high voltage of 19kV. After applying the two corrections to line up the time difference distribution, 25.4 ps of time resolution has been obtained at flux rate of 80Hz/cm^2 with 2% SF_6. Figure 1.2.1.6 shows the time resolution results for different flux rates and gas mixtures. Note that the black solid triangle data are not corrected by the above correction methods due to the one missing channel in the data set.

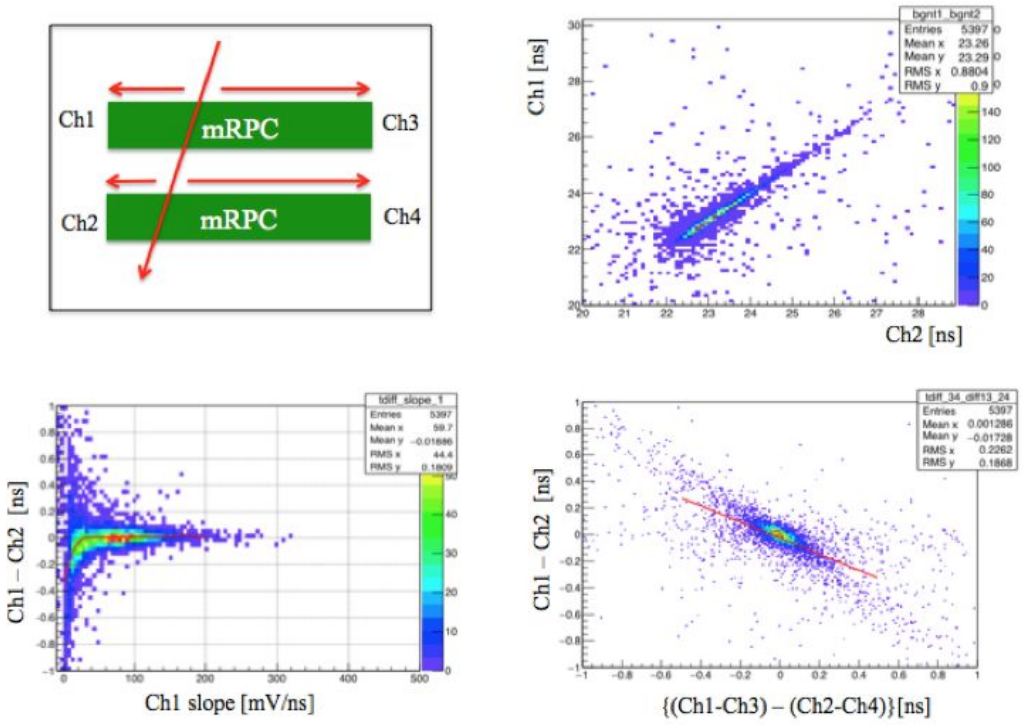

Figure 1.2.1.4. The top left diagram shows the channel mapping for the readout from the two mRPCs. The top right shows the time correlation between the channel 1 and 2. The bottom left plot shows the correlation between the time difference and the rise-time of channel 1. The bottom right plot shows the correlation between the time difference and hit position difference calculated from the signal propagation of all channels.

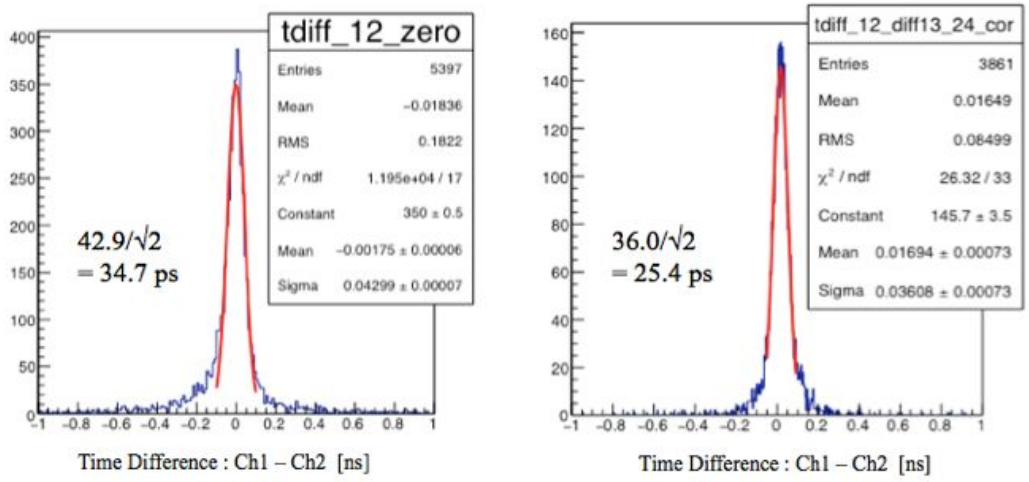

Fig 1.2.1.5. The left plot shows the time difference distribution with a Gaussian fitting before the corrections. The right plot shows the time difference distribution with a Gaussian fitting after the corrections.

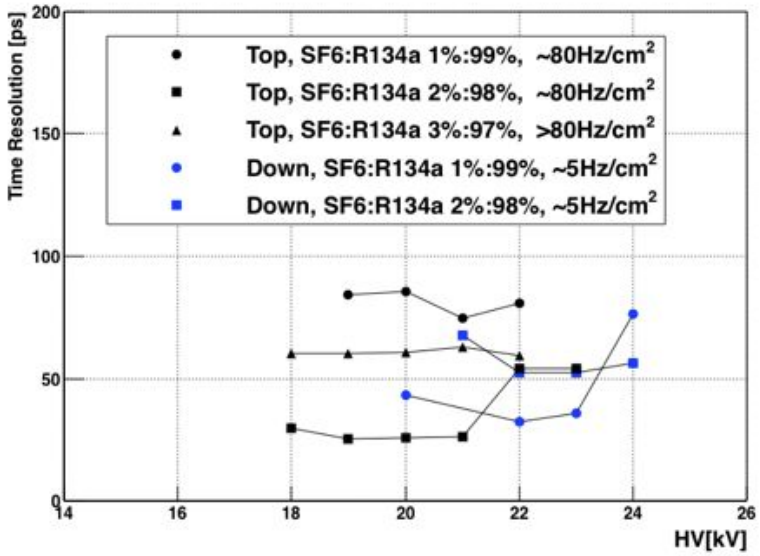

Figure 1.2.1.6. Time resolution results from the different flux rates and gas mixtures as a function of the applied high voltage.

Due to the previously mentioned problems with the gas system, some of the results are hard to interpret, since we should expect the lower flux data to have at least the same, and probably better timing resolutions. We intend to redo these studies, first in the lab at UIUC, and then in the Fermilab test beam in April. However, we were able to achieve 25 ps resolution at 80 Hz/cm^2, which means our initial measurement in the lab of 18ps is likely reproducible. Also, we believe this shows promise that the mRPCs might be able to work with reasonably good performance up to at least 80 Hz/cm^2, though we will want to confirm this under more controlled conditions. In studies using PYTHIA6 and based on the

experience at HERA, we expect a very low flux rate of particles from e+p or e+A events into a TOF wall at the EIC. The problem is instead that there could be an enormously higher rate of background events from beam gas and synchrotron backgrounds; at HERA these events swamped the usable DIS events. The mRPC should handle the flux from collision events very easily, but the background needs to further study in order to quantify exactly the flux rate that the detector is required to handle.

1.2.2 3D printed gas gap mRPCs

A second 3D printed mRPC prototype was built using a similar method as done in the last fiscal cycle. A 3D-printed resistive plate stack was attached to a printed circuit board using Kapton tape. The printed circuit board has four readout strips and a copper electrode. After proper insulation and wiring were done, the prototype was covered with another printed circuit board and tightened using bolts and nuts. The readout strips were then connected accordingly using wires. Our prototype has two stacks of 3D-printed resistive plate stack. Each of the 3D printed stack has 5 layers of 0.3-mm gas gap. Figure 1.2.2.1 shows the inner structure of the prototype and the completed prototype.

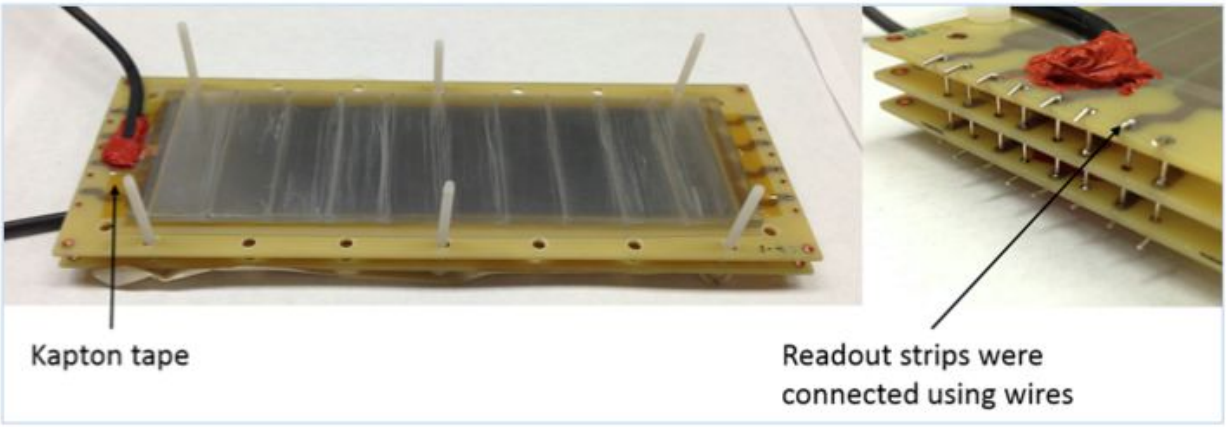

Figure 1.2.2.1. A photograph showing the inner structure of the 3D printed gas gap.

The two identical mRPC prototypes were mounted on a support structure to be placed in the gas chamber. The left picture in the figure 1.2.2.2 shows the 3D printed gas gap mRPCs. Signals from the 3D printed gas gap mRPCs were captured on the screen of the DRS4 waveform digitizer, but there was not enough time to setup for the data taking properly before the COMPASS beam ended. The 3D printed prototype is back at UIUC, where it will be studied using cosmics, and eventually tested in April at the Fermilab test beam facility.

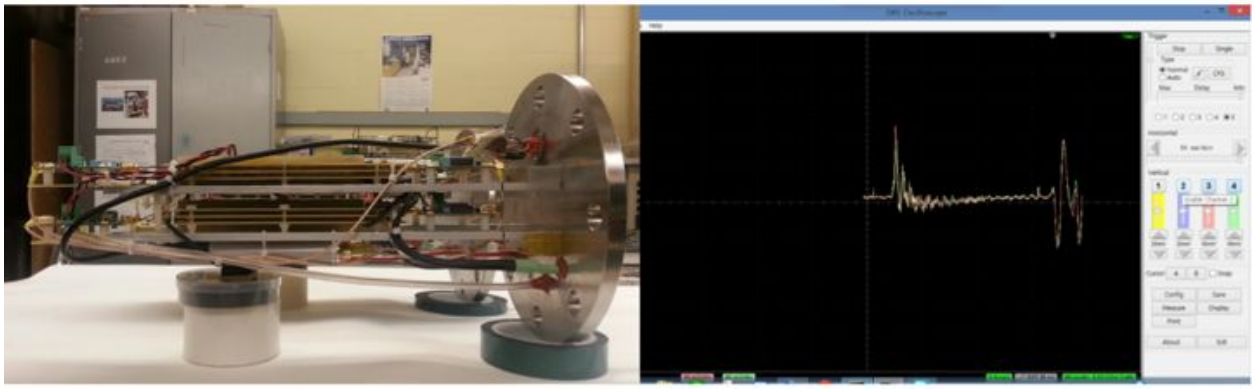

Figure 1.2.2.2. The left picture shows the two 3D printed gas gap mRPCs stacked on the rail of the gas fringe. The right screen shot shows signals (first peak from left to right) captured at the waveform analyzer.

1.2.3 Gas Simulation

To better understand how to improve our mRPC work, we have started to create a simulation of the mRPC detector physics using Garfield++. The work is still in the beginning stages, and we have been able to extract properties of different gas mixtures. Within the next several months we hope to having running the full simulation all the way up to the simulated signals through our electronics. We have compiled and run the current code on a Mac mini running OSX Yosemite, and the code has also been tested on Linux systems. The installed version of Garfield++ is from early October 2015.

We have created gas files for several mixtures of R134A, isobutane, and SF6, which are the standard gases in use today. Since the mixture used for the UIUC prototypes in the Compass test beam were R134A/SF6 mixtures with 1, 2, and 3% SF6, we have concentrated on understanding the properties of what happens when varying the proportion of SF6. We looked at the number of primary electrons generated, the drift velocity of the gas, and the Townsend and attachment coefficients. Plots of the primary electron distribution and Townsend and attachment coefficents are shown in figure 1.2.3.1.

After accounting for the dielectric effect of the glass in our mRPCs, the electric fields in the gas gaps were calculated to be about 152,000 V/cm when 20 kV are applied across one stack (one stack contains 9 gas gaps). From Garfield, we saw very little difference between the drift velocities when varying the SF6 percentage. There was a 15% increase in the number of primary electrons when going from 1% to 2% SF6, which then leveled off for increasing percentages. A small decrease was seen in the effective coefficient (Townsend minus attachment) for increasing SF6 percentage. While our conclusions right now are incomplete, we believe that we are building the tools necessary to start making optimization decisions on the mRPC design based on first principles.

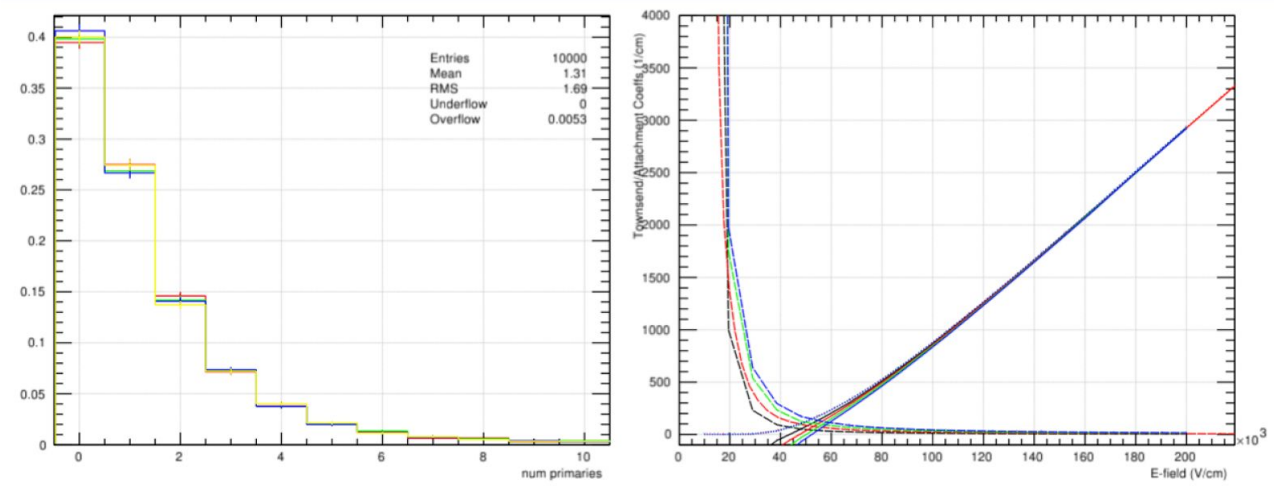

Figure 1.2.3.1. The left picture shows the number of primary electrons per 105 um gas gap, for SF_6 percentages of 1, 2, 3, and 4% and an E-field of 152K V/cm. The right figure shows the Townsend and Attachment coefficients as a function of E-field (solid and dashed lines, respectively).

1.2.4 Preamplifier Development

To amplify the fast signals from the mRPC, we have been using various fast TI amplifier evaluation boards, such as the LMH6881eval, which have gain bandwidth products (GBP) in the 5+ GHz range. While these boards are good for testing a few channels, they are relatively large and thus cannot be packed at the detector, so our testing has currently been limited to a few channels at a time. Andrey Sukhanov has developed a compact, 4 channel preamp board called the UFAMP, which will allow testing as many channels as we have digitizers for. It is based on the TI LMH5401, which has a GBP of 8 GHz. It is designed to have a gain of 16 with a -3dB bandwidth of 900 MHz. The schematic is shown in Fig. 1.2.4.1.

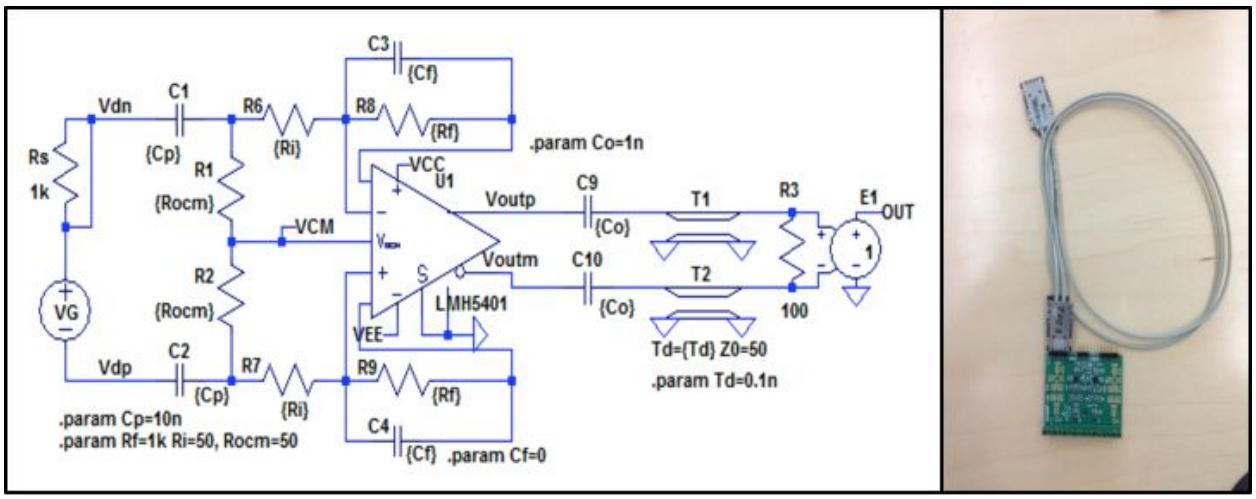

Figure 1.2.4.1. Schematic for UFAMP v4 and separate TLT board (left). Preamp board with hard metric differential cable attached (right).

We have also developed a balun board using a transmission line transformer (TLT), so that we can convert the differential signal from the detector to the single-ended input of the DRS4 eval board without any signal loss. The UFAMP amplifier was tested using a ADCMP850 evaluation board which should generate a pulse with a risetime of 70 ps, though our measurements yielded 390 ps. Using this fast risetime pulse signal, we could test the performance of the preamp. Our initial testing showed this first prototype of our preamp has an analog bandwidth of ~300 MHz, much lower than our estimate of 900 MHz, as shown in fig. 1.2.4.2. This problem has been identified as due to a stray capacitance left from some unused traces on the feedback line of the amplifier, based on including a 1 pF capacitance at the trace location in the SPICE model. We will produce an updated version of the UFAMP with this fix after some real world testing on mRPC signals with the current revision of the board. Additionally, we have recently borrowed a GHz sine wave generator and will map out the response in detail.

Figure 1.2.4.2. The pulse generated by the ADCMP850 board (left). Resulting signal through the preamp (right). Both were read out by an Agilent GHz scope.

The preamplifier development is just the start of several more steps that need to be taken toward having suitable electronics for 10 ps TOF at the EIC. We are preparing to study how to propagate the clock over distances of many meters while maintaining low jitter. We also have been in discussion with Stefan Ritt about the the possibility of developing a DRS5 ASIC, which would have a deep enough buffer to handle the roughly 4 μs trigger latency which are typical at colliders. We will also investigate other options, such as the PSEC5 and the CERN PSTDC.

1.3 What is planned was not achieved, why not, and what will be done to correct?

1.3.1. Further development and study of mRPCs

We have achieved 25.4 ps time resolution at 80Hz/cm^2 flux rate at the COMPASS, but the time resolution results at 5Hz/cm^2 have an issue of low signal amplitude due to the high pressure and a rich SF6 fraction in the chamber. A gas simulation study could help to understand the issue. We will investigate these gas issues at UIUC, and have tentatively scheduled another beam test for Fermilab in April, parasitically with the sPHENIX calorimeter tests. Another beam test could also be scheduled at COMPASS in the fall, if needed.

In this future test it would be useful to scan the SF6 percentage between 1% and 3% to find if there is a maximum in the timing performance at ~2%, as hinted by our data from the COMPASS test beam run.

We couldn't have enough time to take useful data from the 3D mRPC. So it also needs a beam test for the time resolution and detector efficiency measurements. We also have not gone further with using mylar or kapton as dielectric materials. We have a design completed, and will build and test this "flexible" dielectric mPRC over the next 6 months.

1.3.2. mRPC simulations using Garfield

We have made progress on the mRPC simulation, with working code that can extract all the gas properties. We have also successfully incorporated Howard into this effort; most of the gas files were generated at Howard, and they are now able to run through the many different configurations that will be needed. Over the next 6 months we hope to have a complete end-to-end simulation, from the incoming particle all the way to the signal generated on the pickup cathodes.

1.3.3. LAPPD MCP-PMT TOF

We have not been able to test any LAPPD style MCP-PMT as a TOF detector. Most of that was schedule for the coming year, so we expect to have some initial studies done over the next 6 months.

1.3.4. Electronics development

We have made some progress on the electronics by developing a first prototype of a fast preamp board. There is a minor issue which limits the bandwidth on this version, but we expect our next version will have this issue fixed. We continue to think about how to develop the electronics for a system with a larger number of channels and which can work at a collider.

1.3.5 Start Timing

A common complaint about a TOF at the EIC is that there may not be a good start counter. We believe one easy solution would be to have TOF everywhere. Then the electron timing could be used to determine the time start. Another possibility is that one can use just the times of the tracks into a TOF wall – with enough particles, one can do a statistical determination of the start time. Alexander Kiselev and others have studied this for the PANDA experiment and found that even for a low number of tracks, as little as 2 or 3, one can satisfactorily determine the start time. We intend to do a full study of this for a realistic EIC detector configuration over the next 6 months.

Future

1.4 What is planned for 2016 and beyond? How, if at all, is this planning different from the original plan?

Over the next year we hope to improve on our understanding of the mRPC performance, and improve the timing resolution towards our goal of 10 ps. We also hope to start scaling up the tests so that we can read out many more channels, and be able to build up to a system that is about the size of a meter square, at which point we believe we will have demonstrated that it would be possible to build a TOF wall of many square meters. Ultimately we hope that the R&D supported here will contribute to having a prototype of about a meter square that we can test at sPHENIX or SOLID in the early 2020's, on the way towards the full TOF walls in an EIC detector.

1.5 What are critical issues?

Currently there are many critical issues. We still have to demonstrate we can get down to 10 ps with a particular configuration of the mRPC. The electronics that can achieve very high resolution (much less than 10 ps), draw low power, and work at a collider does not quite exist yet. Fortunately, there is much interest from the high energy community as well as from industry for such electronics, and so there is on-going effort from different sources to also solve this problem. For example, we supported a couple of phase-I SBIR applications which might end up producing the solution that we need.

Manpower

University Faculty: Matthias Grosse-Perdekamp (UIUC), Marcus Alfred (Howard), Rusty Towell (ACU). Matthias and Marcus spend roughly 20% of their time on this project, and Rusty spent two summer months.

Scientists: Mickey Chiu (BNL), Andrey Sukhanov (BNL). Mickey and Andrey spend about 25% of their time on this project. We hope to increase that to 50% over the coming year.

Post-docs: Ihnjea Choi (UIUC). Ihnjea is covered for 0.5 FTE by EIC R&D funds, and spent all his time over the past 6 months on this project. He is supervised by Matthias Grosse-Perdekamp.

Students: Hannah Hamilton (ACU), Cecily Towell (ACU), Majed Awadi (Howard), Jun Hui See Toh (UIUC), Seung Joon Oh (UIUC). Hannah and Cecily worked during the summer, and the other students are using their extracurricular time during the semester for their studies.

External Funding

Support for much of the UIUC activities, such as travel and materials, is provided by Matthias' NSF grant and UIUC funds. Materials for the preamps developed by Andrey has been supported by Mickey's PECASE funds. We are currently also applying to various Homeland Security programs for additional funding.

Publications

We are preparing a NIM article on our recent 18 ps resolution result, but we are currently holding up submission while our applications for IP rights are being processed by the UIUC and BNL tech transfer offices.

2. RICH

Contact: H. van Hecke <hubert@lanl.gov>

Abstract

Work continues on simulations of a modular imaging Cherenkov detector, as well as on simulations of a dual-radiator (aerogel-gas) RICH, with an outward-reflecting mirror, in the environment of an EIC detector.
A prototype of the modular aerogel imaging Cherenkov counter is being constructed at GSU, to be tested in a beam in the Spring.

Past

2.1 What was planned?

- Continued study of the modular imaging detector design and the dual radiator designs.
- Incorporation of these into an EIC MC detector framework.
- Study of existing Cherenkov systems.
- Design and construction of a prototype modular detector.

2.2 What was achieved?

2.2.1 Modular Aerogel RICH

2.2.1.1 Prototype

A prototype of the modular aerogel RICH is under construction at Georgia State University (GSU) and the plan is to have a beam test in April of 2016 at Fermilab. Components are purchased with local funds available to the group at GSU. The aerogel blocks are to be provided by the JLab and Los Alamos groups. For the data acquisition, a system designed by Martin Purschke of BNL will be used.

The modular RICH hardware design consists of a sealed acrylic box with removable components. The box consists of solvent-welded butt joint seams and a top panel that is affixed with screws and sealed with an internal O-ring. This provides a water, air, and light tight environment necessary for the aerogel and the photomultiplier tube (PMT). The rear of the box is outfitted with two DB-37 and one SHV connector to provide power and signal readout for the PMT. The connectors are IP67-rated keeping the box sealed.

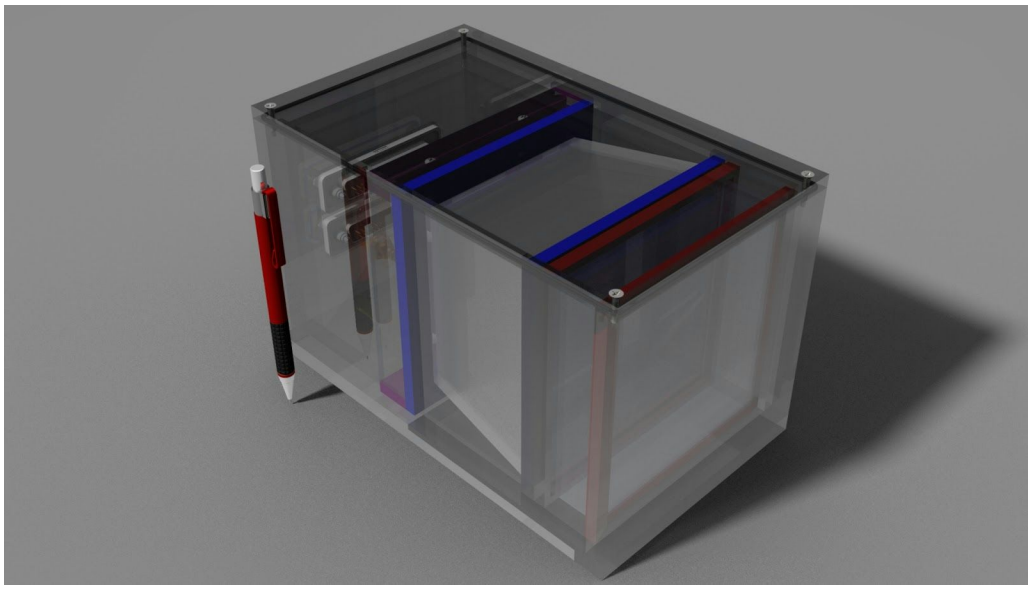

Figure 2.2.1.1. Prototype detector design seen from the aerogel side.

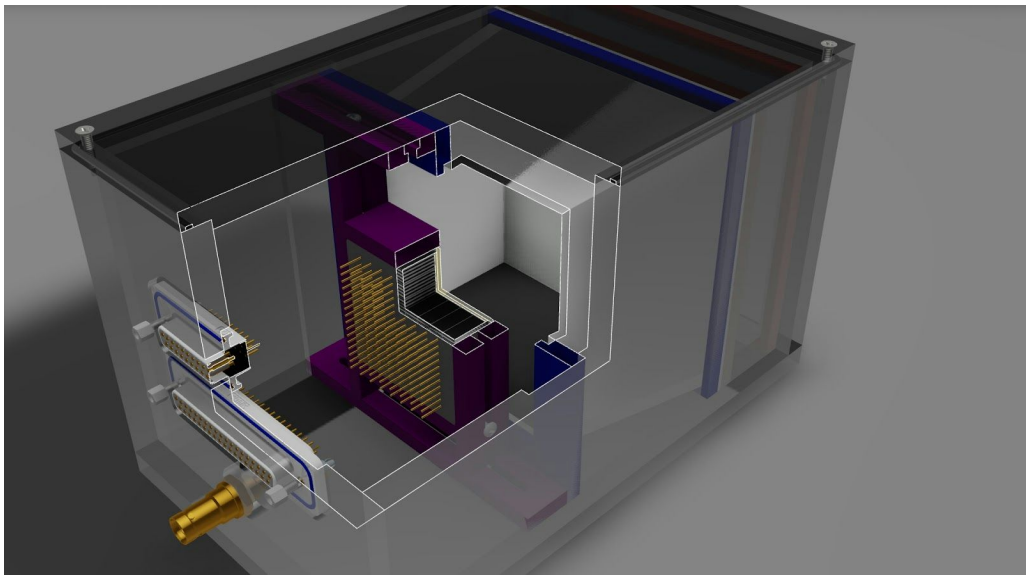

Figure 2.2.1.2. Prototype detector seen from the back. The cutout shows the multi-anode PMT.

Internally there are four separate components, all removable, split to ease assembly and maintenance. As the beam enters the box, it first strikes a 30-mm thick block of aerogel, held in place with two frame pieces. This is followed by a Fresnel lens and then the mirror assembly. The mirrors have bevel cuts and are attached to a frame as well to ease assembly and to provide firm points for spacing. The mirrors are currently back surfaced acrylic. The final component is a holder for a Hamamatsu 8x8 multi-anode PMT (H12700), where each anode covers 6x6mm. The mount has screws and slots so the PMT can be moved to any location in the focal plane.
Some components have been acquired, and the prototype will be constructed in the spring, and operated with cosmic rays before being tested at FNAL, taking advantage of the sPHENIX beam tests scheduled for April.

2.2.1.2 Simulation Updates - Modular design

The simulation results presented in the previous report were based on an aerogel block of 2-cm thickness with a refractive index of 1.025. A new set of simulations have been performed in order to match the properties of the aerogel block to be used in the upcoming beam test in April of 2016.

The thickness and the refractive index of the aerogel were changed to 3 cm and 1.05, respectively, to reflect the aerogel sample which has refractive index in range 1.047 to 1.0523. The updated design of the modular RICH detector is shown in Figure 2.2.1.3. Also shown on Figure 2.2.1.4, and 2.2.1.5 are the simulation results, which demonstrate that both, the Cherenkov ring radius and the number of Cherenkov photons emitted by incident particles increase with thickness and with refractive index of aerogel.

Figure 2.2.1.6 shows that in the current simulation setup with thickness and refracrive index of aerogel set to 3 cm and 1.05, respectively, the radii of Cherenkov photons emitted by incident pions and incident kaons overlap when momentum of incident particles is 5 GeV or higher. Moreover, the numbers of Cherenkov photons emitted by incident pions and incident kaons overlap when the momentum of incident particles is 3 GeV or higher. We conclude that pions and kaons which are in interesting momentum range (3-15 GeV) are hard to be identified from each other by simply considering the Cherenkov ring radius, or the number of Cherenkov photons detected. However, Likelihood Analysis algorithm will be studied for particle identification.

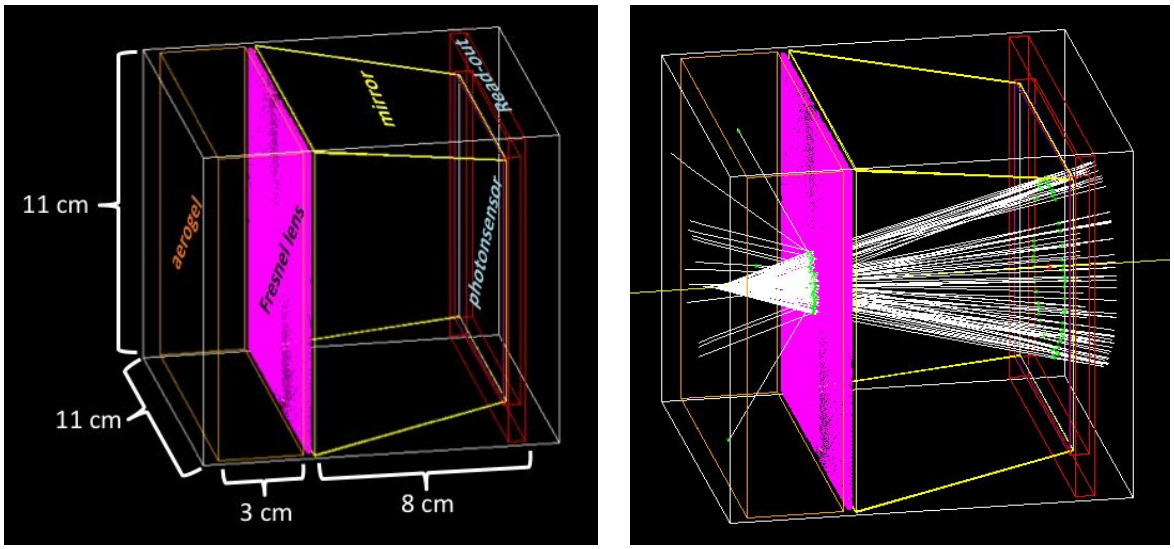

Figure 2.2.1.3. Figure on the left shows the modular RICH detector design in GEMC simulation framework. White wireframe is the detector holder box. Orange wireframe is a 3-cm thick aerogel with refractive index 1.05. In magenta is the Fresnel lens with 100 grooves, focusing the Cherenkov radiation. Four mirrors (yellow) are placed at the top, bottom, left, and right of the detector. At the back (in red) of the detector are photosensors and readout electronics. Figure on the right shows a single negatively-charged pion passing through the detector. The pion emits Cherenkov photons inside the aerogel. Those photons are focused by a Fresnel lens before arriving at the photosensors.

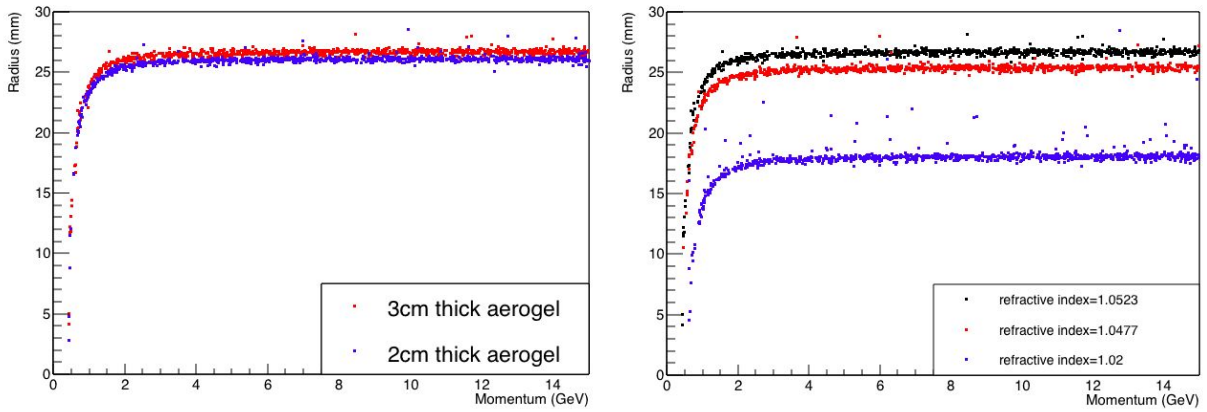

Figure 2.2.1.4. Plots of Cherenkov ring radius versus momentum (in range 0 to 15 GeV) for incident pions. Left: simulations with fixed refractive index n=1.0523 of aerogel, but with different aerogel thicknesses (3 cm in red, and 2 cm in blue). Right: simulation with fixed aerogel thickness (3 cm) but with different refractive index (1.0523 in black, 1.0477 in red, and 1.02 in blue).

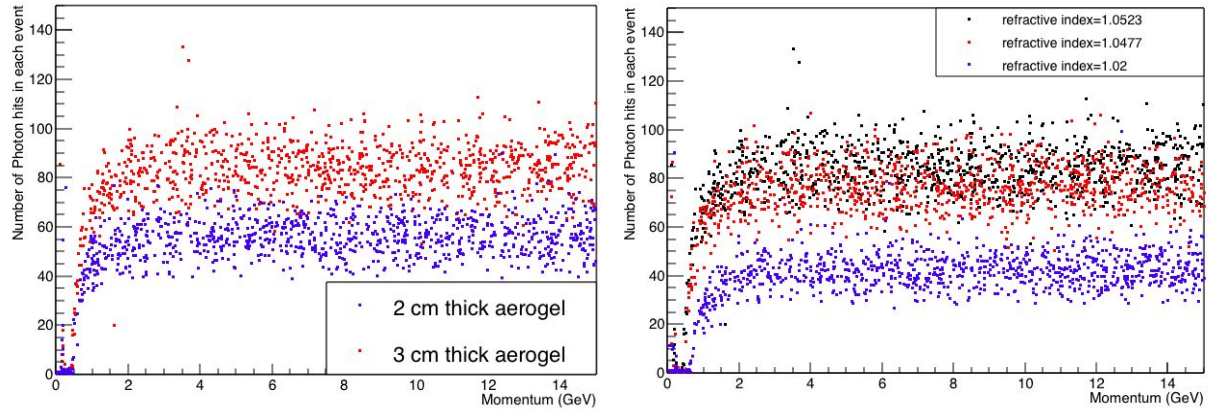

Figure 2.2.1.5. Number of Cherenkov Photon Hits detected by the Photon Sensor vs. momentum (in range 0 to 15 GeV) of incident pions. Left: fixed refractive index (1.0523), but with different thicknesses (3 cm in red, and 2 cm in blue) of the aerogel. Right: simulation with fixed aerogel thickness (3 cm) but with different refractive index (1.0523 in black, 1.0477 in red, and 1.02 in blue).

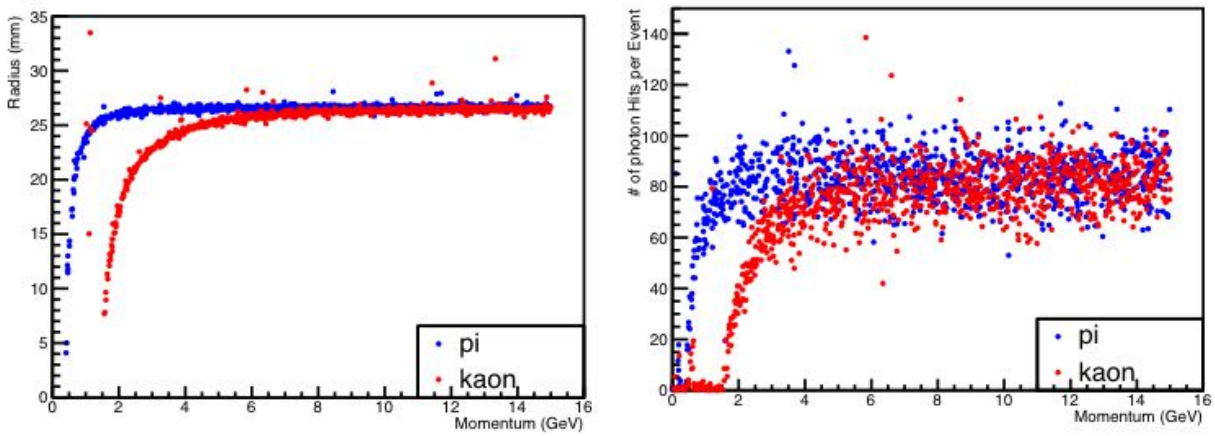

Figure 2.2.1.6. Comparisons of Radius vs. Momentum (right), and of Number of Photon Hits Detected on Photonsensor vs. Momentum (left) between incident pions (blue), and incident kaons (red).

2.2.1.3 Backgrounds

There are three main sources of background. These are Cherenkov photons emitted by incident particles inside the Fresnel lens, and Cherenkov photons emitted by delta ray electrons inside the aerogel and the Fresnel lens. The number of background Cherenkov photons from different sources, and the number of signal Cherenkov photons emitted by incident pions inside the aerogel are shown on the left of Figure 2.2.1.7. It shows that the number of background Cherenkov photons is lower than the number of signal Cherenkov photons in the interesting momentum range (3-15 GeV).

Figure 2.2.1.8 shows Radius versus Momentum of incident particles. Here, radius is defined as the mean of the distance between the center of the photosensor plane and each of the photon hits that are generated in the same event. The Radius of Signal Cherenkov Photons is between 25 mm and 27 mm in momentum range 3 to 15 GeV, while radius of background Cherenkov Photons is randomly distributed.

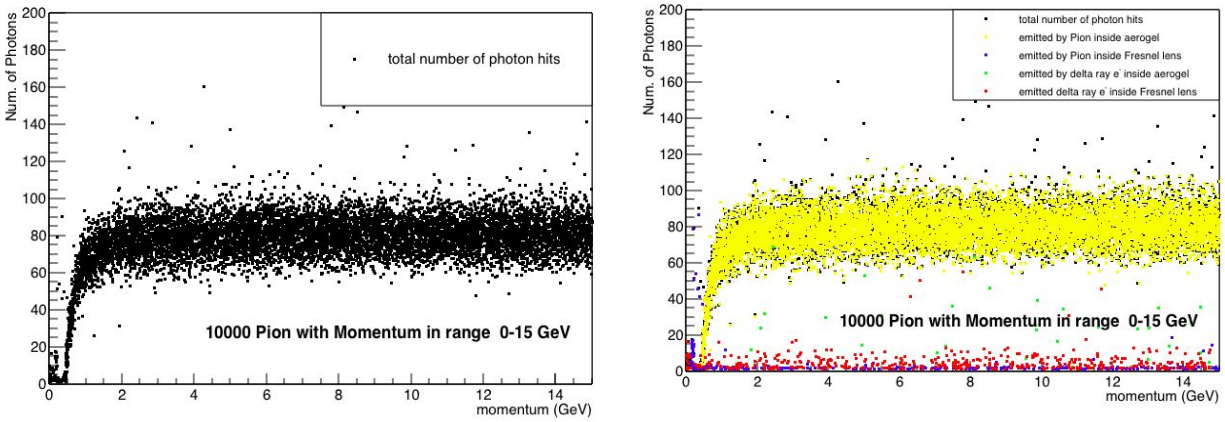

Figure 2.2.1.7. Number of Photons detected on Photosensor in Each Event vs. Momentum of Incident Pions. Black dots on both plots represent the sum of the numbers of signal, and background Cherenkov photons detected. Plot on the right shows the number of signal Cherenkov photons (Yellow), and background Cherenkov photons from different sources, counted in each event. Blue, green, and red dots represent background Cherenkov photons emitted by incident Pions inside Fresnel lens, by delta ray electrons inside aerogel, and by delta ray electrons inside Fresnel lens, respectively.

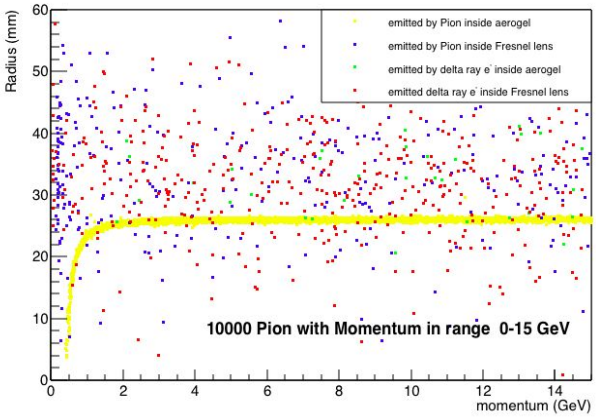

Figure 2.2.1.8. Radius vs Momentum. Yellow dots represent signal Cherenkov photons emitted by incident pions inside aerogel. Blue, green, and red dots represent background Cherenkov photons emitted by incident Pions inside Fresnel lens, by delta ray electrons inside aerogel, and by delta ray electrons inside Fresnel lens, respectively.

2.2.1.4 Effects of a Magnetic field

A uniform 1.5-T y-direction (transverse to the optical axis) magnetic field was implemented in the simulation. The magnetic field deflects the trajectory of charged particles including delta ray electrons. Delta ray electrons, which also emit Cherenkov photons, are produced along the incident particle trajectories regardless of the presence of magnetic field. However, if a magnetic field is present, delta ray electrons, which will move in spiral trajectory, may re-enter, or circulate inside the aerogel as shown in Figure 2.2.1.9. Hence, they may emit more Cherenkov photons as shown on Figure 2.2.1.10. These Cherenkov photons are one of the major sources of background signal.

A comparison between contributions to photons detected on the photosensor from delta ray electrons and incident pions is shown on Figure 2.2.1.11. It shows that the number of photons emitted by delta ray electrons is roughly 100 times lower than the number of photons emitted by incident pions, in photon energy range from 2 to 3.4 eV. The acrylic Fresnel lens has a UV cutoff at 3.4 eV, so the number of photons from delta rays and incident pions that reach the detector plane drops another 2 orders of magnitude.

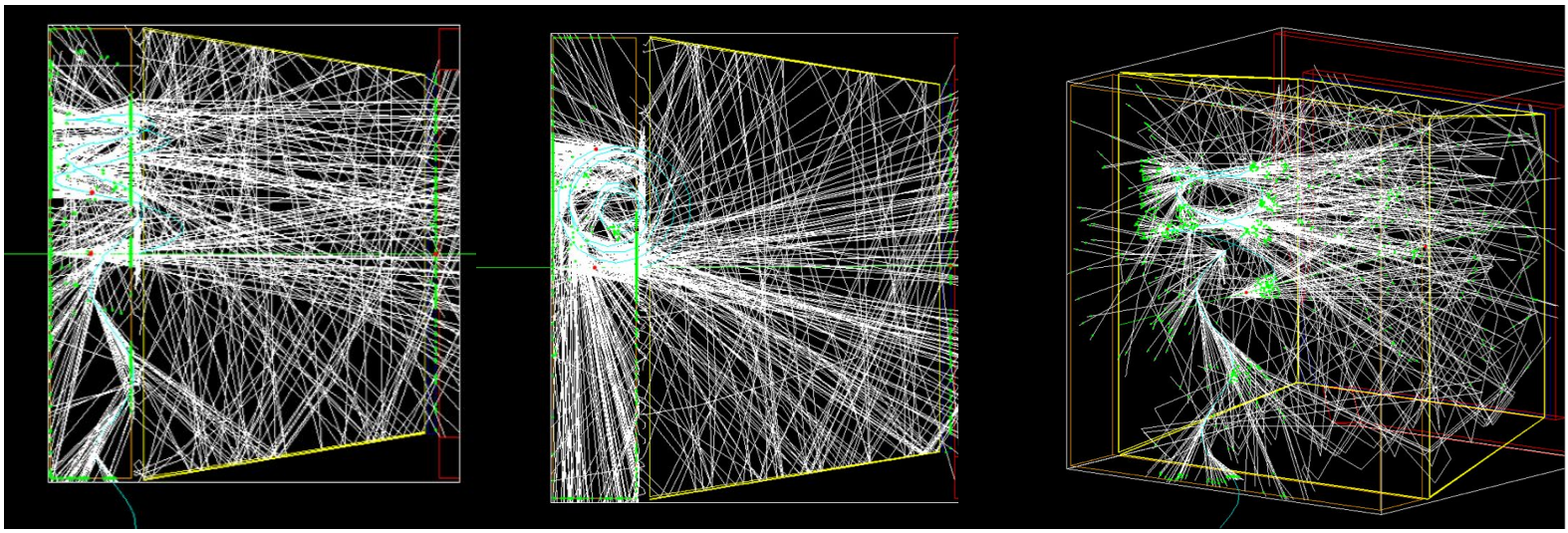

Figure 2.2.1.9. GEMC event display shows Delta Ray electrons (cyan) generated by single incident muon (green) move in spiral trajectory inside the aerogel due to the presence of magnetic field. Photons are shown in white. From left to right: side view, bird view, and front view of modular RICH detector.

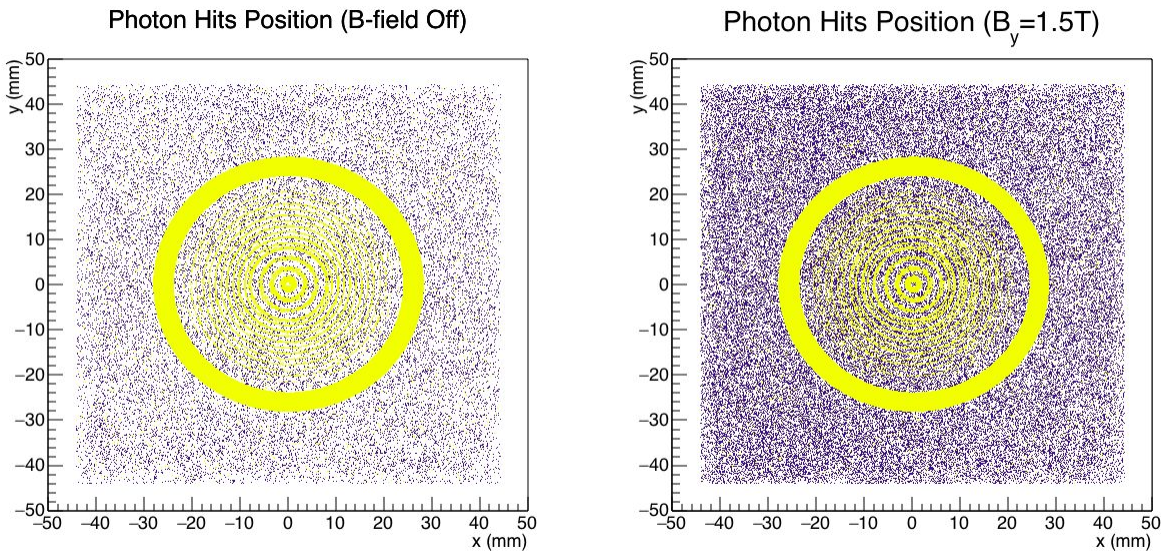

Figure 2.2.1.10. Photon hits on the photosensor with mother particle id which is shown in color. Cherenkov photons which are emitted by 100,000 incident particles, muon (yellow) with 9 GeV, form rings on the photosensor. Cherenkov photons emitted by delta ray electrons are indicated in purple. Plot on the left is from simulation without magnetic field. Plot of the right is from simulation with uniform 1.5-T y-direction magnetic field.

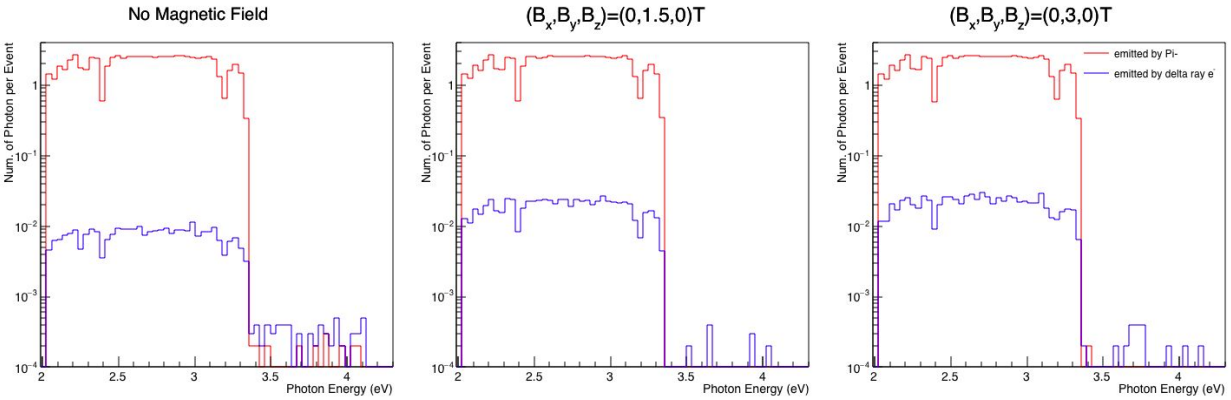

Figure 2.2.1.11. Photon energy distribution normalized to the total number of events. Red line represents the photons emitted by incident particles which are negatively-charged pions. Blue lines represent the background photons emitted by delta ray electrons. Plots from left to right are from simulations without magnetic field, with uniform 1.5-T y-direction magnetic field, and with uniform 3-T y-direction magnetic field, respectively.

2.2.2 Dual-radiator RICH

The goal for this detector is to provide good hadron separation (pi/K/p) up to 50 GeV/*c*. For this purpose a dual-radiator RICH (aerogel and gas) is needed.

An example of a dual-radiator RICH is the HERMES RICH [1]; it uses two radiators: aerogel (n = 1.03) and C_4F_{10} gas, in a mirror focusing configuration. In the design, a number of sigma of 4.65 in hadron identification was chosen, it provides a particle identification from 2 to 15 GeV/*c*. In the future, it will be a component of the SBS spectrometer at JLab, Hall A. Also, the LHCb experiment uses two RICH systems (the RICH1 is a dual-radiator aerogel and C_4F_{10} gas, the RICH2 consists of a CF_4 gaseous radiator) both with a focusing mirrors based optics. The RICH system of LHCb provides charged particle identification over a wide

momentum range, from 2 - 100 GeV/*c*. RICH1 covers the momentum range from 2 - 40 GeV/*c*, RICH2 covers the higher momenta up to 100 GeV/*c* [2].
Concerning the proximity configuration discussed in the section 2.2.2.1, we take advantage of the proximity (aerogel) RICH under development for the CLAS12 detector [3].

As to the proposed MEIC forward double-radiator RICH. The length of the device is chosen to be about 165 cm, given the space available in the MEIC design. Leading order semi-analytical calculations have been numerically implemented in order to suggest the optimal configurations to achieve the target performance. In the following sections the results for a proximity focusing configuration are shown; some of the obtained results have been used as a starting point also for the mirror based configuration (section 2.2.2.2).

2.2.2.1 Proximity focusing configuration

The first configuration considered has been a dual-radiator (aerogel and gas) with proximity focusing optics (see Figure 2.2.2.1). In the momentum range 3-10 GeV the separation of pions and kaons relies on an aerogel radiator. The optimal choice for the aerogel thickness turns to be between 3-4 cm; this as a result of the maximization of the expected cherenkov ring angular resolution (see Figure 2.2.2.2).
It is important to point out that, concerning aerogel, the photons in the UV region which are strongly scattered by the aerogel have to be absorbed using an optical filter placed after the aerogel radiator, likely in the form of a thin acrylic sheet, thereby reducing backgrounds.
The remaining space is filled with CF_4 (N_2 gas has also been considered as an alternative) gas serves as a threshold Cherenkov detector to veto pions up to 17 GeV (see Table 2.2.2.4). In the momentum range (10–15 GeV), the separation of kaons and protons will still rely on aerogel (given the thresholds see Table 2.2.2.4).

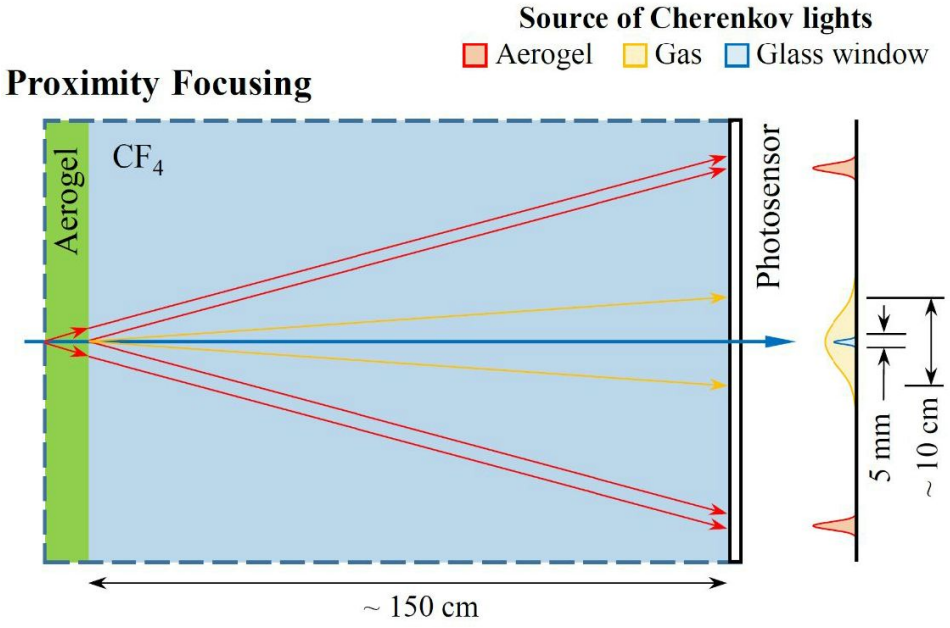

Figure 2.2.2.1: Options for a dual-radiator RICH detector for the EIC: a concept using proximity focusing.

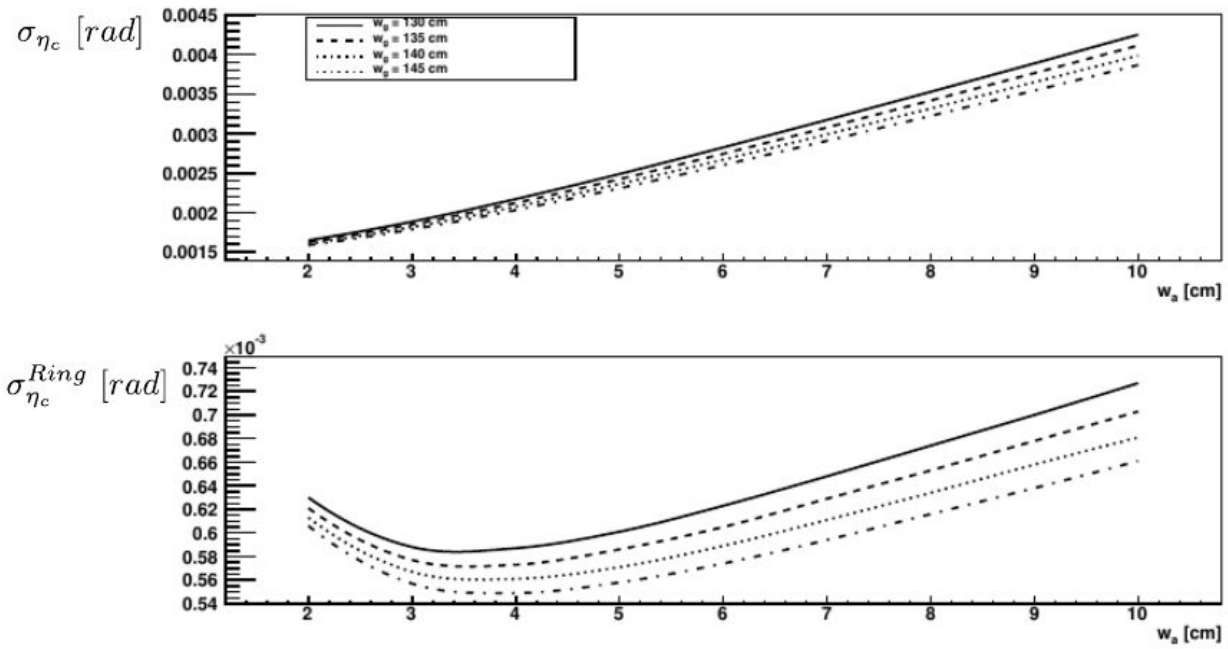

Figure 2.2.2.2. (Upper panel) The sigma on the Cherenkov angle (for n = 1.02, the maximum cherenkov angle is 0.198 rad) is plotted as a function of thickness of the Aerogel radiator (wa) for different thickness of the gas box (wg); (lower panel) is the resolution on the ring (the upper plot divided by the square root of the number of emitted photoelectrons) plotted as a function of the aerogel thickness. Both for a pion at <p> = 5 GeV/*c*.

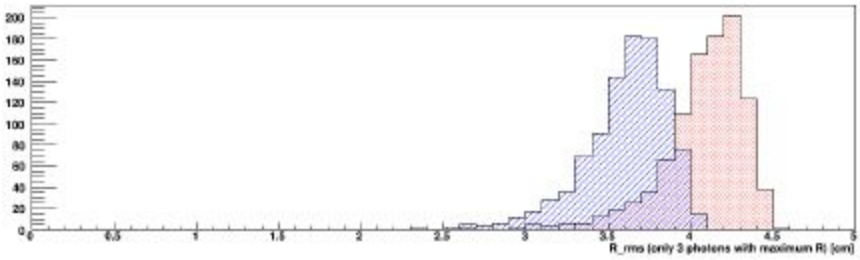

Figure 2.2.2.3. Histogram of mean radius of the spot of photons hits coming from CF_4 gas (for Pions in red and Kaons in blue); only 3 hits per spot with larger radius with respect to the track hit point have been selected.

Although the proximity design seems much simpler in terms of optics design and mechanical construction, the result is that this concept cannot guarantee hadron separation up to 50 GeV/*c* in momentum (see Tables 2.2.2.4 - 2.2.2.5).
Tables 2.2.2.4 - 2.2.2.5 show the separation power of the gas radiator used as an extended threshold cherenkov (we try to gain information from the shape of the gas photons spot in the detector plane, *i.e.,* considering only the three photon hits with highest radius with respect to the center of the spot); in the proximity case it is not possible to reconstruct a ring from the gas photons. This has been done for a typical ratio of the hadronic species, *i.e.* in SIDIS.

	Aerogel (n = 1.02) P_{th} (GeV/c)	CF_4 P_{th} (GeV/c)
π	0.69	5.53
K	2.46	15.94
p	4.89	31.66

Errors on θ_c Aerogel	mrad
Chromatic	1.3
Emission	1.5
Pixel size (3 mm)	0.8
σ_{tot}	2.1
Npe	~ 10

Table 2.2.2.4. (left panel) Threshold momenta for Aerogel and CF_4 gas. (right panel): main error contributions to the aerogel (n = 1.02) cherenkov angle (summed up in quadrature in the upper panel of Figure 2.2.2.2).

$$\pi/K = 10/1$$

P (GeV/c)	CF_4 K-π contamination (%)	CF4 π-K contamination (%)	N2 K-π contamination (%)	N2 π-K contamination (%)
20	0.3	3	0	0
25	2	22	1.6	16
30	5.7	57	4.6	46
35	8.6	86	7.6	76
40	10	100	10	100

$$\pi/K = 10/5$$

P (GeV/c)	CF_4 K-π contamination (%)	CF4 π-K contamination (%)	N2 K-π contamination (%)	N2 π-K contamination (%)
20	0	0	0	0
25	3	6	2	4
30	11	22	10	20
35	23	46	18	36
40	32	64	28	56

$$K/p = 1/2$$

P (GeV/c)	CF_4 p-K contamination (%)	CF_4 K-p contamination (%)
35	0	0
40	2	1
45	8	4
50	12	6

$$K/p = 1/2$$

P (GeV/c)	N_2 p-k contamination (%)	N_2 K-p contamination (%)
45	4	2
50	8	4

Table 2.2.2.5. Momentum range coverage of the gas radiator in terms of particle species contamination, given the particle species ratio; two possible choices of gas has been considered: CF_4 gas and N_2 gas. (Upper blue tables) K over pi and pi over K contamination, calculated considering the overlapping of the photons distributions in the photodetector plane (only the 3 largest radius photons per event considered); (lower gray tables) p over K and K over p distributions contamination in the photodetector plane (again only the 3 largest radius photons per event considered).

An alternative configuration that could be investigated in the future is a Fresnel lens focusing RICH detector (Figure 2.2.2.4).

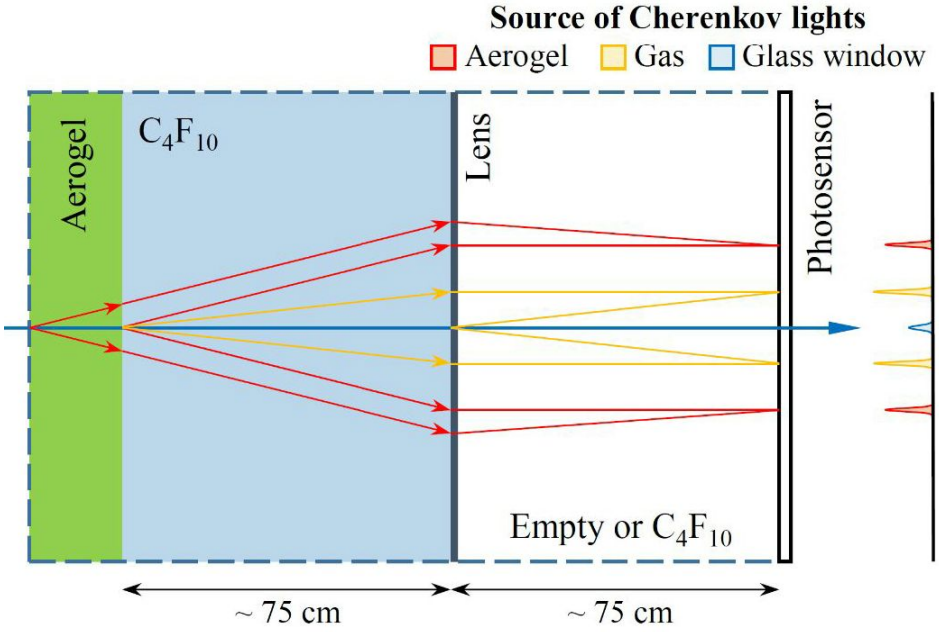

Figure 2.2.2.4: Options for a dual-radiator RICH detector for the EIC: a concept using a lens for focusing.

In this concept, an aerogel radiator is put in the front to cover the 3–10 GeV momentum range. Following the aerogel is a 75-cm long gas radiator volume containing C_4F_{10} to cover the 10–15 GeV range. The Cherenkov photons generated in each of the radiators are then focused by a Fresnel lens with a focal length of 75 cm. A super ultraviolet transmitting (SUVT) acrylic lens may be used to allow transmission of Cherenkov photons with wavelengths longer than 280 nm. With about 10–20 photoelectrons per Cherenkov ring, the required position resolution of the readout is a few millimeters in order to reach 4σ kaon/pion separation. Furthermore, because of the spatial resolution of the readout device, the photosensors don't need to be placed at the focal plane of the lens, but can be moved closer to reduce the total length of the detector.

2.2.2.2 Mirror-based focusing designs

The second studied concept is a mirror-based design. An LHCb-HERMES style layout, with the readout placed to the sides. The focusing mirror enlarges the momentum coverage capability, in particular for the CF_4 gas. The readout area in such a design can be more compact, and can be placed in the shadow of a barrel calorimeter. Since the readout is placed outside the radiator acceptance, the total thickness of this arrangement can be very small.

A simulation of this design has been constructed in GEMC framework (in Figure 2.2.2.6 - 2.2.2.7).

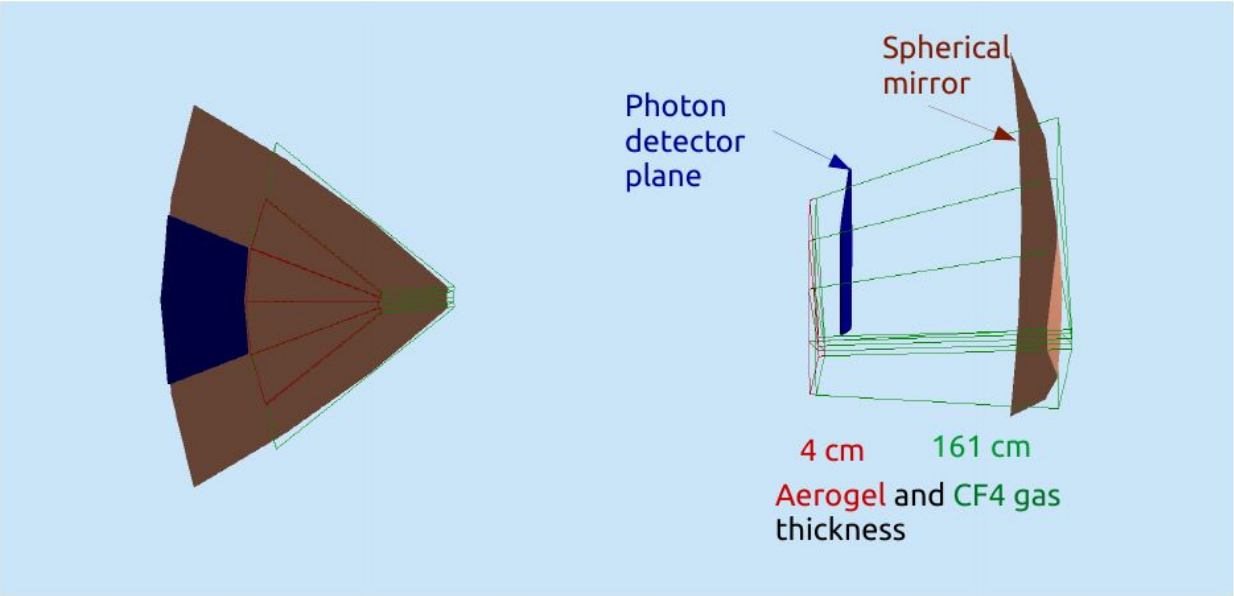

Figure 2.2.2.6. A frontal (left) and lateral (right) views of a sector of the mirror based RICH are shown.

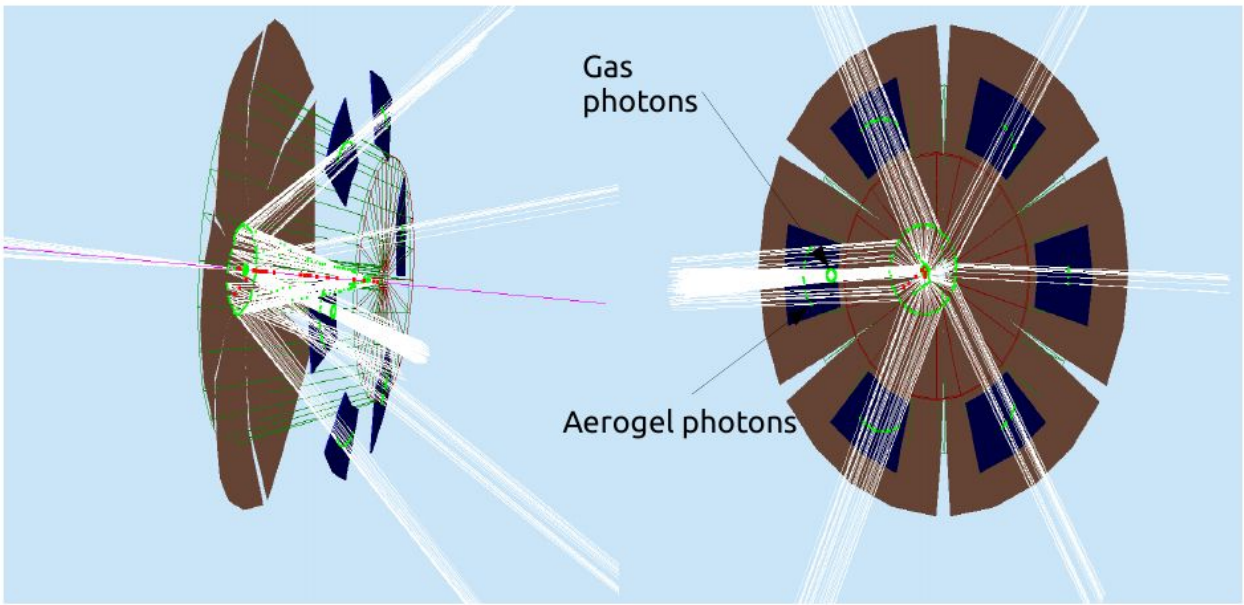

Figure 2.2.2.7. Full angle view of the mirror based RICH detector, with a pion event of momentum 30 GeV/*c*.

The angular dimension of each sector is a parameter that has to be fixed on the basis of analysis of the performance, that will be part of the future developments; such as the proper dimension of the photodetector plane (see Figure 2.2.2.7 for a preliminary analysis of the hits pattern on the detector plane).

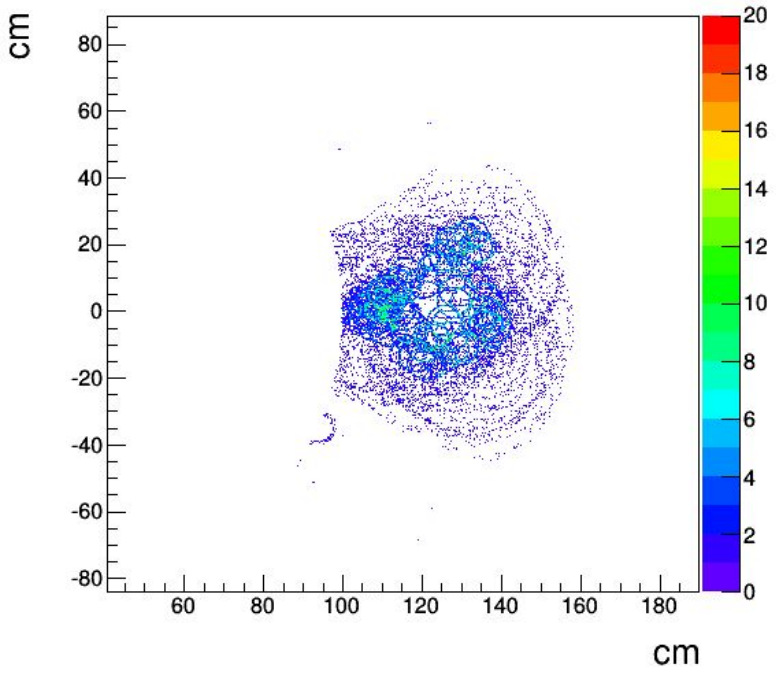

Figure 2.2.2.7: The spatial distribution of the photon hits on the detector plane.

A reconstruction algorithm has been implemented in order to study the output of the GEMC simulation of the mirror based dual-RICH, namely the inverse ray tracing algorithm implemented and used by the HERMES RICH collaboration [1].
A preliminary result of the algorithm applied on a sample of 1000 tracks per hadron (pi/K/p) at fixed polar angle (12.5°) and momentum (10 GeV/*c*) is shown in Figure 2.2.2.8; at the same polar angle and momentum (40 GeV/*c*) in Figure 2.2.2.9. The sigma of the cherenkov angle distributions shows a phase space dependence that will be studied in details. In Figures 2.2.2.8 - 2.2.2.9 one of the worst cases is shown.
In the analyzed simulated data the magnetic field is off and the pixel size effects due to the photodetector segmentation are not yet considered. Also, the effects of the delta rays (and the consequent background photons) are not yet subject of detailed study.

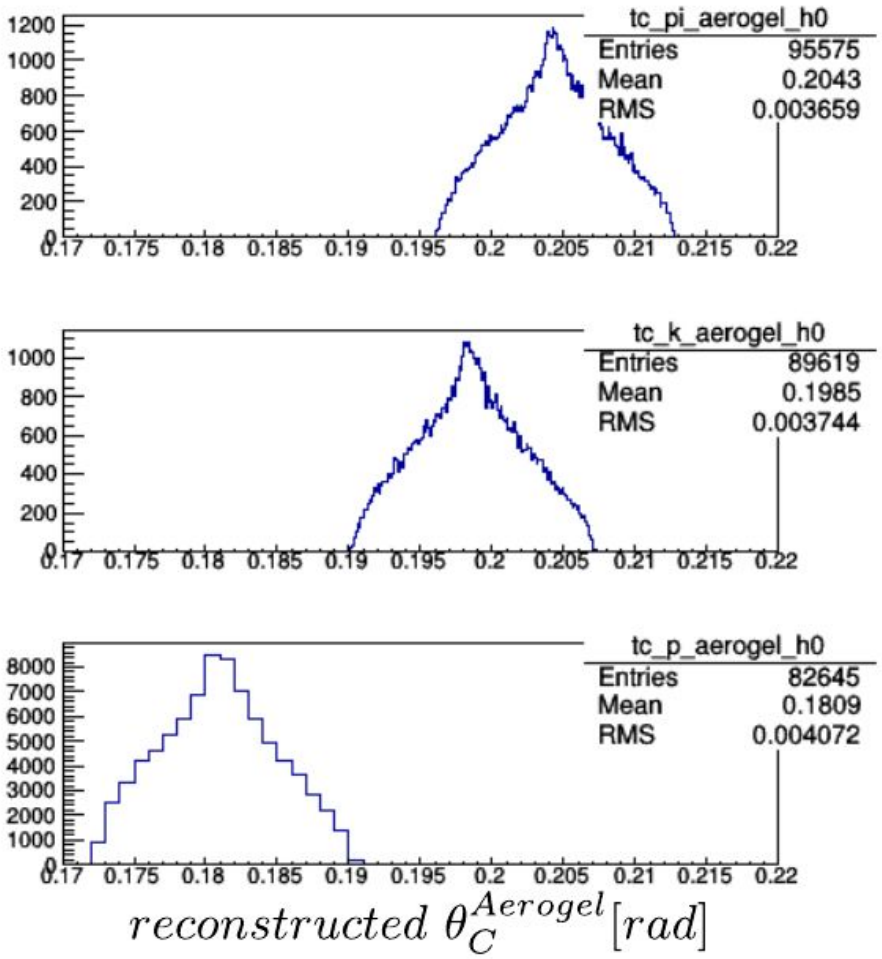

Figure 2.2.2.8: Distributions for the reconstructed aerogel cherenkov angles (sample of 1000 traks with momentum 10 GeV/*c* at polar angle of 25°) for π,K, p (from top to bottom).

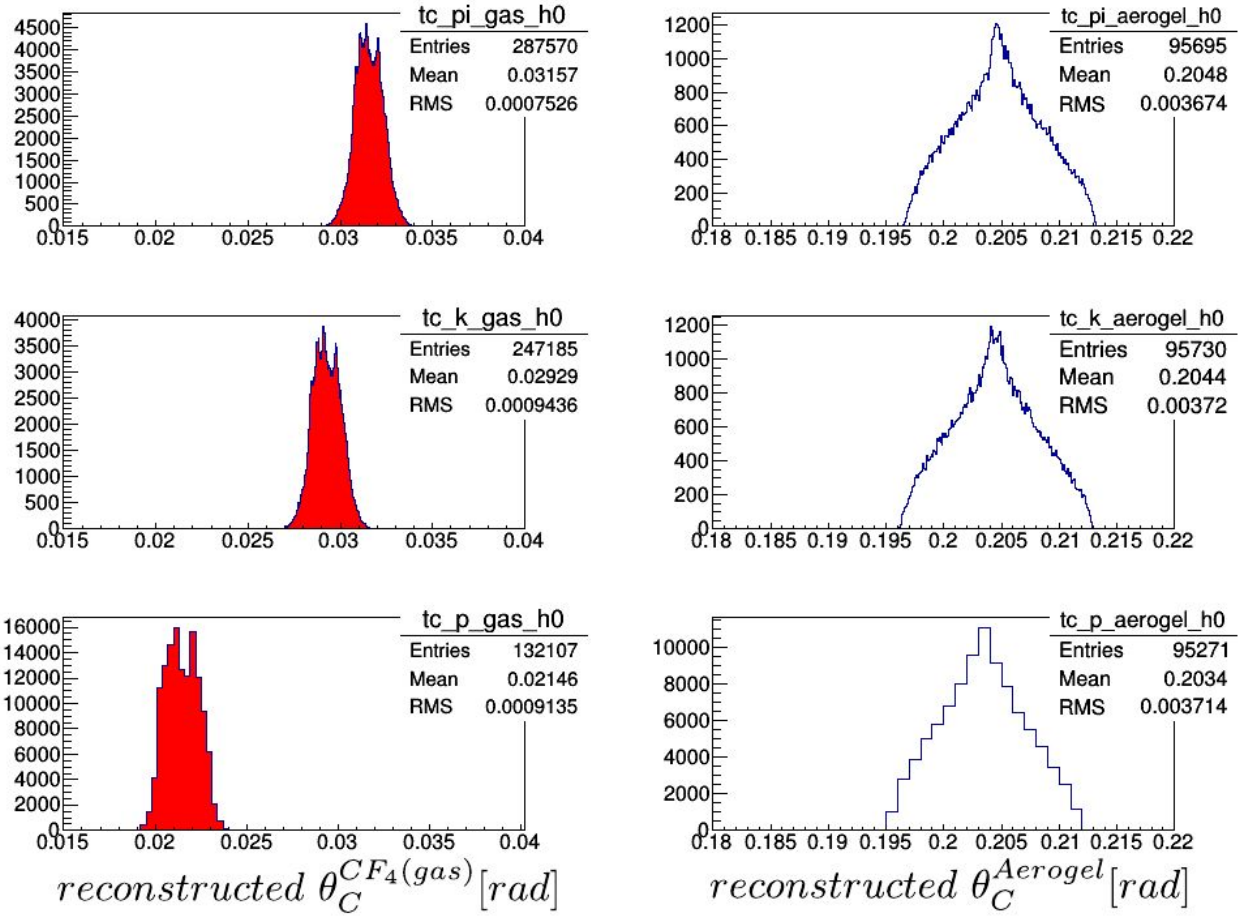

Figure 2.2.2.9: Distributions for the reconstructed gas (left panel) and aerogel (right panel) cherenkov angles (sample of 1000 tracks with momentum 40 GeV/*c* at polar angle of 25°) for π,K, p (from top to bottom).

2.2.2.3 Magnetic-field distortion effect for RICH

The RICH region is filled by a non negligible magnetic field (see Figure 2.2.2.10) and the charged hadron tracks are curving as they pass through the Cherenkov radiators. This introduces an additional source of error in the Cherenkov angle. The effect is proportional to the path length within the Cherenkov radiators, and therefore it becomes particularly important for the CF_4 gas.

An analytical-numerical method has been used to calculate the bending of the tracks within the MEIC magnetic field, with the aim of finding a field configuration that minimizes the effect in the RICH region.

In Figure 2.2.2.11 the error induced on the Cherenkov angle measurement is shown as a function of the polar angle and the momentum of the emitting particle.

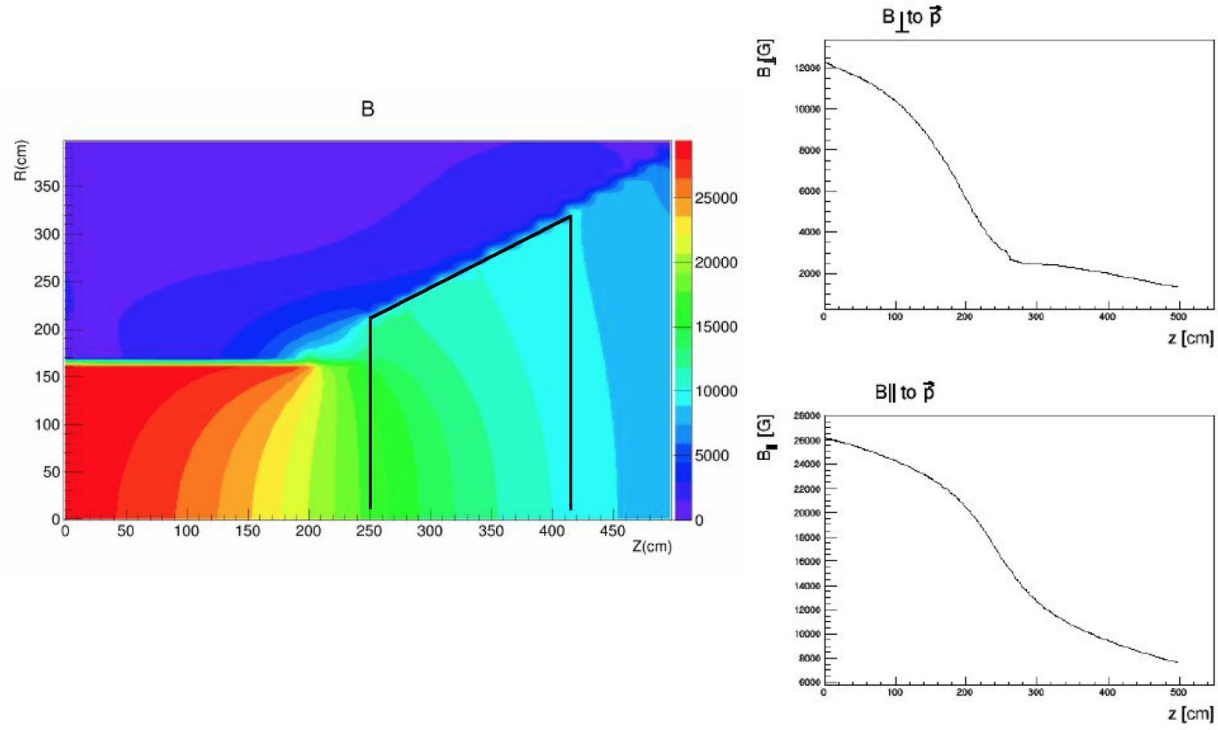

Figure 2.2.2.10: (left panel) Preliminary magnetic field map (in Gauss) in the (outgoing) ion side of the MEIC detector; the nominal region for the dual-radiator RICH detector is Z = [250,415] cm; (right panel) perpendicular and parallel components of the field to the momentum (for a track with polar angle of 25°).

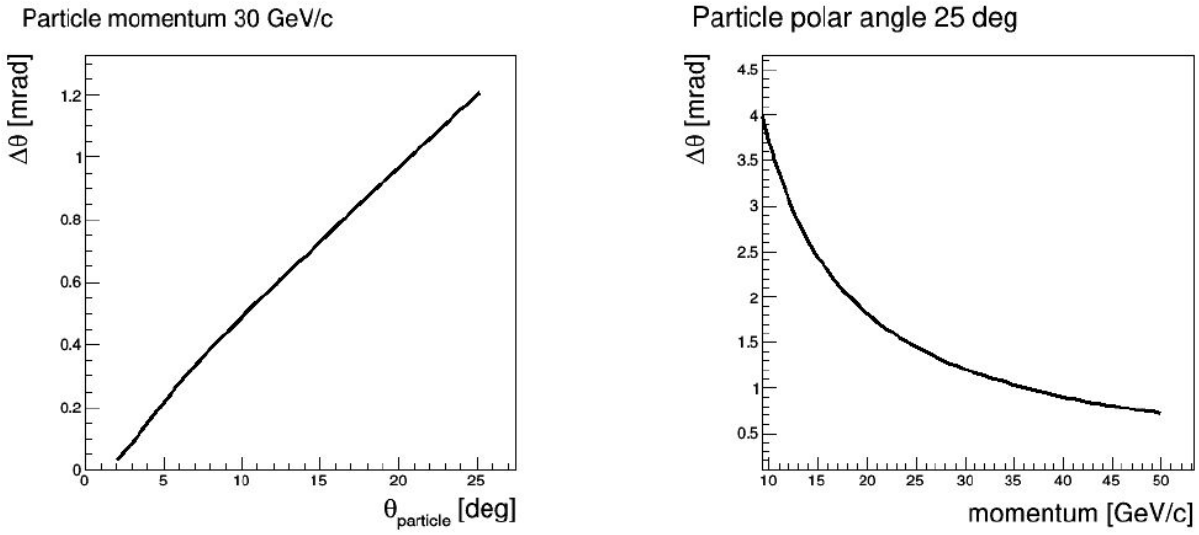

Figure 2.2.2.11: (left panel) induced error by the magnetic field on the Cherenkov angle measurement ($\sigma_B = \Delta\theta/\sqrt{2}$ per single p.e.) as a function of the polar angle of a charged pion of momentum 30 GeV/*c* (in the RICH region). (right panel) $\Delta\theta$ as a function of the track momentum at a fixed value of the polar angle, 25°.

To have a comparison with the other typical errors for a CF_4 gas Cherenkov radiator, *i.e.*, for a mirror based configuration, the contributions to the total error on the Cherenkov angle (per single p.e.), obtained from leading order calculations, are summarized in the following Table 2.2.2.12.
The contribution to the error due to the magnetic field (Figure 2.2.2.11) is of the same order as the others single p.e. error contributions in the range of the particle polar angle above 10°.
A final quantification of the error (for the aerogel and the gas radiator) would be from the GEMC simulation.

Errors on θ_c (CF_4 gas)	mrad
Chromatic	0.4
Emission	0.4 (from LHCb to be validated by gemc)
Pixel size (3 mm)	0.3
Magnetic (θ = 25°)	0.5
σ_{tot}	0.8
Npe	~ 20

Table 2.2.2.12: Main error contributions to the Chrenkov angle single p.e. measurement, the magnetic field contribution has been calculated for a track at 25° (polar angle) and of momentum 50 GeV/*c*.

2.3 What is planned was not achieved, why not, and what will be done to correct?

We had hoped to more fully evaluate the various options in the full detector environment, by analyzing key physics signals.

Future

2.4 What is planned for 2016 and beyond? How, if at all, is this planning different from the original plan?

2.4.1 Modular Aerogel RICH

2.4.1.1 Prototype

Prototype beam tests will be performed at Fermilab in April 2016. We plan this to result in a publication.

2.4.1.2 Simulation

- In future simulation, detector holder box (white wire frame shown in Figure 2.2.1.3) with set to ⅜ inch thick acrylic will be added in GEMC framework for a more realistic simulation.

- Since typical structure scale length of aerogel is between 3 to 5 nm, which is much smaller than the wavelength of the sensitive spectrum of the Hamamatsu modules H12700A (300 - 650 nm) considered in the modular aerogel RICH design, Rayleigh scattering will be a concern in detector performance. Therefore, Rayleigh scattering will be implemented in the simulation, and its effect on distribution of background photon hist will be quantified.
- Refine Likelihood analysis technique by adding parameters such as photon, and photoelectrons efficiency will be included next.
- integrate Modular RICH detectors into the MEIC framework.

2.4.2 Dual-radiator RICH

2.4.2.1 Simulation

- Finalize the study of the mirror-based configuration: refinement of the optical parameter used in the simulation on the basis of the recent results available in literature, study of the photon yield and of the photodetector shape, definition of reconstruction algorithm (more than one method, with a comparison of the performances) and performances.
- Explore other possible configurations (i.e. double bounce mirror configuration); a comparison in terms of costs and performances.

2.4.2.3 Photocathode development

At Los Alamos, contact has been made with members of a group in the Accelerator Division who specialize in the development of photocathodes. They have expressed interest in proposing a joint LDRD project for the development of GEM-based photocathodes, for the Spring round of submittals.

2.5 What are critical issues?

No funding is allocated for travel to Fermilab to participate in the beam test.

2.6 Additional Information?

None

2.7 Manpower

2.7.1 Modular Aerogel RICH

Cheuk-Ping Wong (GSU student) supported by eRD14 funds
Sawaiz Syed (GSU)
XiaoChun He (GSU)
Zhiwen Zhao (Duke)
Jin Huang (BNL)
Martin Purschke (BNL)
Marco Contalbrigo (INFN)
Maurizio Ungaro (JLab)

2.7.2 Dual RICH

Alessio Del Dotto (JLab, INFN postdoc) supported by eRD14 funds
Jin Huang (BNL)
Zhiwen Zhao (Duke)

2.7.3 GEM photocathodes

Hubert van Hecke (LANL)
Matt Durham (LANL)
Doug Fields (UNM)

2.8 External Funding

The design and construction of the modular detector prototype is funded by internal funds at GSU, and aerogel blocks are provided by Jlab and LANL.
If the LANL LDRD proposal is successful, the photocathode work will be carried out with the LDRD funds. The simulation studies were performed using RD14 funds at GSU and JLab.

Publications

2.9.1 Modular Aerogel RICH

- Presentation by Cheuk-Ping Wong, APS April Meeting 2015 at Baltimore.
- The test beam results is expected to produce a submission to NIM.

References

[1] Akopov, Norair, et al. "The HERMES dual-radiator ring imaging Cherenkov detector." *Nuclear Instruments and Methods in Physics Research Section A: Accelerators, Spectrometers, Detectors and Associated Equipment* 479.2 (2002): 511-530.

[2] Adinolfi, M., et al. "Performance of the LHCb RICH detector at the LHC." *The European Physical Journal C* 73.5 (2013): 1-17; Alves Jr, A. Augusto, et al. "The LHCb detector at the LHC." *Journal of instrumentation* 3.08 (2008): S08005; Nobrega, R. Antunes, et al. "LHCb reoptimized detector design and performance: Technical Design Report." (2003): x-127.

[3] Baltzell, N., et al. "Test of the CLAS12 RICH large scale prototype in the direct proximity focusing configuration." *arXiv preprint arXiv:1509.02818* (2015).

3. DIRC

Contact: P. Nadel-Turonski <turonski@jlab.org>

Abstract

A radially-compact subsystem providing particle identification (e/π, π/K, K/p) over a wide momentum range is an essential requirement for the central detector of an Electron-Ion Collider (EIC). With a radial size of only a few cm, a Detector of Internally Reflected Cherenkov light (DIRC) provides a very attractive solution. The R&D undertaken as part of the PID consortium (eRD14) effort builds on the results obtained during the eRD4 project, which had the goal of investigating feasibility of building a high-performance DIRC that would extend the momentum coverage well beyond state-of-the-art, up to 6 GeV/*c*.

Based on Geant4 simulations, validated through test beam results, we now consider this goal to be achieved using an approach with BaBar-like boxes with narrow bars, each coupled to an advanced spherical three-layer lens, and one fused-silica compact (30-cm deep) expansion volume per box. The current work is focussing on the experimental evaluation of the properties of the 3-layer lens prototype, which was designed in FY13 and procured in FY14. Experimental tests of the new lens have included measurements in test beams at GSI and CERN using the full PANDA Barrel DIRC prototype setup. Analysis of the data collected in the 2015 CERN test beam is currently ongoing. In addition, two types of test bench measurements are being prepared for the 3-layer lens. The first is the mapping of the focal plane in an optical setup build at ODU. The second is the radiation hardness test in two setups build at CUA.

Past

3.1 What was planned?

Last year, a baseline design of the DIRC system envisioned for the EIC was established, implemented, and studied in Geant4 simulations (see Fig. 3.1). However, since not all of the components of the full DIRC baseline design are available (such as sensor with small pixels, *etc.*), the validation of the simulation package, used to optimise the design and to determine the performance, was done by simulating key DIRC@EIC components in a geometry corresponding to the currently available detector prototypes, and by comparing to test beam data. Here, the most important item is the special 3-layer lens that was developed in collaboration with the GSI PANDA DIRC group. Schematics and photos of the prototype lens are shown in Fig. 3.2.

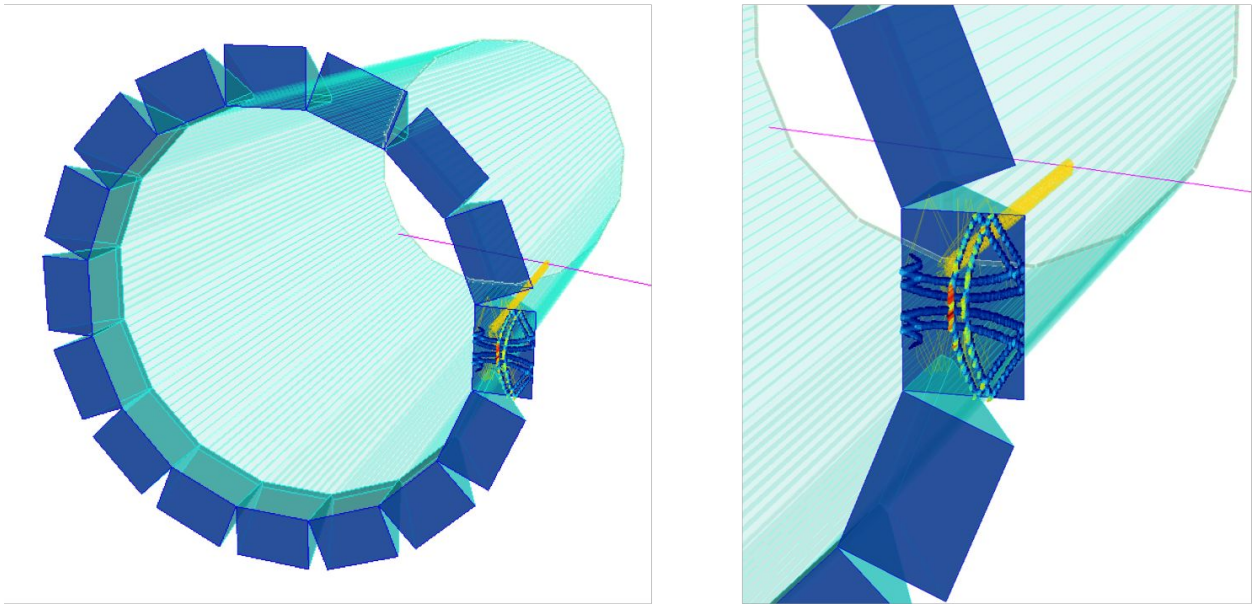

Figure 3.1. A Geant4 implementation of the tentative geometry of a lens-based, high-performance DIRC for the EIC with narrow bars and a solid fused silica prism. The simulated event shows the primary charged track in magenta, with Cherenkov photons in yellow.

Establishing the properties of the 3-layer lens prototype is thus the most important task this year. This includes the preparation and two measurements on test benches, the mapping of the focal plane and the radiation hardness of the middle layer of the lens (which is not made of radiation hard fused silica), and the taking and analysis of test beam data - for which G. Kalicy and L. Allison joined the GSI PANDA DIRC group at CERN in August 2015. The analysis of the data collected in CERN was a key activity for the first part of this year.

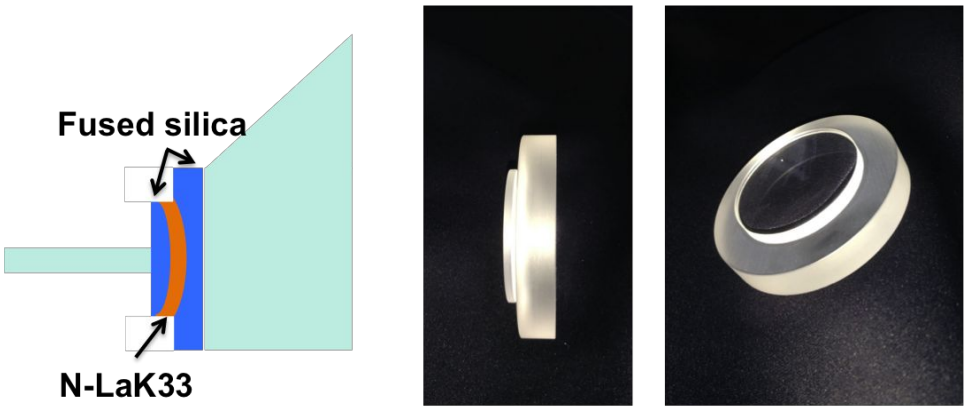

Figure 3.2. Schematic diagram and two photos of the prototype three-layer spherical lens.

3.2 What was achieved?

3.2.1 Performance of 3-component lens in test beam

Cooperation with the PANDA Barrel DIRC group provided the opportunity to evaluate the performance of 3-component lens in a real particle beam experiment. The full PANDA Barrel DIRC system prototype shown in Fig. 3.3 was developed at GSI and transported to the T9 area at the CERN PS. A height-adjustable table with a precision rotating stage is used to place the prototype into the beamline and to adjust the position and polar angle of the radiator bar or plate relative to the beam. The radiator is placed into a holder on an X/Y stage, which allows precision alignment of the radiator relative to the lens and the expansion volume. A mirror was placed at the opposite end of the bar. A plastic fixture places the sensors into an array structure at the back wall of the prism. The sensors, prism, lens, and radiator are coupled using optical grease. The radiator, lens, expansion volume, and front-end readout electronics are placed in a light-tight box, cooled by a forced air flow.

Modular design of the prototype allowed to easily exchange several components in between runs and to compare their impact on the prototype performance. The PID performance of the DIRC detector is driven by the photon yield and the single-photon Cherenkov angle resolution. Therefore, these parameters are used to quantify the performance of each design. The same simulation package that was used to study DIRC@EIC was also used for designing the prototype, monitoring the measurements, and analysing the data.

The arrangement of the components that were put in the beam is shown in Fig. 3.4. The trigger was provided by two round scintillator paddles located in front and behind the prototype. In addition, the coincidence signal of the two scintillators was distributed over the readout boards, to provide time corrections in the analysis. Time-of-flight (TOF) detectors were installed at the beginning and at the end of the beamline and provided clean pion/proton tagging up to 7 GeV/*c* beam momentum.

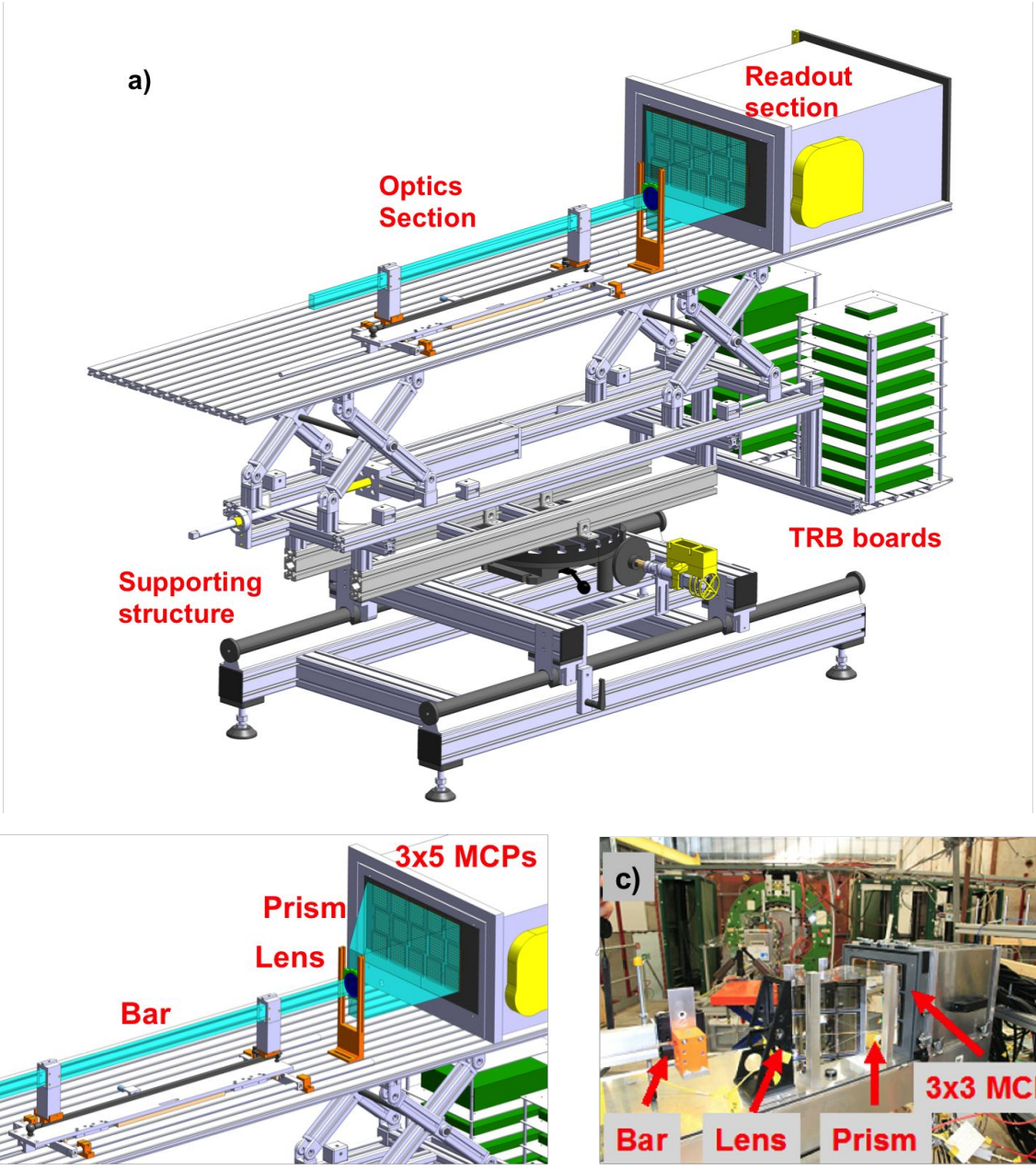

Figure 3.3. Layout of the PANDA barrel DIRC prototype from the summer of 2015. Overview of components (a) and close-up of the imaging region (b) showing the prism expansion volume, focusing lens, and radiator plate. Photo of the prototype at CERN.

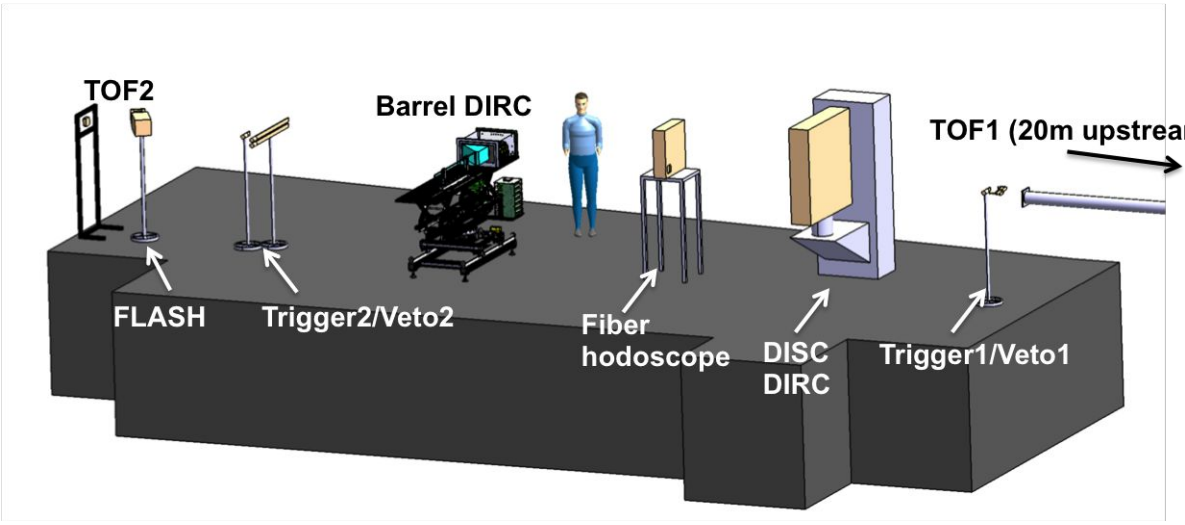

Figure 3.4. Arrangement of the prototype elements used in the 2015 test beam at CERN.

The first phase of the analysis was dominated by calibration of the data, establishing the time resolution of the setup, and optimising the event and hit selection. At this stage of the analysis, in the process of event selection, coincidence of both triggers and any pixel of both TOF MCPs is required. The first stage of hit selection is performed on corrected hit time (see example for the single pixel on Fig. 3.5). The correction comes from reference time, information obtained from data taken with the PiLas and Picoquant laser calibration system and simulation.

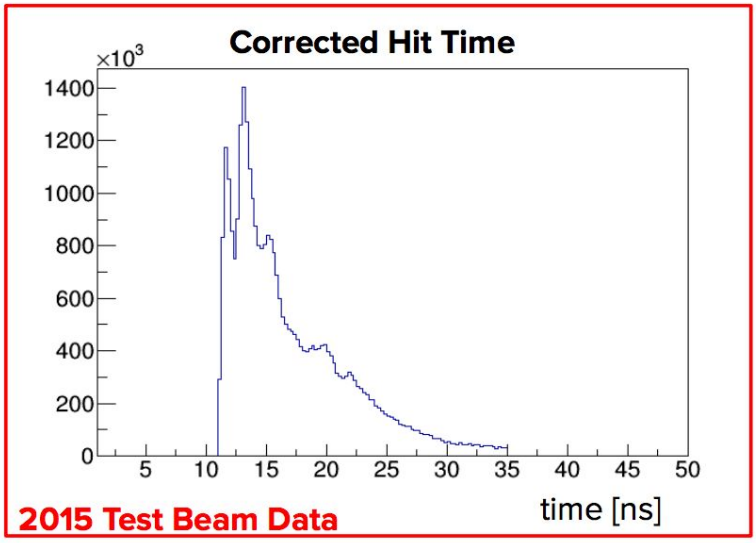

Figure 3.5. Corrected hit time of an example pixel.

Several different focussing options were tested during the 2015 test beam campaign. Below we discuss results only for data taken with the 7 GeV/*c* hadron-rich beam, with two focussing options, shown in Fig. 3.6, the standard air-gap lens and the 3-layer compound lens. We selected a few different beam/bar polar angles, representing most extreme cases - the beam going towards the mirror, perpendicular to the bar, and towards the readout end.

Comparison to other used lenses and the other measured configurations of the setup will be analyzed in the second part of the year.

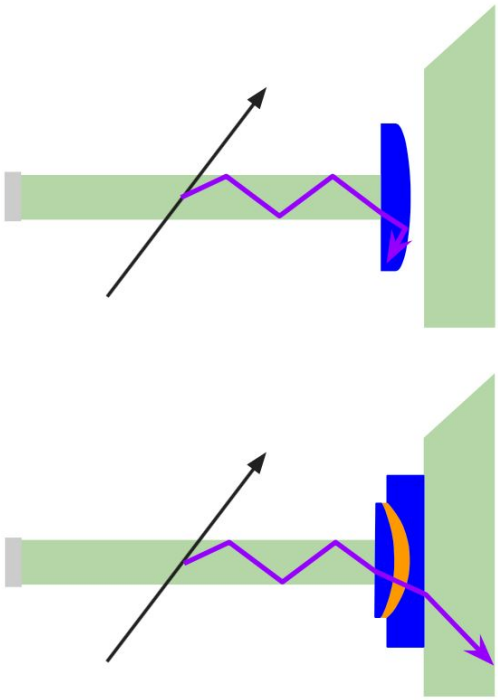

Figure 3.6. Schematic diagram of photon propagation from the bar to the prism for the configuration with an air-gap lens (top) and the three-component lens (bottom) .

The difference between the performance of the air-gap lens and the 3-layer lens is visible already on the occupancy distribution, shown in Fig. 3.7 for a 125° beam polar angle. The hit pattern for the air-gap lens becomes faint much sooner as photons with steeper angles do not get transported. When the 3-layer lens is used, photons even with very steep angles are preserved and one can see clear wings of the ring image even on the last column of MCPs. Although the hit patterns are complicated with overlapping segments due to reflections from the top, bottom, and sides of the prism, these features are in good agreement with the prediction from simulation. The background, visible as violet pixels around the main ring segments, comes from processes like δ-electrons, MCP-PMT dark noise, scattered photons, and charge sharing. Light green pixels correspond to zero hits per pixel. These are due to dead electronic channels and, in the case of the middle bottom MCP-PMT, a disconnected TRB-MCP cable.

The geometric reconstruction algorithm was used to quantify the Cherenkov angle resolution. In Geant simulation a monochromatic photon source was placed inside the DIRC bar close to the readout end and photons were emitted over the entire phase space. After propagation of the rays through the lens and expansion volume, a look-up table is created associating each MCP-PMT pixel with the center of the bar end surface with a specific unit wave vector $\hat{k}$ (see Fig. 3.8). In addition, the time of propagation for each photon path is saved. A separate look-up table is created for photons with a combination of 0, 1, 2, or 3 reflections off the sides, top, and bottom, inside the prism. The reconstruction of the

detected pattern of Cherenkov photons in data is done by calculating a Cherenkov angle θ_c from $cos\theta_C = \hat{k} \cdot \hat{p}$ ($\hat{p}$ is the beam unit vector in the bar coordinate system) for each detected photon. The value of θ_C is histogramed, including the 8-fold ambiguity from all possible reflections off the sides, top and bottom, and end of the DIRC bar and all additional possible paths in the prism. Reconstructed false photon propagation paths generate combinatorial background around the main peak in the θ_C distribution but a clear peak remains at the correct angle. The single-photon Cherenkov angle resolution is obtained by fitting a Gaussian plus polynomial to the θ_C histogram. Some of the false photon paths can be rejected by a time cut, suppressing some of the combinatorial background. This time cut is performed on the distribution of difference between the measured propagation time of the photons and the expected propagation time obtained from the look-up table.

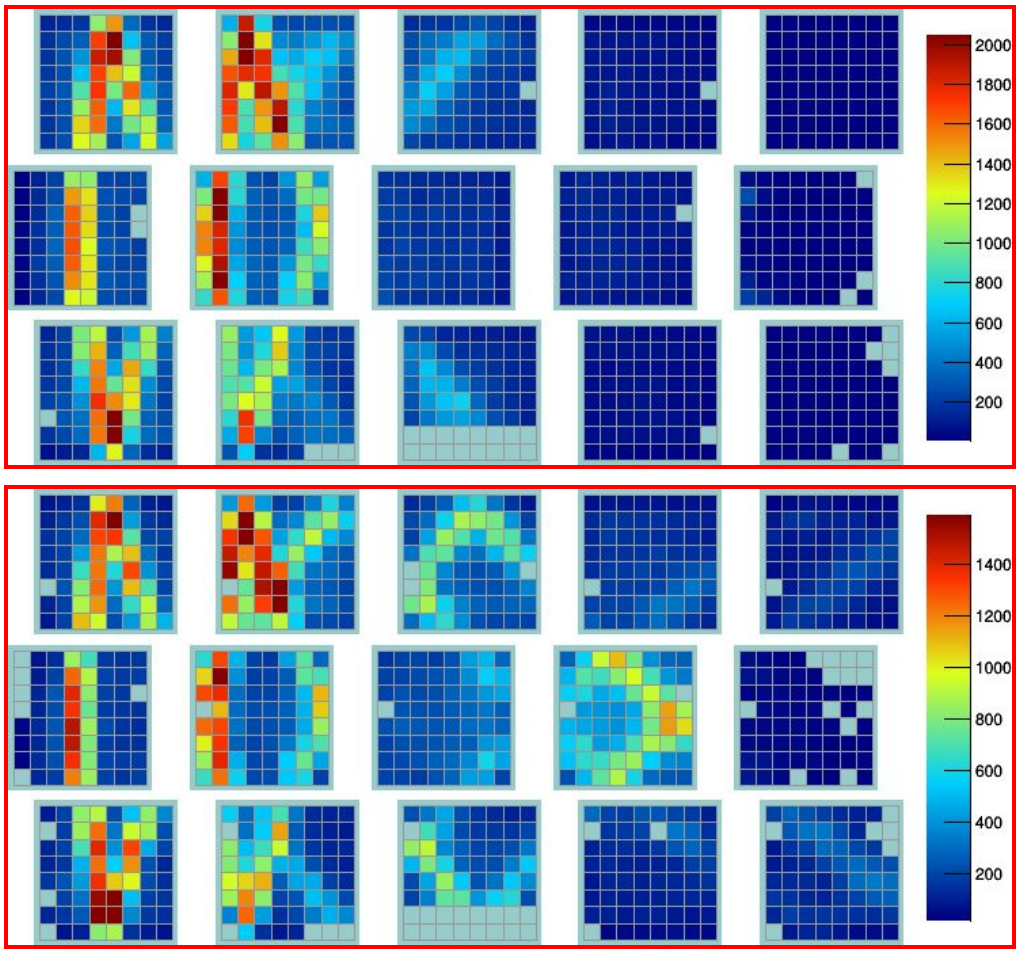

Figure 3.7. Distribution of the number of hits per MCP-PMT pixel in the 2015 test beam data for a configuration using an air-gap lens (top) and a 3-layer lens (bottom).

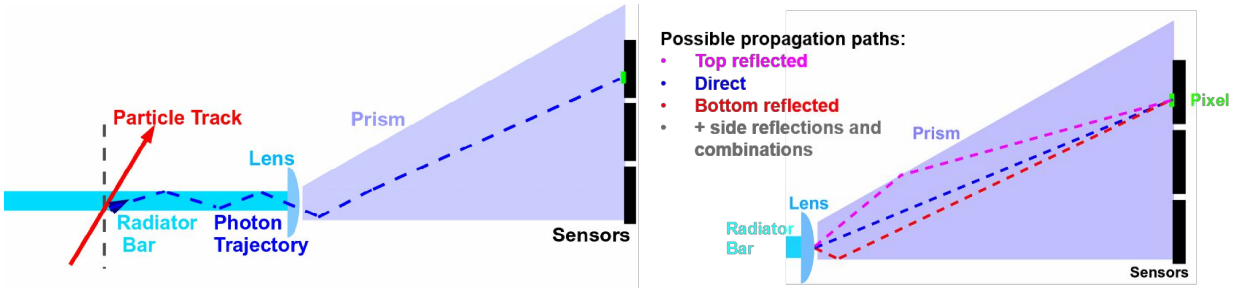

Figure 3.8. Schematic diagram of the reconstruction concept, with one example photon track emitted from a particle. The direction vector k is an estimator of the origin vector k_{org}, and is used to reconstruct θ_C. On the right, three examples for possible propagation paths of the photon from the center of the bar end to one of the pixels are shown.

An example distribution of the reconstructed single-photon Cherenkov angle for simulated 7 GeV/*c* protons with a polar angle of 125° for a configuration with a 3-layer lens is shown in Fig. 3.9a. The same distribution after a ±2ns time cut is shown on Fig. 3.9b. The fit is much more stable after the cut and the resolution got slightly better. The importance of the time cut varies for different beam polar angles.

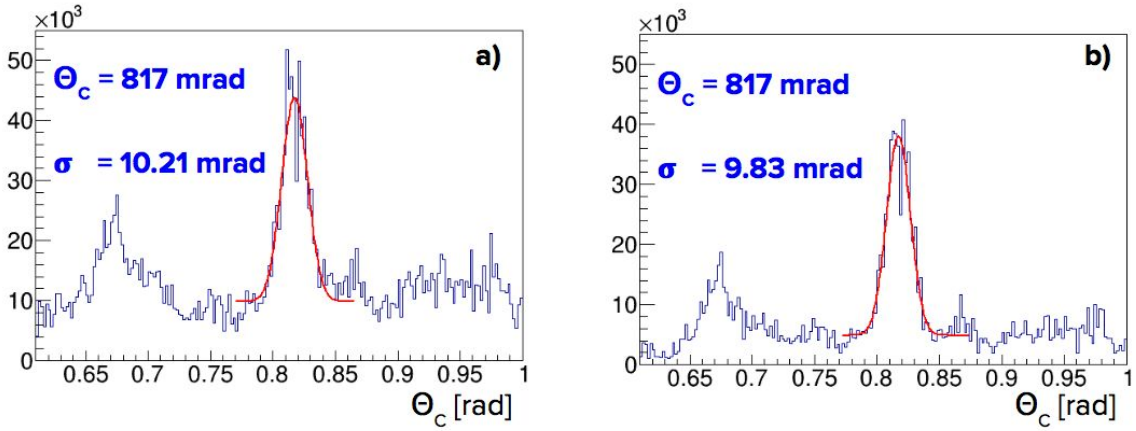

Figure 3.9. Reconstructed single-photon Cherenkov angle for simulated data using Geant4. 7 GeV/*c* protons are entering the setup with 3-component lens at a 125° angle. Left: without time cut. Right: with 2-ns time cut (measured - expected).

A comparison of the reconstructed single-photon Cherenkov angle for the configuration with the air-gap lens and the 3-component lens, from experimental data, is shown in Fig. 3.10. In both cases the prototype was placed at 60° relative to the 7 GeV/*c* beam. Only protons were selected for this analysis (tagged with a TOF system). As expected, the single-photon resolution is better by ~2 mrad for the 3-layer lens, also the reconstructed angle is closer to the expected 817 mrad for 7 GeV/*c* protons.

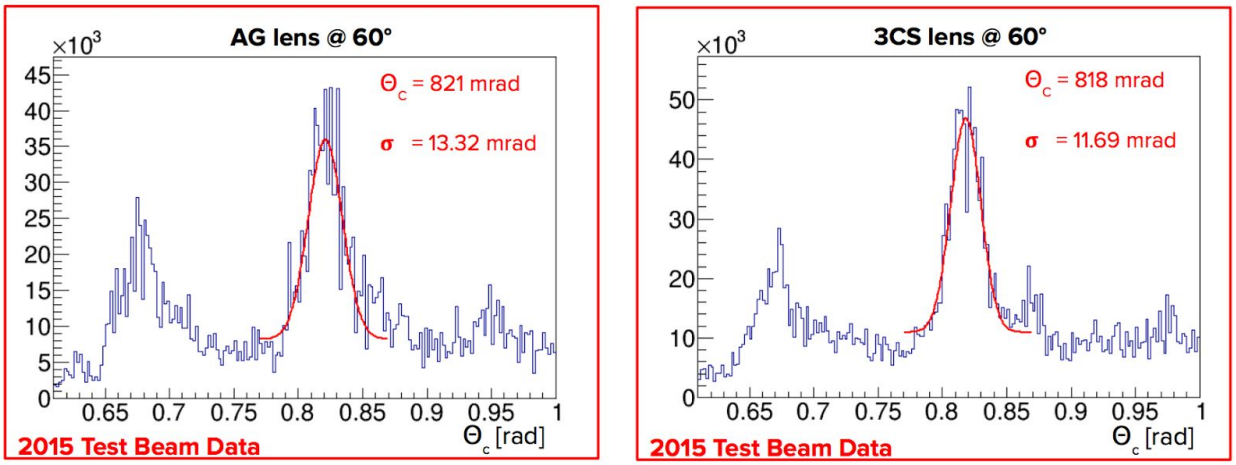

Figure 3.10. Reconstructed single-photon Cherenkov angle from the 2015 CERN beam data for a 7 GeV/*c* momentum and 60° polar angle. Left: Setup with air-gap lens. Right: Setup with 3-component lens.

A similar improvement of the single photon resolution for the configuration with the 3-component lens is shown for different polar angles in Fig. 3.11. The missing point at 90° for data taken with the air-gap lens is due to insufficient statistics of detected photons due to internal reflection at the air gap (see Fig. 3.11 right).

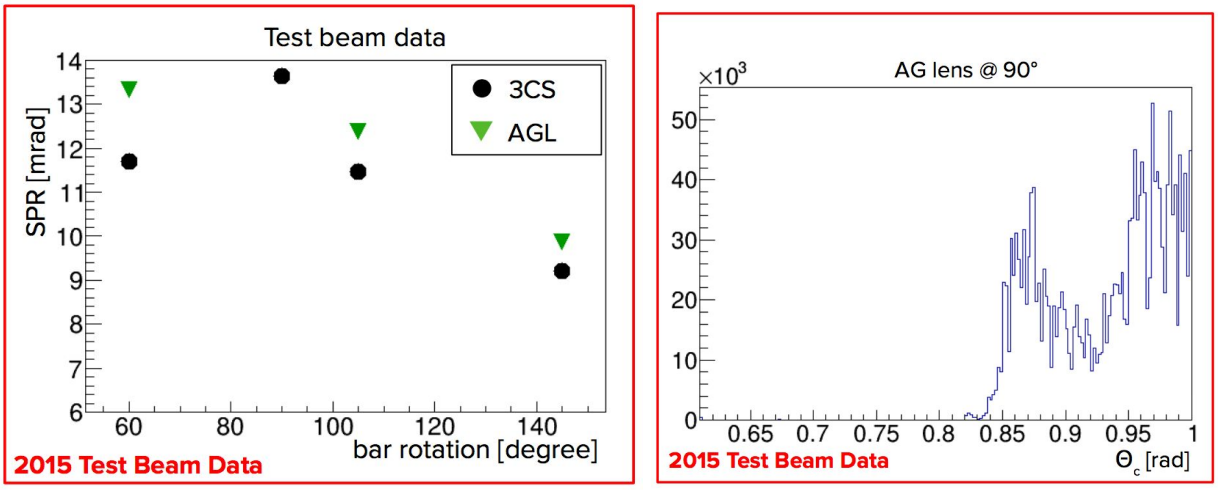

Figure 3.11. Left: Single-photon Cherenkov angle resolution as a function of beam polar angle for the 2015 CERN beam data. Green points: Setup with air-gap lens. Black points: Setup with 3-component lens. Right: Reconstructed single-photon Cherenkov angle for 90° polar angle and air-gap lens setup.

To determine the photon yield, cuts were placed on the reconstructed θ_C vs time (measured - expected) distribution (see example in Fig. 3.12) to subtract background hits from electronics noise as well as from scattered photons and photons from δ-electrons.

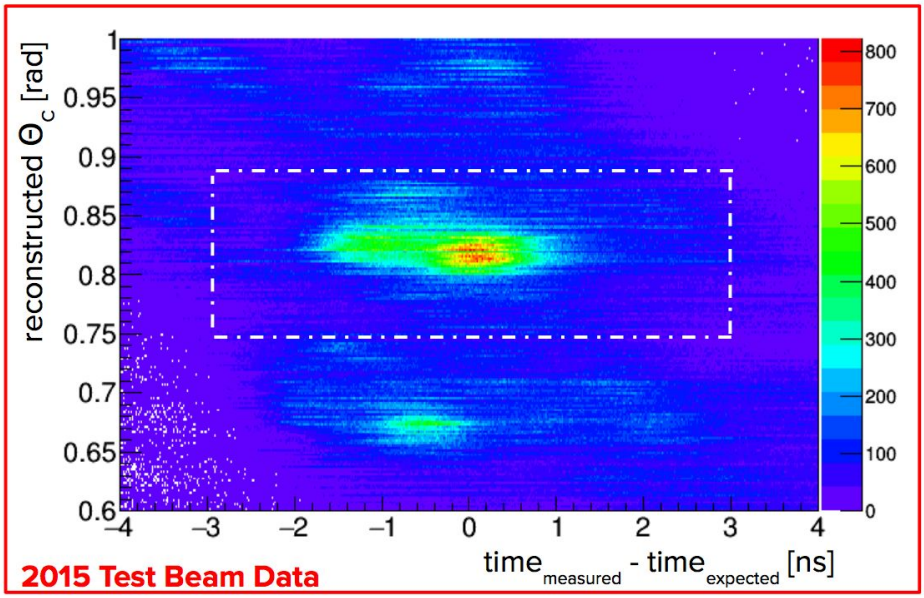

Figure 3.12. Cut on reconstructed single-photon Cherenkov angle as a function of time (measured - expected) for 2015 CERN beam data. 7 GeV/*c* beam is entering the setup at 90° angle (setup with air-gap lens).

The comparison between the photon yield for configurations with the air-gap lens and with the 3-layer lens is shown for several beam polar angles in Fig. 3.13. As expected from the simulation, the 3-layer lens improves the photon yield by about 10% for forward or backward angles, but the biggest difference is observed around 90°.

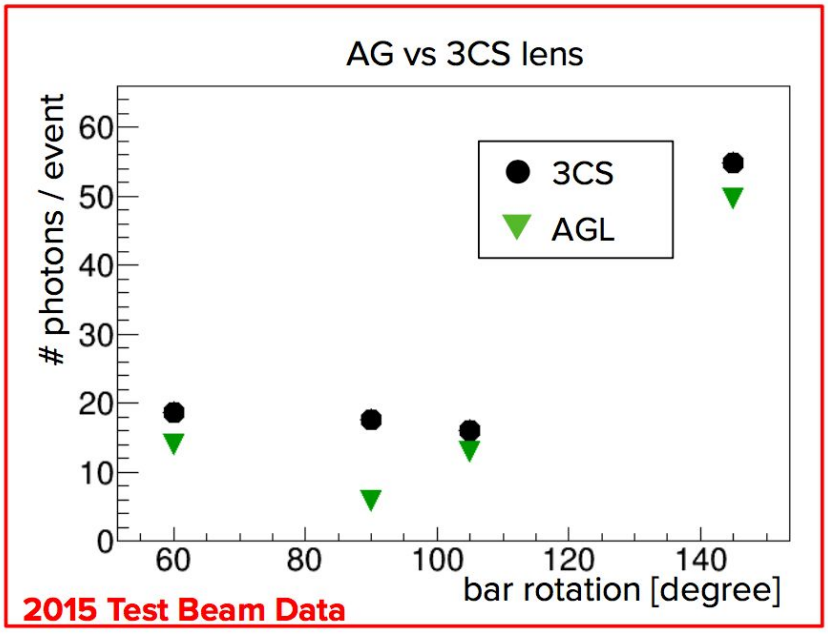

Figure 3.13. Photon yield as a function of beam polar angle for the 2015 CERN beam data. Green points: Setup with air-gap lens. Black points: Setup with 3-component lens.

3.2.2 Radiation hardness test

The determination of the radiation hardness of materials that will be used in the EIC detector is an important requirement. Synthetic fused silica, which is used for most of the optical components in the DIRC, was already extensively tested for the BaBar and PANDA experiments and proved to be radiation hard. However, in the 3-layer lens the middle layer is made of a high-refractive-index glass NLak33, which has yet to be tested for radiation hardness. During the fabrication of the prototype lens, three of the five purchased 3-layer lenses were covered with anti-reflective coating (see Fig. 3.14), which should be also tested for radiation hardness. That is why several samples of pure NLak33 material (see Fig. 3.15) were obtained from Schott so that it can be irradiated in parallel with one of the coated lenses.

The irradiation test is in the final stages of preparation. Both items will be irradiated in 10 steps, each time by 1 krad. In between every step, the transmission properties of the lens and the NLak33 sample will be measured to quantify the impact of the irradiation. The irradiation will be performed either at JLab or at CUA. In the first case, a ^{137}Cs source with dose rate of 0.25 krad/h at the location of the irradiated samples will be used, and in the second, an X-ray setup with energies up to 160 keV. Regardless of where the irradiation is performed, the transmission measurement will be done in collaboration with the Vitreous-State Laboratory at CUA, in a setup with a reproducibility of 0.2%.

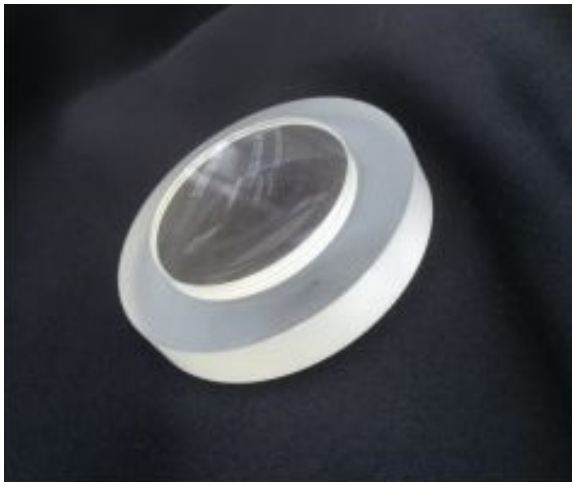

Figure 3.14. Antireflective coated 3-layer lens prototype.

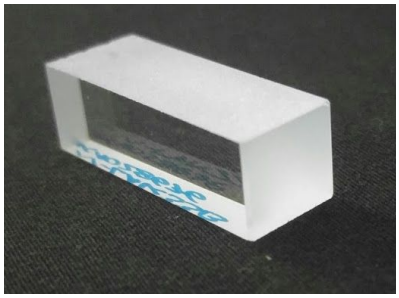

Figure 3.15. Sample of pure NLak33 material.

3.2.3 Measurement of the shape of the focal plane

The shape of the focal plane proved to be an important aspect of the single-photon resolution in the PANDA Barrel DIRC R&D program. The focal planes of the standard spherical lens and a prototype two-layer high-refractive index spherical lens were studied in Geant4 simulation. It was also measured in the laboratory to verify the parameters and to evaluate how important the curved surface of the focal plane is for the DIRC resolution. Based on studies with Geant4 simulation and ZEMAX software, a newly designed 3-layer lens is expected to resolve issues of aberrations and have a flat focal plane as shown in Fig. 3.16.

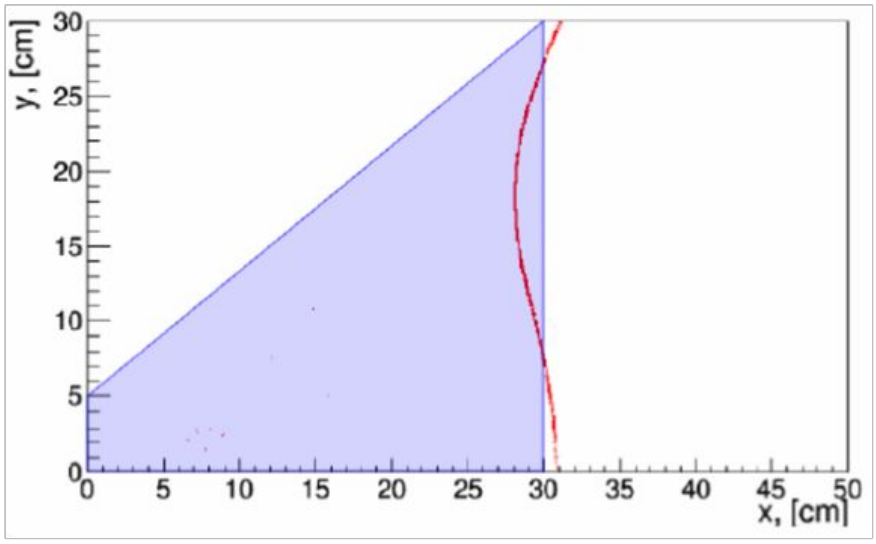

Figure 3.16. Simulated focal plane for the three-layer lens in Geant4.

To measure the shape of the focal plane, a special setup was designed and built at the ODU laser lab. The schematic of the setup is shown in Fig. 3.17 and the photo of the almost complete setup is shown in Fig. 3.18. The lens is placed on the rotation stage and rotated through two parallel laser beams. The intersection point of the two laser beams determines the focal length. The lens will be placed inside a 30x40x60 mm^3 glass container filled with mineral oil (with a refractive index very close to fused silica) to simulate the focusing behavior for the situation without the air gap. The 3-layer lens will be placed in a special 3D-printed holder, shown in Fig. 3.19. This holder makes it possible to map out the focal plane in all three dimensions, which will be particularly important for comparing spherical and cylindrical lens designs.

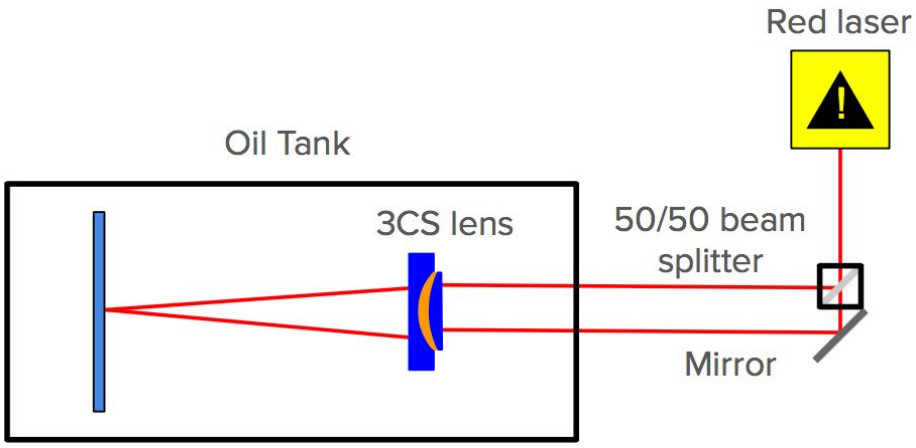

Figure 3.17. Schematic diagram of the optical setup to map the focal plane of the high-refractive lens as a function of rotation angle of the lens.

+

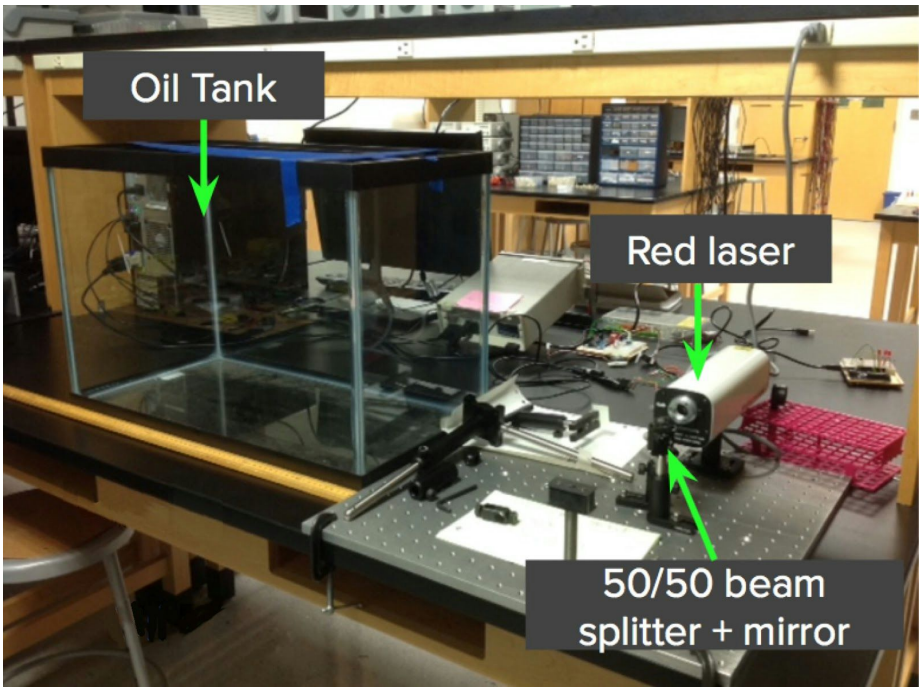

Figure 3.18. A photograph of the setup to map the lens focal plane built at ODU.

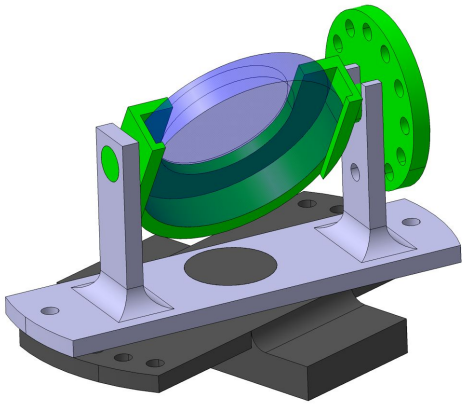

Figure 3.19. A CAT 3D image of the 3-layer lens holder designed for focal plane mapping.

3.2.3 Prism with a tilted detector plane as an expansion volume.

The study of the properties of photosensors in high magnetic fields, described in Chapter 4, is still ongoing. However, some general features are already clear, and we took them into account in the design of the DIRC expansion volume. Measurements performed in the summer of 2015 showed that, even though the gain of the sensors drops drastically in the magnetic field, it is possible to recover it to some extend by modifying the voltages applied between the MCPs and the anodes. It is clear that such a recovery works best for a configuration where the sensor is placed perpendicularly to the magnetic field lines. That is why the shape of the expansion volume and possible modifications were reinvestigated. The combination of the radii of the focusing and defocusing elements within the 3-layer lens was selected to make the focal plane follow a flat detector plane, perpendicular to the bottom of the prism. By further optimization of the radii in the Geant4 simulation, it was possible to achieve a tilted but still rather flat focal plane, as shown in Fig. 3.20. The special shape of the prism expansion volume, indicated by the drawing in the plot, would allow the optimal placement of the sensors with respect to the magnetic field lines. Note that the focal plane is placed behind the rear wall of the prism to account for longer photon paths due to reflections in the prism. The final optimization of the best tilt angle will be performed once the final magnetic field map is available for the EIC detector(s). An important additional benefit of the tiled detector plane configuration is that lens elements with larger radii can be used in the modified 3-layer lens. This makes the elements thinner and, therefore, limits the photon loss due to reflections on the sides of the lens.

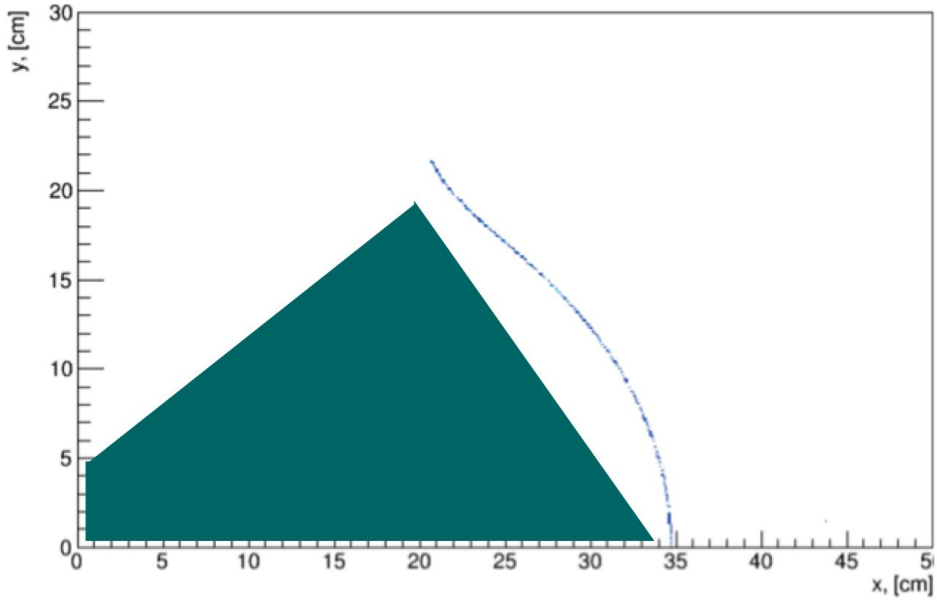

Figure 3.20. Geant4 simulation of the 3-layer lens with a tilted focal plane.

3.3 What is planned was not achieved, why not, and what will be done to correct?

The test bench measurements of the 3-layer lens , which were planned for early FY16, have not yet been completed due to time limitations and delays in obtaining some of the components for the setups. However, most of the components are already in place and both of the measurements should be completed at the beginning of 2016.

Future

3.4 What is planned for 2016 and beyond? How, if at all, is this planning different from the original plan?

At the beginning of 2016 one of the lens prototypes and samples of NLaK-33 will be tested for radiation hardness at CUA. Both irradiation and transmission measurement of the lens will be performed, under the supervision of G.Kalicy and T.Horn. The second prototype of the 3-layer lens will be used to map its focal plane. This measurement will be performed at ODU University by G.Kalicy and L.Allison.

The analysis of the data from the CERN test beam will continue throughout FY16. Careful calibration of the data has to be performed before evaluating the performance of the 3-layer lens and comparing it to other focussing options. Optimization of timing cuts and fitting parameters is likely to improve the obtained single-photon resolution. More extensive use of the beam counters in the analysis should also further improve the quality of the data sample by taking out effects such, as for example, the beam divergence. Charge sharing effect will

be included in the Geant4 simulation, and corrected for in the test beam data. Different variations of the geometric reconstruction method will also be used to determine a single-photon resolution.

Several important new features will be implemented and studied in general DIRC@EIC simulation package. It was shown that it is possible to have a tilted, but still flat focal plane by adjusting the ratio of radii in the 3-layer lens. However, in addition to optimizing the tilt for a certain local orientation of the magnetic field, the influence of a tilted detector plane on the single-photon resolution and the photon yield has to be studied more carefully. For the latter, the thinner lenses in a tilted focal-plane configuration suggest a possible intrinsic improvement. Also, while the single-photon resolution and the photon yield are key parameters for comparison with test beam data, the π/K identification efficiency and mis-ID across DIRC phase space has to be also implemented as figure-of-merit for DIRC design evaluation for all tilt angles.

Development of a time-based reconstruction algorithm for geometries with alternative wide plates without focusing and with cylindrical focusing is another very important task as this solution has a potential of large cost saving. Although this effort was proposed for FY17, preparatory work will be starting in FY16 since an important part of the validation will be based on applying it to narrow bars and spherical lenses, in simulation and test beam data, and comparing to the geometrical reconstruction method. We also plan to investigate fit to ring-center as a way to mitigate effect of insufficient tracking resolution and to study opportunities for e/π identification in the central EIC detector using a DIRC.

Also, in preparation for the proposed FY17 effort, which includes development and construction of radiation-hard lens, we have started design of such a lens in ZEMAX and Geant4. To maximize synergies with the effort to reduce costs by using wide plates instead of narrow bars (with more reliance on high-precision timing in the reconstruction) this new three-layer lens will be cylindrical. We are discussing the possibilities of building the new prototype 3-layer lenses with two manufacturers, Koth and Nikon. Korth is the only company so far that is willing to use PbF_2 as an alternative for NLak-33, as it is a very hard material to work with. Nikon is instead investigating other options for radiation hard materials with high refractive index that they could use for the middle layer. They will also evaluate the price of a potential prototype of the prism expansion volume with a tilted plane.

In general, the work is proceeding as planned. The only difference is that we are whenever possible trying to fold in preparatory steps for the work proposed for FY17.

3.5 What are critical issues?

The R&D is currently proceeding according to plan and we do not foresee high-risk elements in the near future.

3.7 Manpower

G. Kalicy (ODU) - postdoc funded at the 50% level by eRD14
L. Allison (ODU) - grad student (DIRC work part of thesis)
C. Hyde (ODU) - prof.
T. Horn (CUA) - prof.
R. Dzhygadlo (GSI) - postdoc
J. Schwiening and C. Schwarz - GSI staff
P. Nadel-Turonski and Carl Zorn - JLab staff

In addition, Y. Ilieva (prof. USC), T. Cao (grad student USC), and K. Park (postdoc ODU/JLab), who are primarily involved in the high-B program also participate in the DIRC effort.

3.8 External Funding

Some external funding has been provided for travel from JLab (operations funds) and ODU (travel for G.Kalicy and L.Allison to Germany to work together with GSI group on CERN data analysis and to participate in the DIRC 2015 workshop). ODU also provides matching funds for the postdoc, and an ODU-funded grad student for test beam analysis. GSI also provides part of a postdoc for simulations. The main support comes, however, through synergies with GSI (PANDA) and JLab (GlueX) DIRC R&D.

We have been able to benefit from very significant synergies with the PANDA DIRC development. It allowed us to develop the lens-based high-performance DIRC concept and to validate the performance of the optics in test beams at CERN and GSI. In terms of hardware contributions, the PANDA group essentially made available an entire prototype setup, including several radiator bars (and plates) of fused silica with the required optical quality ($30-60k each), two fused-silica expansion volumes ($20k each), electronics, and mechanical infrastructure, as well as transportation for the latter to the test beams. This has allowed the EIC DIRC R&D to purchase only a few key components – most importantly the prototype of the advanced spherical three-layer lens – in order to carry out the prototyping, and to only provide travel for the ODU postdoc and student to the test beams at CERN.

The synergies with the GlueX DIRC effort will play the significant role in case of studying different expansion volume option.

Publications

[1] G. Kalicy *et al.*, *DIRC detector for the future Electron Ion Collider experiment*, Proceedings of the DIRC2015 Workshop, 11 - 13 November, Rauischholzhausen, Germany, to be published in Journal of Instrumentation (JINST).

4. Sensors in high magnetic fields

Contact: Y. Ilieva <jordanka@jlab.org>

4.1 MCP-PMT sensors in high magnetic fields

Abstract
The program for testing photosensors in high magnetic fields was established within eRD4, and has now been taking data for a second year. After the first measurements, taken in Summer and Fall 2014, demonstrated that MCP-PMTs with small pore sizes can perform well in magnetic fields up to several Tesla, but that the gain deteriorates (sometimes very rapidly) as a function of the angle between the MCP normal direction and the direction of the magnetic field, we have turned our focus on studies of design optimization. The goal of these studies is to establish an optimal set of MCP-PMT operational and design parameters, and their limits, for operating the sensors in a range of field magnitudes and orientations similar to what is expected for DIRC and RICH applications in an EIC detector.

Past

4.1.1 What was planned

The plans for the past 6 months were to continue to evaluate the gain performance of MCP-PMTs in magnetic fields up to 5 T. More specifically, we intended to focus on studying the sensors tested in Summer and Fall 2014 as a function of the high voltages between the photocathode and the MCP ($V_{C\text{-}MCP}$), across the two multichannel plates ($V_{MCP\text{-}MCP}$), and between the last MCP and the anode ($V_{MCP\text{-}A}$).

4.1.2 What was achieved?

Our achievements are two-fold; we have implemented upgrades in the setup and we have obtained new gain data. The main upgrades were implemented in order to achieve a better control of the stability of the light intensity on the sensor's photocathode. The purpose is to decrease the uncertainty of the control variable we use for gain evaluation. We have also implemented additional monitoring to decrease the risk of photocathode damage. We have obtained results for the gain dependence on the internal MCP-PMT high voltages. All of these are reported below.

4.1.2.1 Facility Upgrades

In the summer of 2015 the following upgrades were implemented in the facility

- The pulser controlling the light-emitting diode was calibrated against a reference PMT with known quantum efficiency.

- A set of neutral density filters was calibrated with the goal of controlling the light intensity on the photocathode by means of filters while keeping the voltage of the LED-driving pulser constant at a high value.
- A SiPM was implemented and used as an independent light monitor. The light from the LED was split between the MCP-PMT being tested and the SiPM by means of a bifurcated cable. The SiPM was operated continuously outside of the magnetic field.
- The anode current of the tested MCP-PMT was monitored by redirecting the signal output to a picoammeter. The current was measured prior to each run to ensure that the charge through the device is within acceptable limits and decrease the risk for damages.
- By measuring the current through the voltage divider (shown in Fig. 4.1.1), we evaluated the MCP-PMT resistance and monitored this quantity on a run-per-run basis throughout the experiment.

4.1.2.2 Measurements and Results

Through a negotiated loan with Photek, the 3-μm single-anode sensor PMT210, which we measured in 2014, was made available for our Summer 2015 measurements. In order to allow for independent regulation of the voltages within the sensor, a special voltage divider was designed and manufactured at JLab (see Fig. 4.1.1). The voltages were adjusted by choosing various combinations of resistors.

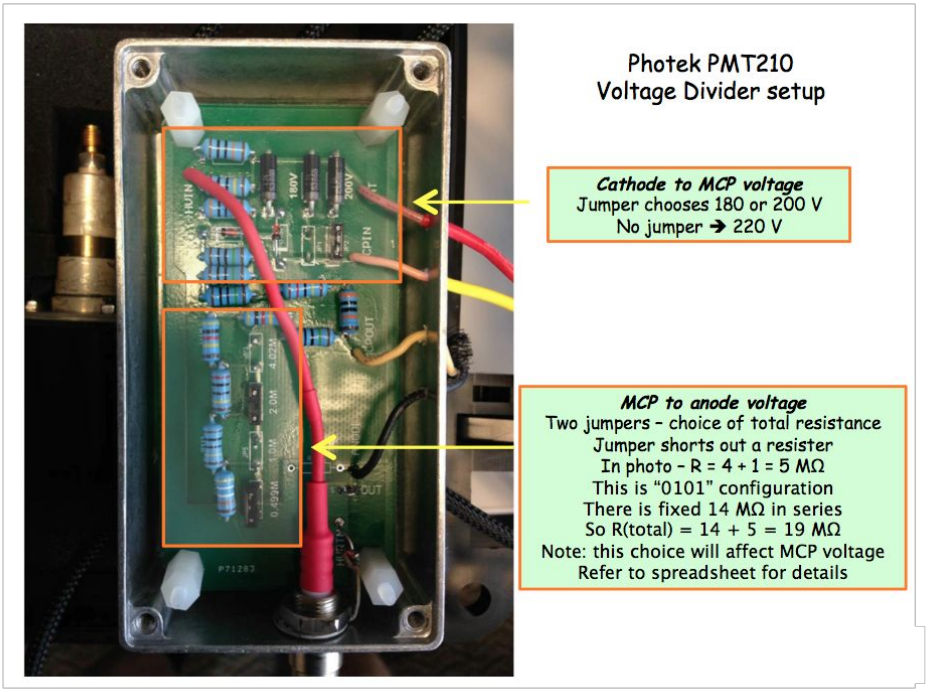

Figure 4.1.1. Photograph of the custom built voltage divider that was used to evaluate the gain of Photek PMT210 for various, independently controlled voltages $V_{C\text{-}MCP}$, $V_{MCP\text{-}MCP}$, $V_{MCP\text{-}A}$. Two values of $V_{C\text{-}MCP}$ were used: the nominal value of 200 V and 220 V. $V_{MCP\text{-}MCP}$ was varied in the range between 90% and 99% of the maximum value of 2750 V. $V_{MCP\text{-}A}$ values were the nominal values of 1736 V and 1868 V and values higher by 100 V than the nominal values.

The purpose of the measurements was to establish the extent to which the gain at high fields and non-zero angles between the field and the sensor axes can be recuperated by increasing the high voltages within the sensor. As the voltage across the two micro-channel

plates, $V_{MCP\text{-}MCP}$, was expected to be the most critical one, we focused mainly on gain evaluation over a broad range of $V_{MCP\text{-}MCP}$. Our results are shown in Figures 4.1.2 and 4.1.3.

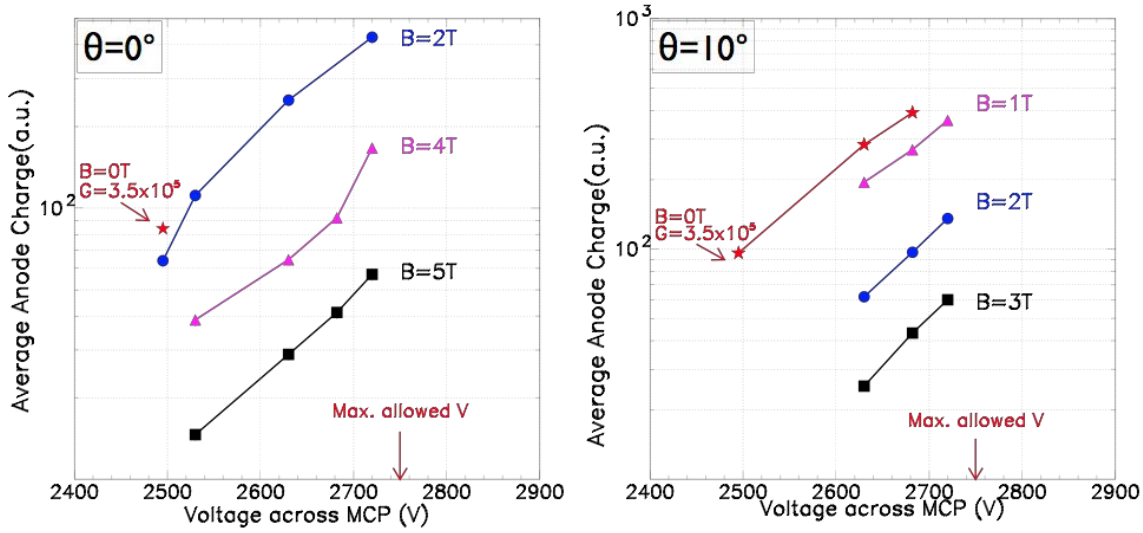

Figure 4.1.2. Average anode charge per pulse as a function of $V_{MCP\text{-}MCP}$ for several values of the magnetic field B and two angles θ between the MCP-PMT and the B-field axes, 0º and 10º. The average anode charge is proportional to the gain of the sensor and is our control quantity for gain evaluation. As $V_{MCP\text{-}MCP}$ increases, the gain increases exponentially, which allows the gain of 3.5×10^5 at 0 T to be recoverable up to 5 T at θ=0º and up to 3 T at θ=10º.

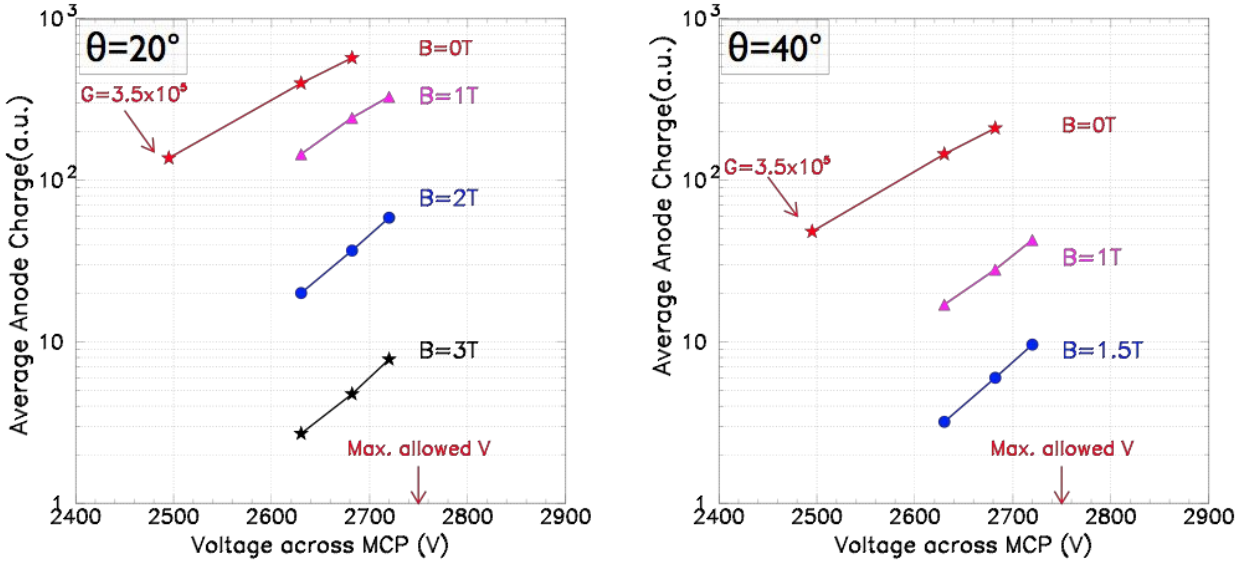

Figure 4.1.3. Average anode charge per pulse as a function of $V_{MCP\text{-}MCP}$ for several values of the magnetic field B and two angles θ between the MCP-PMT and the B-field axes, 20º and 40º. By increasing $V_{MCP\text{-}MCP}$ to 99% of the maximum allowed value, the gain of 3.5×10^5 at 0 T was recoverable to < 2 T at θ=20º and to < 1 T at θ=40º.

Our results suggest that at θ = 0º, a gain of 3.5×10^5 can be recovered up to field magnitudes of 5 T by increasing $V_{MCP\text{-}MCP}$. As the polar angle increases, the field at which gain recovery is possible, decreases. At θ = 10º, the gain can be recovered for fields below 3 T. At θ = 20º, the gain can be recovered for fields below 2 T. At θ = 40º, the gain can be recovered for fields below 1 T.

In addition, we tested the PMT210 gain performance for 20-V variations of the voltage between the cathode and the first MCP, and for 100-V variations of the voltage between the last MCP and the anode. Neither of these variations yielded a noticeable change in the sensor's gain.

It is clear from our measurements that optimizing the voltage across the multi-channel plates can help for gain recovery in B-fields. The extent of the recovery, however, strongly depends on the angle between the sensor and the field axes. To achieve full gain recovery at θ angles different than 0º, other sensor parameters need to be also optimized. One of the most efficient ways to proceed with that is to input the MCP-PMT geometry in a simulation, such as GEANT4, and then proceed to simulate the electron avalanche evolution in various magnetic fields. The total anode charge can be then studied for various ratios of the pore-size diameter to channel length, bias angles, and distances cathode to first plate and last plate to anode.

4.1.3 What is planned was not achieved, why not, and what will be done to correct?

All that was planned was achieved.

Future

4.1.4 What is planned for 2016 and beyond? How, if at all, is this planning different from the original plan?

The planned future of the program aims to achieve an MCP-PMT design and operational parameters that are optimized for successful application in DIRC in the high magnetic field of the central detector at EIC. This is a significant effort, which involves (a) High-B gain measurements of a variety of commercially available single- and multi-anode MCP-PMTs as a function of various operational parameters (b) Development and implementation of a GEANT4 simulation of an MCP-PMT in the design process, (c) Timing studies in high magnetic fields of various commercially available single- and multi-anode MCP_PMTs. The future of the program is based on our results from the first two program years and will require increase in personnel to accomplish the program's goal stipulated above.

More specifically, our main activities will involve:

- Design and manufacturing of a universal HV divider with independent control of the internal voltages in the photon sensor, which can be used with a broad range of MCP PMTs.
- Gain evaluation of several 10-μm **multi-anode** sensors that are available on loan (Hamamatsu, Photonis).
- Implementation and commissioning of timing capabilities in the High-B facility.
- Studies of timing resolution of single- and multi-anode sensors in fields up to 5 T.
- Timing and gain tests of Katod single-anode sensors: single-anode 3-μm and 5-μm pore size.
- Development of a GEANT4 simulation of an MCP-PMT in magnetic field and studies of its gain performance for varying geometrical parameters. The goal is to support the design optimization of MCP-PMTs for their operation in magnetic fields such as expected for DIRC at EIC.
- Studies of the effect of high B-fields on the ion feedback in an MCP-PMT, both with simulated and real sensors.

As our effort grows, we will continue to benefit from the expertise of our PANDA GSI collaborators and from the established collaborations with MCP-PMT manufacturers, such as Photek and Photonis (we will invest an effort to start a similar collaboration with Hamamatsu as we proceed with the evaluation of their sensors).

4.1.5 What are critical issues?

The critical issues for the success of the program are (a) the availability of various MCP-PMT samples for studies and optimization of operational parameters and (b) adequate personnel and operational funding to support the expanding effort.

(a) With the help of our GSI collaborators we have established productive relationships with MCP-PMT manufacturers, such as Photek and Photonis, who are interested in our program and have provided sample sensors for our measurements. We will continue this collaborative work for the optimization of the geometrical and operational MCP-PMT parameters for operations in high magnetic fields and will invest efforts to negotiate sample sensors for our future measurements. Hamamatsu and Photonis have already provided us free of charge with 10-μm pore-size multi-anode sensors for tests in 2016. We have also established a contact with CAEN who is developing fast electronics, such as discriminators, which opens the opportunity to obtain sample modules for our tests.

(b) As the program matures, the size of the effort naturally increases and requires both more personnel and more measurement time. The funding under this R&D is critical to support summer student internships, travel between JLab and USC, operations (cost of LHe to operate the superconducting magnet) and hardware (such as custom components and items for the timing measurements).

(c) With two measurement periods planned each in 2016 and the years beyond (one run in summer and one run in fall), prompt availability of approved funds at the beginning of the fiscal year is critical for the success of the fall measurements.

4.1.6 Additional Information

None.

Manpower

University Faculty: Y. Ilieva (USC); R&D funds paid for Y. Ilieva's travel to and stay at JLab for high-B test runs.

JLab staff: C. Zorn, P. Nadel-Turonski.

Postdoctoral fellows: K. Park (ODU), G. Kalicy (ODU); 50% salary for G. Kalicy is funded by R&D funds.

Graduate students: L. Allison (ODU, supervised by G. Kalicy and Ch. Hyde), T. Cao (USC, supervised by Y. Ilieva). R&D funds paid for T. Cao's travel to and stay at JLab. T. Cao spent 2 weeks (4% of his time) on the High-B sensor tests. L. Allison spent 2 weeks (4% of his time) on the High-B sensor tests.

Undergraduate students: C. Barber (USC, supervised by Y. Ilieva and C. Zorn), travel and 8-week internship at JLab paid by R&D funds. C. Barber spent 100% of her internship working on the High-B facility and sensor tests.

External Funding

Jefferson Lab contributed significantly by providing infrastructure (in the test lab) hardware (a 5T superconducting solenoid), some of the funds for operations of the test facility, and by providing personnel for the cryogenic operation of the magnet and for data acquisition installation and maintenance. USC and ODU have contributed travel funds for their respective personnel.

Publications

[1] Y. Ilieva *et al.*, *MCP-PMT studies at the High-B test facility at Jefferson Lab*, Proceedings of the DIRC2015 Workshop, 11 - 13 November, Rauischholzhausen, Germany; to be published in Journal of Instrumentation (JINST).

4.2 LAPPD sensors in high magnetic fields

PROGRESS REPORT OF eRD14 - THE PID CONSORTIUM
LAPPD / MCP PROJECT

October 1 – December 31, 2015

M. Demarteau, J. Wang, R. Wagner, J. Xie
Argonne National Lab, Argonne, IL 60439

M. Chiu (co-PI), T. Tsang
Brookhaven National Lab, Riverhead, NY 11901

F. Barbosa, J. McKisson, P. Rossi,
W. Xi, B. Zihlmann, C. Zorn (co-PI)
Jefferson Lab, Newport News, VA 23606

M. Grosse-Perdekamp
University of Illinois at Urbana-Champaign, Urbana, IL 61801

W. Brooks, R. Mendez
Universidad Tecnica Federico Santa Maria, Valparaiso, Chile

J. Harris, R. Majka, N. Smirnov
Yale University, Urbana, New Haven, CT 06511

Abstract
An initial test of the behavior of the 6x6 cm^2 LAPPD sample (#28) within a high magnetic field has been performed. This study focused on the changes in the gain of the device. The high magnetic field was provided by a large-bore (60 cm diameter) MRI research magnet at the Biomedical Engineering Department of the University of Virginia. The field is purely solenoidal within the bore at a fixed field of 3 Tesla. To vary the field, the sample was moved outside the bore along the longitudinal axis of the magnet. Unfortunately, this method also produced a mixture of the axial and transverse fields on the sample. The results verify that this prototype sample has design aspects which prevent it from achieving a good tolerance to high magnetic fields. The basic problem is that the elements of the LAPPD have internal spacings large enough to be strongly affected by transverse magnetic fields. The report covers the progress during six months of the project from October 1, 2015 to December 31, 2015.

4.2.1 What was planned?

In the previous report [1], the next step in the characterization of the LAPPD was the testing of its gain and timing characteristics in a high magnetic field. Since the laser pulser could not be used in a mobile setup, it was decided to focus on the gain characteristics instead.

4.2.2 What was achieved?

To characterize the sample in a high magnetic field, a mobile test setup was created and is shown in Figure 4.2.1. The LAPPD sample is placed inside a light tight box made only of either non-magnetic parts or parts with a very weak sensitivity to a strong magnetic field. The light source is a fast pulsed UV or blue LED. Wavelength choices include 370, 405, or 470 nm. It was found that the 370 nm emission gave an equivalent amplitude response to the others while giving the best time response from the LAPPD in terms of rise time and pulse width. Since the LED leads are very sensitive to a magnetic field, the light is delivered to the light tight box via a 5 meter long UV grade silica fiber. On the inside surface of the box where the light enters the interior of the box, a diffuser was installed to ensure uniform illumination of the LAPPD. It is also important to note an interesting fact about the LAPPD device. Unlike any of the commercial MCP-PMTs that were available to our lab, this was the only one that showed no attraction to a strong ambient magnetic field. This aspect may influence its behavior and would certainly be useful in the design of fixtures for clamping it in place within a large detector setup.

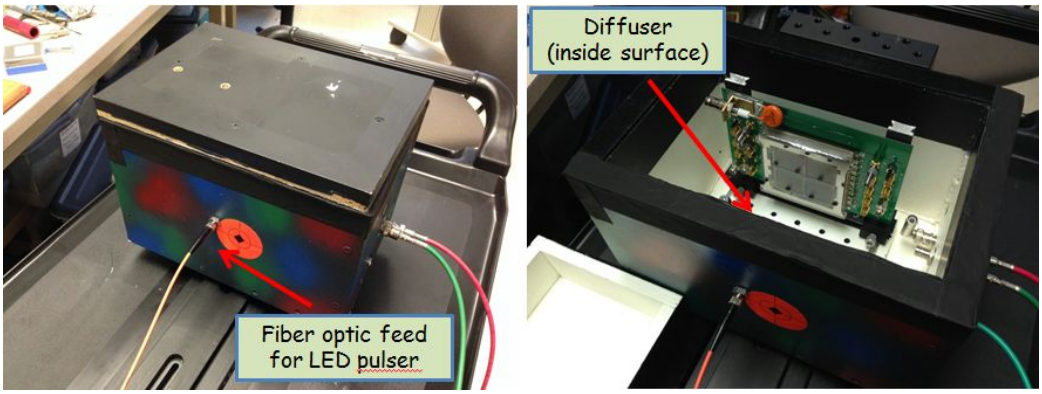

Figure 4.2.1. Photograph of small dark box setup for testing LAPPD sample in a high B field. The light source is a 370 nm pulsed LED connected via a 5 meter fiber optic to the dark box. A diffuser on the inside surface (not seen in photo) spreads the light from the fiber optic in a uniform illumination of the LAPPD faceplate. The box can mounted on an optical rail to allow controlled insertion into a magnetic field.

In the prior report [1], it was shown that one had to mask out adjacent readout channels in order to obtain a good single photoelectron (SPE) spectrum from an illuminated channel. By using this method a gain map of the device was made and is shown in Figure 4.2.2. The SPE could only be resolved at relatively high voltages and gains, even with the use of a good external amplifier. For the test, it was decided to collect data on two of the channels – one in the upper half (ch.3) and the other in the lower half (ch.6) of the MCP-PMT.

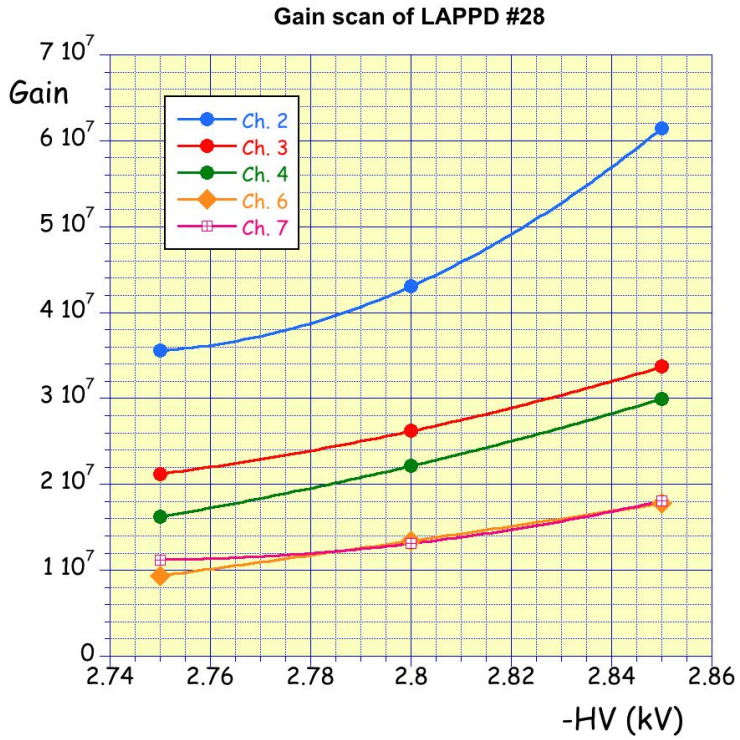

Figure 4.2.2. Gain scan of the live channels of the LAPPD using SPE spectra to determine the gain. Channels 1,5, and 9 are not shown as the glass frame within the LAPPD structure blocks the amplification process. Channel 8 had a very weak signal. Channels 3 and 6 were chosen for the magnetic field test – one from the upper half and the other from the lower half of the LAPPD. The HV was fixed at -2.8 kV during the test.

Figure 4.2.3 is a photograph of the setup within the MRI magnet room at UVA. Figure 4.2.4 shows a schematic of the test setup. A 3-axis teslameter gives a reading of the magnetic field near the LAPPD. A separate run was made to collect the actual readings at the center of the LAPPD faceplate. The tests were run at a fixed gain for both channels. Both the absolute gain and relative gains were monitored. The latter were useful when the absolute value was too difficult to determine from the SPE spectra. The relative gain was determined by boosting the light intensity to about 10 photoelectrons and monitoring the pulse height. The sample box was mounted on a platform that could be moved along the longitudinal axis of the magnet in a controlled fashion with increments as small as 1 millimeter. The magnetic field values were the result of the outside fringe field of the MRI magnet as the central solenoidal field within the bore of the magnet was fixed (and could not be varied) at 3 Tesla.

Given that the fringe field would result in both transverse and axial components, it was necessary to determine the position of the LAPPD within the field. Figure 4.2.5 is a schematic showing the LAPPD relative to the symmetry axes of the magnet. Figure 4.2.6 shows the vectors representing the orientation of the transverse field. Some of the implications of this are shown in Figure 4.2.7. The left plot shows that the B field magnitude differs only slightly between the LAPPD center and the teslameter position (at the top of the box), but the transverse field differs considerably as shown in the right plot. If one compares this to the situation where one rotates a PMT within a purely axial field, then this is equivalent to a 11° rotation. Figure 4.2.8 shows the magnitudes of the axial and transverse components as a function of the positions used in the test run.

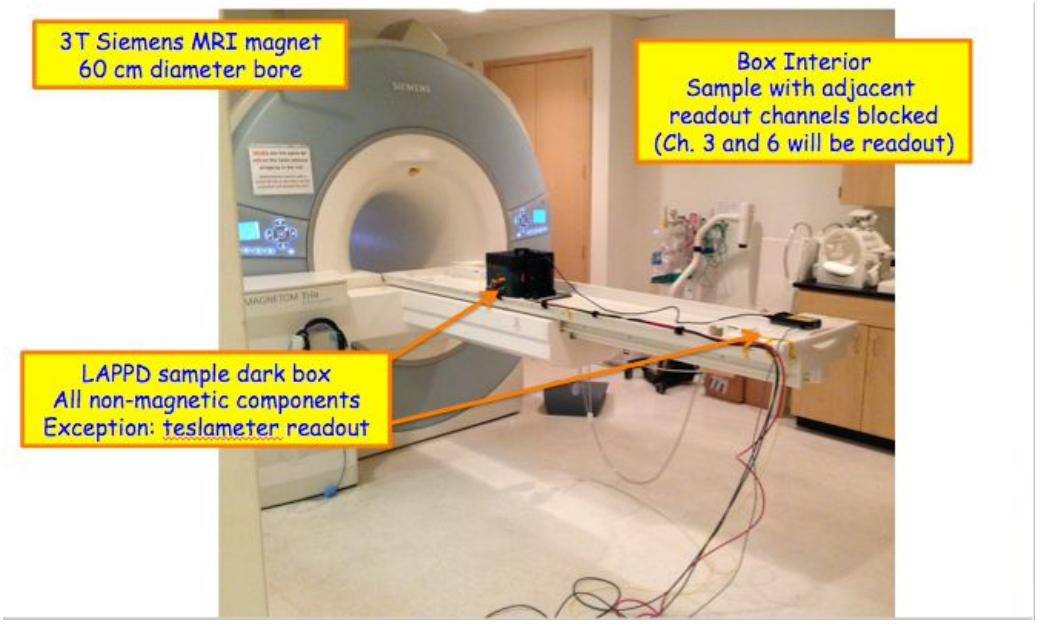

Figure 4.2.3. A photograph of the setup at the UVA MRI research facility (Dept. of Biomedical Engineering). The sample box was placed on platform that could be moved in small controlled steps (millimeters). The magnetic field strength was measured by a 3-axis teslameter [2]. All DAQ hardware and the PC laptop were placed outside the room as required for safe operation. Other than the teslameter readout box, all materials inside the room were non-magnetic.

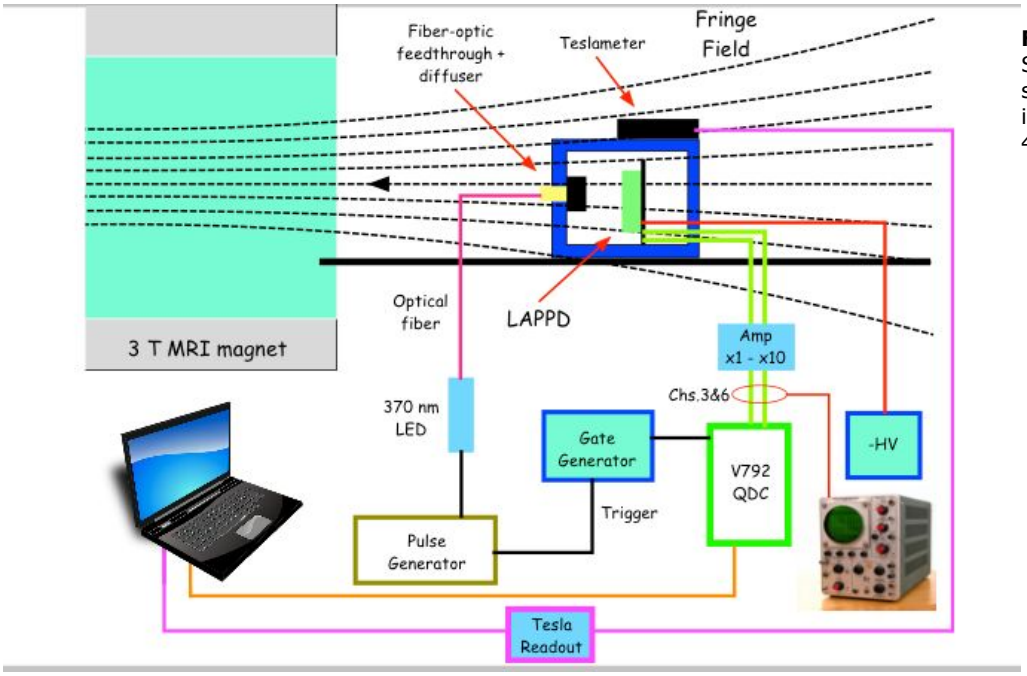

Figure 4.2.4. Schematic of the setup partially shown in the photo of Fig. 4.2.3.

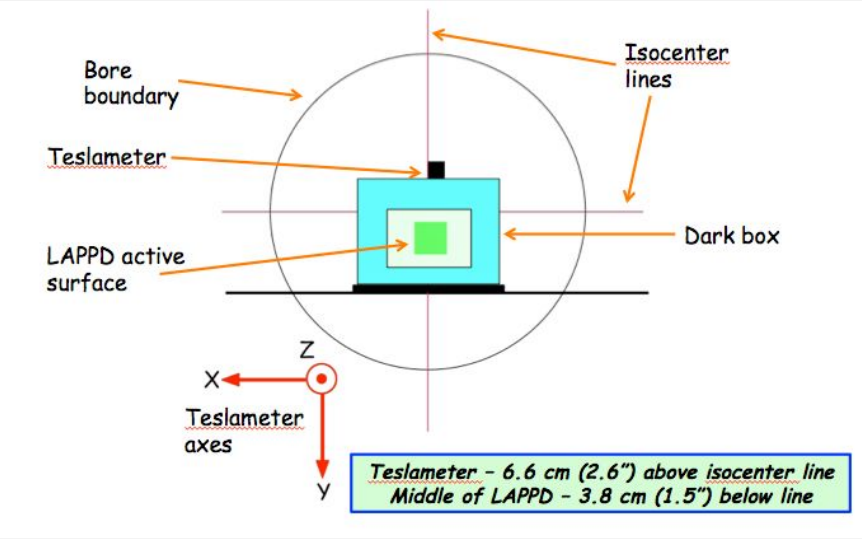

Figure 4.2.5. Schematic showing the position of the LAPPD relative to the symmetry axis of the MRI magnet.

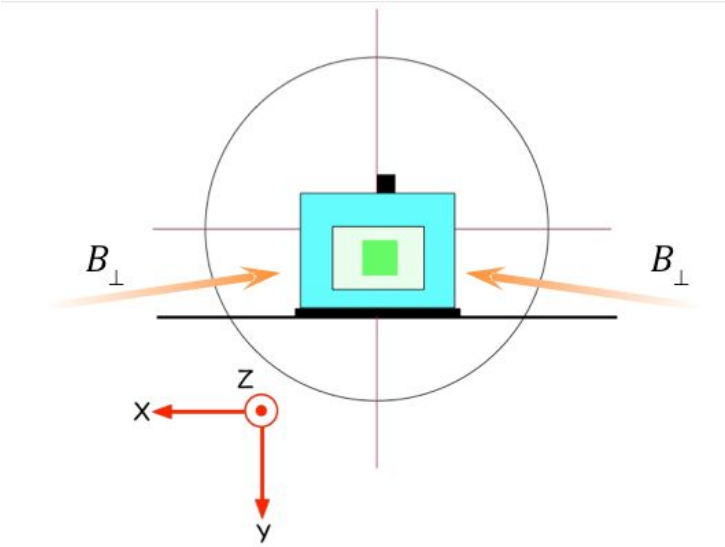

Figure 4.2.6. As on Fig. 4.2.5, but here we show the orientations of the transverse field vectors.

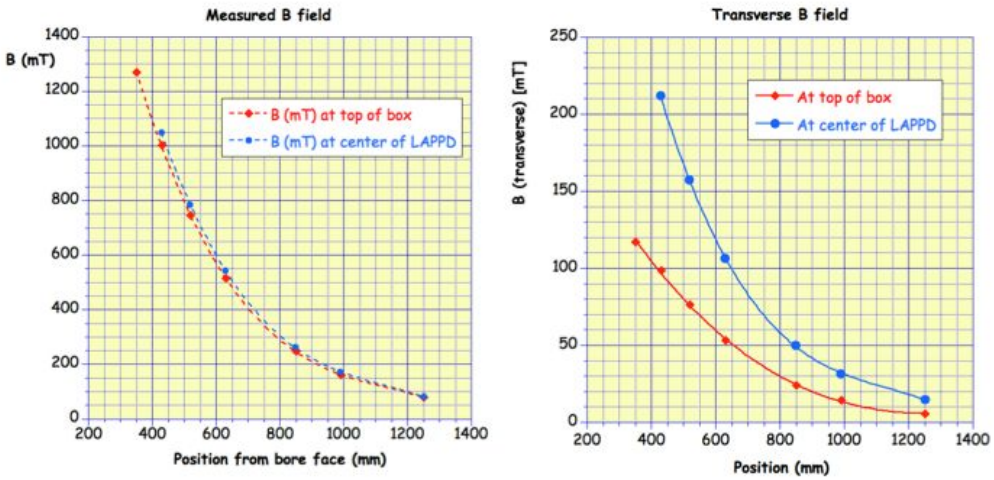

Figure 4.2.7. The B-field data collected shows that the transverse field differs significantly between the teslameter position during the tests and the actual values at the center of the LAPPD faceplate (RH plot). In contrast, the total B field magnitude differs only slightly (LH plot).

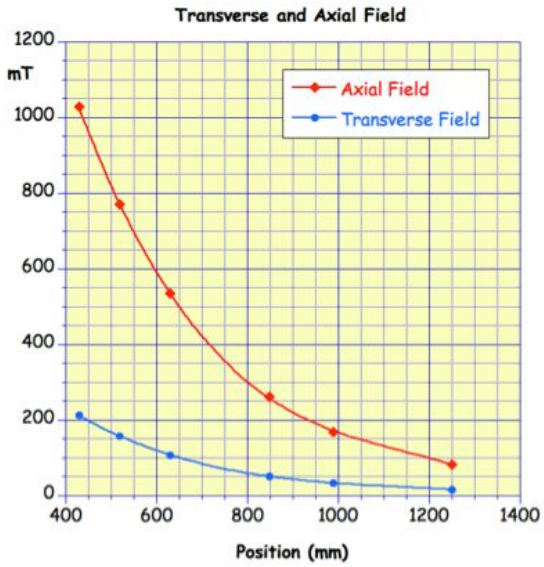

Figure 4.2.8. Magnitudes of the actual axial and transverse components of the B field as function of the position of the sample relative to the entrance face of the magnet bore.

Figures 4.2.9, 4.2.10, and 4.2.11 show the key results of the test run. Figure 9 displays the loss in absolute gain for both of the monitored channels as a function of the transverse field, and indicates a factor of *x*5 to *x*6 loss in gain by 100 mT. (At this value, the B field has a magnitude of about 0.5 T). To monitor the gain loss over a wider range, the relative gain was used by measuring the pulse height for a higher light intensity (~10 pe). Figure 10 shows these results indicating a total loss in signal by 250 mT transverse. (The B field is about 1 T at this point.) Note that, unlike the absolute gains, the pulse heights for the two channels are almost equal. This is an example of how the quantum efficiency of the faceplate varies as well as the gain over the LAPPD. Several runs were also taken at various

rotation angles (in the plane of the platform). Figure 4.2.11 indicates the overall result that the transverse field is the appropriate parameter rather than the axial or total field values.

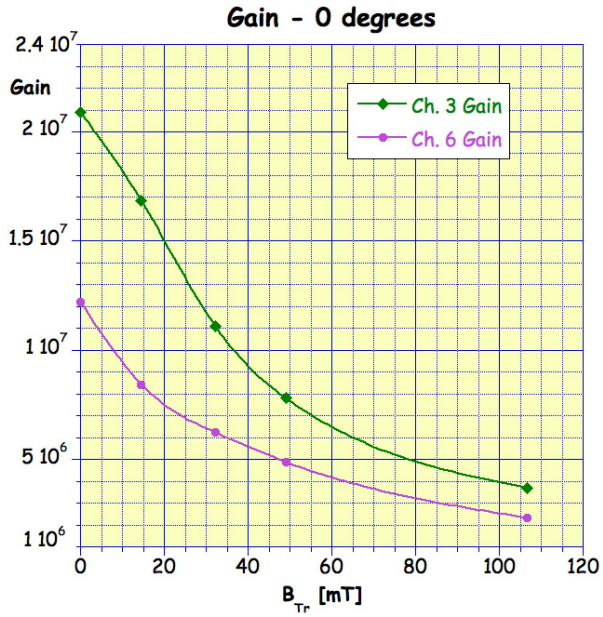

Figure 4.2.9. The loss in absolute gain as a function of the transverse field for the two monitored channels.

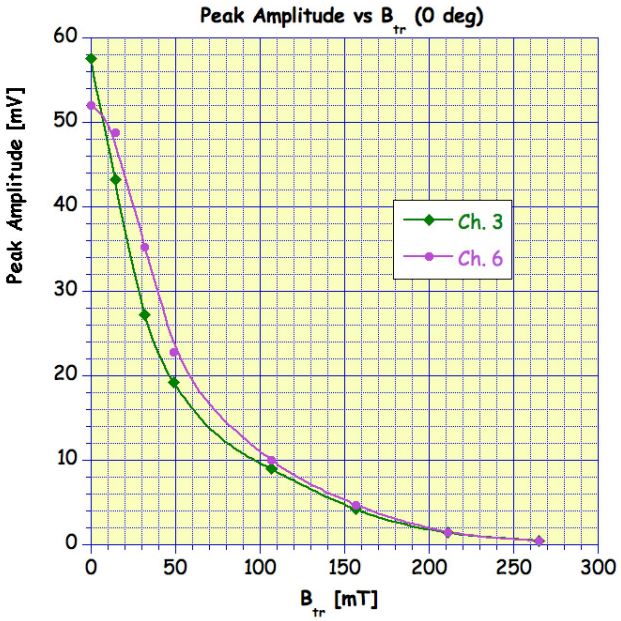

Figure 4.2.10. The loss in relative gain for the two channels as function of the transverse field.

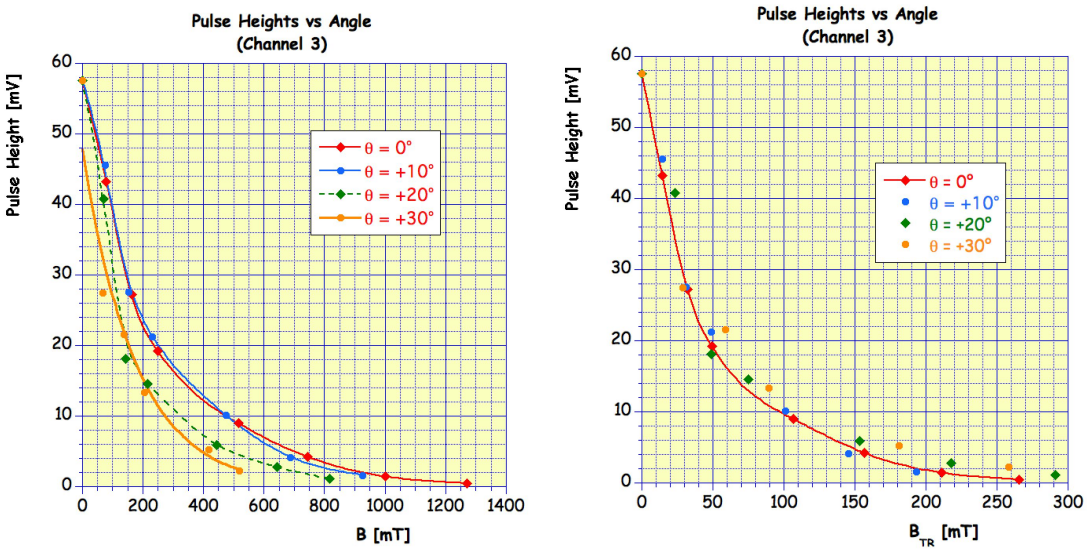

Figure 4.2.11. Pulse heights (relative gain) as a function of the B field (LH) and the transverse field (RH) for a variety of rotations on the platform plane. The data indicates that the transverse field is the correct parameter to use in analyzing the gain changes.

To compare this to a current commercial device, one can look at the example of the PANDA collaboration results for the Photonis XP85012 [3] as shown in Figure 4.2.12.

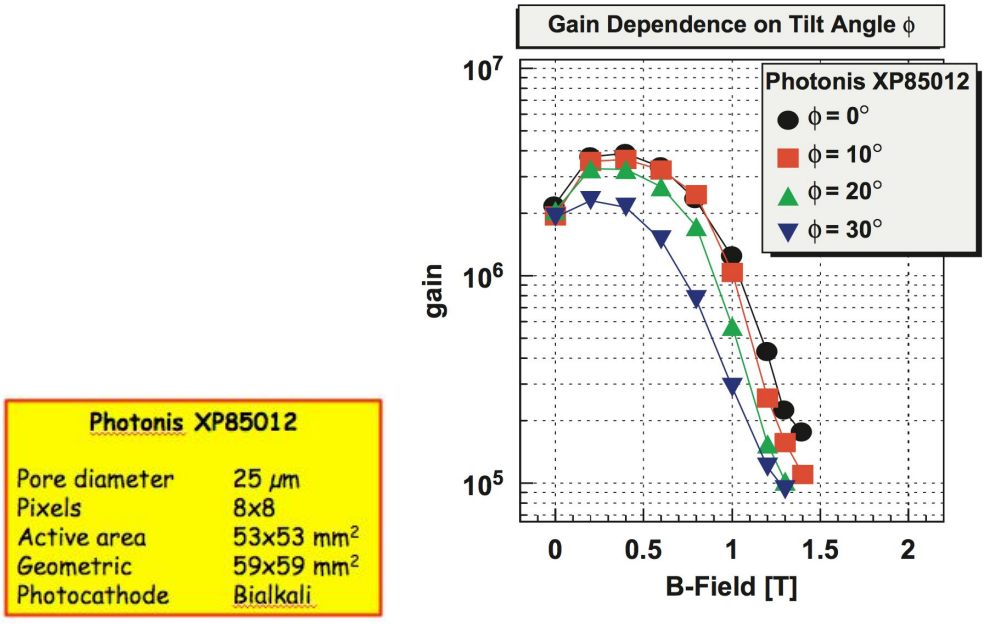

Figure 4.2.12. From reference [3], a plot showing the gain changes in the Photonis XP85012, a commercial MCP-PMT, which is comparable to the LAPPD. The results show that the commercial device has far greater tolerance to a high magnetic field compared to the current LAPPD sample. Examination of the structure of the prototype LAPPD reveals why this follows.

Notice that the data at 0° and 10° are almost identical showing the small effect of the transverse field on the device. Recall that in the test of the LAPPD, the transverse field was comparable to a 11° rotation in a purely axial field. At a B field value of about 0.5 T, the LAPPD suffered a loss of about *x*5-*x*6, with a total loss in signal by B ~ 1 T.

Figure 4.2.13 shows why the current LAPPD design cannot be used to create a high field tolerant device. By the necessities of the design, several gaps of 2 mm or more have to created between the stages of the LAPPD. Commercial devices try to minimize these gap distances as much as possible taking into account other deleterious effects from too small a gap. One way of testing this will be present in the new version of the device, where the voltage divider distribution will be variable and be accessible to the user. A further step can be taken by creating a more compact stack design with distances between components minimized where possible.

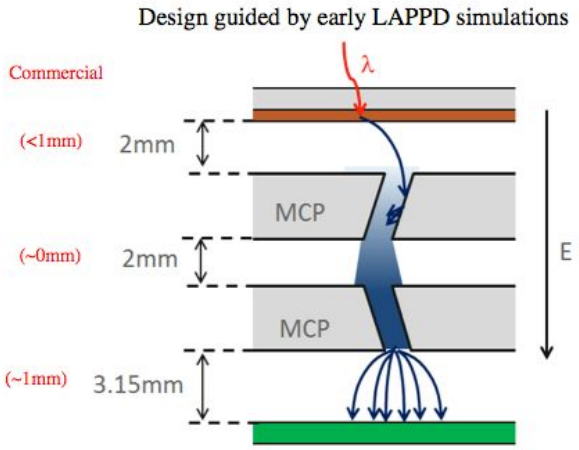

Figure 4.2.13. Basic setup of the LAPPD stack. Note that the gap distances are significantly larger than those in a typical commercial device (shown in red type at the left side). This will create opportunity for a transverse field to upset the gain amplification process in the LAPPD stack.

4.2.3 What is planned was not achieved, why not, and what will be done to correct?

The timing resolution in a high magnetic field was not tested. The timing tests performed at Argonne [8,9] showed the importance of a very fast light source such as pulsed laser. It was not possible to obtain such a device that would meet the JLAB safety requirements and be allowed for use in a mobile setup. Work is continuing on an alternative very fast LED pulser that is already being used in the GlueX experiment at JLAB [10].

Future

4.2.4 What is planned for 2016 and beyond? How, if at all, is this planning different from the original plan?

At present, JLAB is awaiting the next version of the LAPPD for further testing. In the meantime, some other tests of the current sample can be made. First, some initial rate tests have been performed. In this setup, two independently pulsed LEDS are used. One is used as the SIGNAL, and runs a low rate (1 kHz) with an intensity low enough to produce a good single photoelectron spectrum. (The mean photoelectron count is < 0.2.) The other is considered the LOAD and can have its frequency varied over several decades. At the same time, its intensity is set to produce definite single photoelectrons at the phototube, so the mean photoelectron count is about 0.5. Figure 4.2.14 displays an initial test of one of the LAPPD readout channels (ch. 3) over a range of gains. The gains below 10^6 had to estimated by monitoring pulse heights at a higher light intensity (but within the linear range of response). Further tests are planned which include verifying these results with a commercial MCP-PMT.

Another project is to redo the original pulsed laser setup so that the cross channel contamination of readout channels can be avoided. This will be important for timing studies of the LAPPD.

The final test will involve irradiating the LAPPD to a high neutron and/or gamma dose. There is also the question of whether thermal neutrons must be considered as boron, a common element in glasses, has a high cross section for thermal neutrons, and so constitute another source of damaging radiation. At the very least, they can be a source of spurious signals [4]. References such as [5] have shown the effect of different radiation sources upon standard photomultipliers and can serve as a guide to a proper test setup.

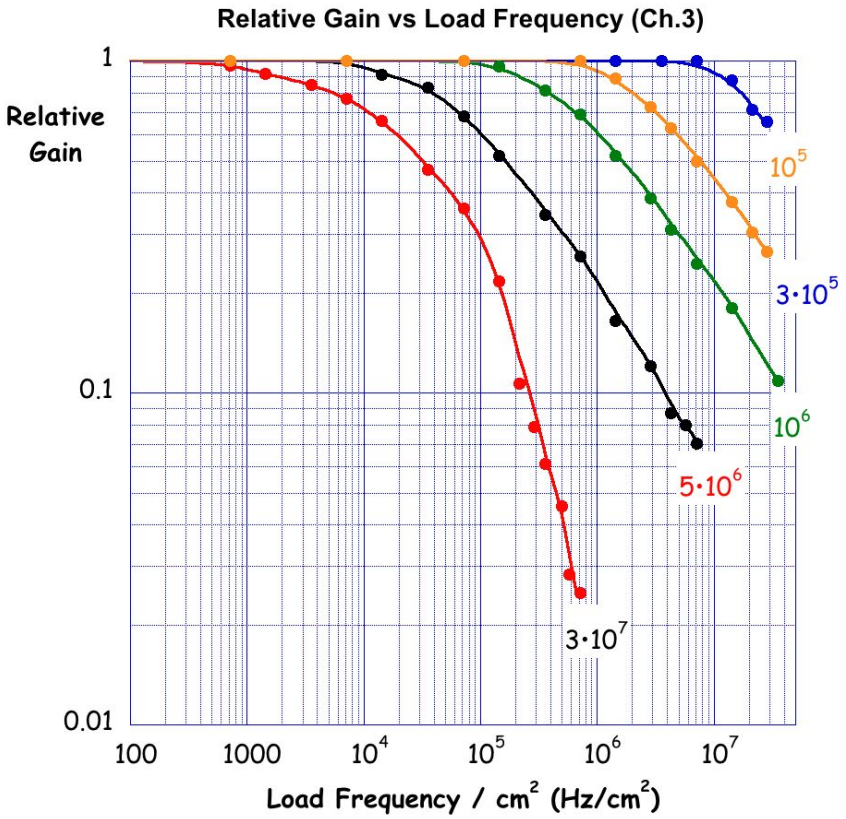

Figure 4.2.14. Results of an initial rate test of the LAPPD sample for one readout channel. The rates are normalized to 1 cm^2. The pulsed load was tuned to produce a mean count of 0.5 photoelectrons per pulse.

4.2.5 What are critical issues?

For the LAPPD, the critical issues include (i) a high quality photocathode with good uniformity and reasonable quantum efficiency, (ii) a new pad-based readout for position sensitive applications, and (iii) a voltage division system that ensures good SPE response, and may allow for some increase in tolerance to high magnetic fields. The last point can also be expanded to include a more compact internal design with minimal spacings between components to create a greater tolerance to high external magnetic fields. As an added note, the pad based readout could allow for a more compact form factor for the LAPPD. This would allow it to be characterized in the present High-B test station at Jefferson Lab (originally created for the eRD4 project). This facility can produce a variable (purely) solenoidal field of up to 5 Tesla, but requires the sample to fit within a 5 inch diameter bore. This is presently impossible with the current LAPPD form factor.

Manpower

In the period covered by this report, the main efforts were centered at Jefferson Lab with C. Zorn supervising the effort and assistance provided by members of the Radiation Detection and Imaging Group whenever possible or necessary. Student help was provided during the summer period but this was funded independently as part of the Science Undergraduate Laboratory Internship program (SULI) at Jefferson Lab.

External Funding

The only external funding was provided through the previously mentioned SULI program which is an opportunity for an undergraduate student to obtain laboratory experience during the summer months. Otherwise, all funding was provided through the EIC research funds originally awarded for this effort in the latter part of 2014 for the eRD11 program carried out in 2015.

Publications

To date, no publications from this specific effort have been submitted to conferences, workshops or refereed journals. All reports have been generated as part of the internal report program of eRD11, eRD14, and the overall EIC R&D effort. The idea is to have a new generation of LAPPD samples to test before proceeding with any external publications. The original LAPPD Collaboration has published a number of publications. A relevant sampling of these is given in the References below [6-9]. Reference [9] is the one directly relevant to this report.

Acknowledgements

Acknowledgements must be made to Professors Wilson Miller and Mark Williams of the University of Virginia Biomedical Engineering Department. Their assistance was critical to the success of the B-field testing of the LAPPD.

References

[1]https://wiki.bnl.gov/conferences/images/5/51/ERD11_ProgressReport_LAPPD_2015-6.pdf

[2] THM-7025 3-axis Hall effect teslameter (discontinued – replaced by THM-1176), MetroLab Technology SA, Geneva, Switzerland.

[3] F. Uhlig et al., "Performance Studies of Microchannel PMTs," Nucl. Instr. Meth. A 695 (2012) 68-70.

[4] U. Akgun et al., "Boron and thermal neutron interactions on borosilica window photomultiplier tubes," 2010 JINST 5 P08005.

[5] G. Dajko et al., "Results of gamma photon and neutron irradiations of Hamamatsu R5600-03/NG photomultiplier tubes," Conference Proceedings of the 6th Workshop on Electronics for LHC Experiments (Sept. 200) Cracow, Poland, p. 540-544.

[6] H. Grabas et al., "RF strip-line anodes for Psec large-area MCP-based photodetectors," Nucl. Instr. Meth. A711 (2013) 124–131.

[7] B.W. Adams et al., "An internal ALD-based high voltage divider and signal circuit for MCP-based photodetectors," Nucl. Instr. Meth. A780 (2015) 107–113.

[8] B.W. Adams et al., "Timing characteristics of Large Area Picosecond Photodetectors," Nucl. Instr. Meth. A795 (2015) 1–11.

[9] J. Wang et al., "Development and testing of cost-effective, 6 cm x 6 cm MCP-based photodetectors for fast timing applications," Nucl. Instr. Meth. A804 (2015) 84-93.

[10] V. Popov et al., "Performance studies of Hamamatsu R9800 photomultiplier tubes with a new active base designed for use in the Hall D Broadband Tagger Hodoscope," proceedings of the 2014 IEEE NSS/MIC Conference (Seattle, WA) November 2014.